

UNDERGROUND MEASUREMENTS AND SIMULATIONS ON THE MUON INTENSITY AND ^{12}C -INDUCED NUCLEAR REACTIONS AT LOW ENERGIES

Felix Ludwig

Wissenschaftlich-Technische Berichte
HZDR-116

Felix Ludwig

**UNDERGROUND MEASUREMENTS AND SIMULATIONS
ON THE MUON INTENSITY AND ^{12}C -INDUCED
NUCLEAR REACTIONS AT LOW ENERGIES**

Druckausgabe: ISSN 2191-8708

Elektronische Ausgabe: ISSN 2191-8716

Die elektronische Ausgabe erscheint unter Creative Commons License (CC BY 4.0):

<https://www.hzdr.de/publications/Publ-33273>

<urn:nbn:de:bsz:d120-qucosa2-763437>

Die vorliegende Arbeit wurde sowohl als Dissertation an der Fakultät Mathematik und Naturwissenschaften der Technischen Universität Dresden sowie als Wissenschaftlich-Technischer Bericht des Helmholtz-Zentrum Dresden – Rossendorf mit der Berichtsnummer **HZDR-116** veröffentlicht.

2021

Herausgegeben vom

Helmholtz-Zentrum Dresden - Rossendorf

Bautzner Landstraße 400

01328 Dresden

Germany



TECHNISCHE
UNIVERSITÄT
DRESDEN



HELMHOLTZ
ZENTRUM DRESDEN
ROSSENDORF

Underground measurements and simulations on the muon intensity and ^{12}C -induced nuclear reactions at low energies

Dissertation

zur Erlangung des akademischen Grades

Doctor rerum naturalium

(Dr. rer. nat.)

vorgelegt

der Fakultät Physik

der Technischen Universität Dresden

von

Felix Ludwig

geboren am 19.05.1993 in Plauen

Eingereicht am 25.02.2021

Diese Dissertation wurde von April 2017 bis Februar 2021 am Institut für Strahlenphysik
des Helmholtz-Zentrums Dresden-Rossendorf und am Institut für Kern- und
Teilchenphysik der Technischen Universität Dresden angefertigt.

1. Gutachter: Prof. Dr. Kai Zuber
2. Gutachter: PD Dr. Daniel Bemmerer
3. Gutachter: Prof. Dr. Alessandra Guglielmetti

Abstract

The reaction $^{12}\text{C}(\alpha,\gamma)^{16}\text{O}$ is of paramount importance for the nucleosynthesis of heavier elements in stars. It takes place during helium burning and determines the abundance of ^{12}C and ^{16}O at the end of this burning stage and therefore influences subsequent nuclear reactions. Currently the cross section at astrophysically relevant energies is not known with satisfactory precision.

Due to the low cross section of the reaction, low background, high beam intensities and target thicknesses are necessary for experiments. Therefore a new laboratory hosting a 5 MV ion accelerator, was built in the shallow-underground tunnels of Felsenkeller. The main background component in such laboratories was investigated with a muon telescope in this thesis. It was found, that the rock overburden of about 45 m vertical depth reduces the muons by a factor of about 40 compared to the surface. Furthermore the results of the measurements were compared to a simulation based on the geometry of the facility and showed good agreement. In the next step the accelerator was put into operation. Since the experiment on $^{12}\text{C}(\alpha,\gamma)^{16}\text{O}$ will be done in inverse kinematics, an intense carbon beam is necessary to reach sufficient statistics. For this, the creation and extraction of carbon ions in an external ion source was improved. The external source now provides steady currents of $^{12}\text{C}^-$ of above 100 μA .

In the following the transmission through the accelerator and the high-energy beamline was tested with a beam restricted in width. The pressure of the gas stripper in the centre of the accelerator and the parameters of different focusing elements after the accelerator were varied. It was found, that for a desired carbon beam energy of below 9 MeV, the 2+ charge state is suited best, where up to 35% of the inserted beam could be transmitted.

To ease the planning of future experiments and aid the analysis of the data, the target chamber and two different kinds of cluster detectors were modelled in GEANT4. The low-energy region was verified by comparing the simulations to measurements with radioactive calibration sources. Deviations for the detectors were below 10% without target chamber, and up to 30% for individual germanium crystals of the Cluster Detectors with the target chamber.

A first test measurement was undertaken to investigate the capabilities of the new laboratory. Solid tantalum targets implanted with ^4He were prepared. An ERDA analysis of the used solid targets showed contaminations with carbon and oxygen. These led to beam-induced background in the region of interest during the irradiation.

Then the targets were irradiated with a carbon beam at two different energies. While no clear signal of $^{12}\text{C}(\alpha,\gamma)^{16}\text{O}$ could be observed, the beam could be steered on the target for the whole duration of the beam time spanning five days. Problems during this test, like low beam current, were identified. These could be partly remedied in the scope of this thesis. Suggestions for improvements for a second test run were developed as well.

Parts of the present data in sec. 2.4 have already been published in a peer-reviewed journal:
F. Ludwig, L. Wagner, T. Al-Abdullah, G.G. Barnaföldi, D. Bemmerer, D. Degering, K. Schmidt, G. Surányi, T. Szücs, K. Zuber

The muon intensity in the Felsenkeller shallow underground laboratory

Astroparticle Physics 112 (2019) 24–34

This work was supported by the Helmholtz Association (NAVI VH-VI-417 and ERC-RA-0016), DFG (BE4100/4-1) and the COST Association (ChETEC CA16117).

Contents

1	Introduction	1
1.1	Evolution of stars	2
1.1.1	Helium burning	2
1.1.2	Subsequent burning stages	4
1.2	The $^{12}\text{C}(\alpha,\gamma)^{16}\text{O}$ reaction	4
1.2.1	Importance of the reaction	5
1.2.2	Review of prior measurements	6
1.3	Aim	11
1.4	Structure of the thesis	11
2	Muon background measurements in shallow-underground laboratories	13
2.1	The muon	13
2.1.1	Muon production in the atmosphere	13
2.1.2	Muons underground	14
2.2	The REGARD muon telescope	16
2.2.1	Experimental planning	17
2.2.2	Data analysis	17
2.3	Measurements on the surface	22
2.4	Measurements in Felsenkeller	23
2.4.1	Systematic uncertainties on the muon intensity	27
2.4.2	Matching the measurements	29
2.4.3	Temperature Correction	35
2.4.4	Other temporal effects on the muon intensity	36
2.5	Measurements in the IAEA Monaco	37
2.5.1	Calculation of the averaged threshold energy	39
3	Re-installing and testing the sputter ion source for the Felsenkeller accelerator	41
3.1	The ion source	41
3.2	Setup at HZDR	42
3.2.1	Results at HZDR	43
3.3	Setup at Felsenkeller	45

3.4	Improvements of the ion source for carbon beam	46
3.4.1	Influence of the cathode voltage	46
3.4.2	Influence of the caesium focus	48
3.4.3	Study of different sample holder material	48
3.5	Magnetic beam analysis	49
3.5.1	Hysteresis of the electromagnet	50
3.5.2	Conversion from the magnet current to the ion mass	50
3.5.3	Beam analysis	52
3.6	Realignment of the ion source	56
4	Commissioning of the accelerator	59
4.1	The accelerator	59
4.1.1	Accelerator conditioning	60
4.1.2	Terminal voltage stability	62
4.2	The high-energy beamline	64
4.2.1	Vertical beam alignment	66
4.2.2	Horizontal beam alignment	66
4.3	Stripper gas pressure	70
4.3.1	Fundamental interactions in the stripper	70
4.3.2	Stripper setup at Felsenkeller	72
4.3.3	Experimental method	73
4.3.4	Charge state distribution for different stripper pressures	74
4.3.5	Charge state distribution for different terminal voltages	76
4.3.6	Transmission	77
4.3.7	Lessons for experiments	79
5	Towards a measurement of the $^{12}\text{C}(\alpha,\gamma)^{16}\text{O}$ reaction at Felsenkeller	81
5.1	Monte Carlo simulations	81
5.1.1	Cluster detectors	82
5.1.2	The encapsulated HPGe Crystal	82
5.1.3	General approach for the verification of the simulation	84
5.1.4	The simulation of the Miniball	87
5.1.5	The simulation of the Euroball	87
5.1.6	Verification of the target chamber	89
5.1.7	Optimization of the setup	91
5.2	First test measurements at Felsenkeller	93
5.2.1	The experimental setup	94
5.2.2	Targets	94
5.2.3	The detectors	97

5.2.4	Data acquisition	98
5.2.5	Beam-induced background	99
5.2.6	Problems during the first test	100
5.2.7	Achievements of the first test	103
5.2.8	Runs on the E1 resonance	105
5.2.9	Runs on the E2 resonance	105
5.3	Preparations for a future irradiation	109
6	Summary and Outlook	111
A	Appendix	117
A.1	List of abbreviations	117
A.2	Stripper charge distribution	119
A.3	Simulation results	121
Anhang		115
Bibliography		125

List of Figures

1.2.1	Energy levels of ^{16}O	5
1.2.2	Total S-factor of $^{12}\text{C}(\alpha,\gamma)^{16}\text{O}$	9
1.2.3	E1 S-factor of $^{12}\text{C}(\alpha,\gamma)^{16}\text{O}$	10
1.2.4	E2 S-factor of $^{12}\text{C}(\alpha,\gamma)^{16}\text{O}$	10
2.1.1	Muon energy spectrum at earth's surface	15
2.1.2	Background components underground	15
2.2.1	Design close cathode chamber	16
2.2.2	Illustration of the telescope orientations	18
2.2.3	Comparison between three and seven measurements	18
2.2.4	Alignment histogram	20
2.2.5	Efficiency of the six chambers of the muon telescope	21
2.2.6	Consistency of measurements with different orientations	21
2.3.1	Muon intensities on the surface	22
2.4.1	Terrain of the Felsenkeller site	24
2.4.2	Map of the Felsenkeller tunnels	24
2.4.3	Muon intensities in Felsenkeller	26
2.4.4	Dependency of the muon intensity on the zenith angle	27
2.4.5	Dependency of the muon intensity on the depth	28
2.4.6	Event rate of the muon telescope	29
2.4.7	Comparison between measurement, analytic calculation and two simulations	32
2.4.8	Residuals of the calculation and two simulations	34
2.4.9	Energy spectra from the simulation of electrons	35
2.4.10	Effective temperature for Felsenkeller	37
2.5.1	Position of the muon telescope in CAVE, Monaco	38
2.5.2	Elevation map of Monaco	38
2.5.3	Muon intensity in CAVE, Monaco	39
3.1.1	Schematic of the ion source	42
3.2.1	Ion source test stand at HZDR	43
3.2.2	Ion source beam current over time at HZDR	44
3.2.3	Drawing of the sample holders	44

3.3.1	Ion source setup at Felsenkeller	45
3.4.1	Dependency of the caesium focus voltage on the ion beam current	49
3.5.1	Hysteresis of the electromagnet at the low-energy beamline	51
3.5.2	Conversion from magnet current to ion mass	51
3.5.3	Beam analysis for two different sample holders	53
3.6.1	Realignment of the ion source	56
3.6.2	Beam position before and after realignment	57
4.1.1	Schematics of a tandem Pelletron	61
4.1.2	Accelerator conditioning	61
4.1.3	Terminal stability	62
4.2.1	Schematics of the high-energy beamline	65
4.2.2	Vertical position of the beam on BPM 6 before adjusting the electromagnet	67
4.2.3	Vertical position of the beam in the HE beamline after adjusting the electromagnet	67
4.2.4	Horizontal beam alignment in the HE beamline	69
4.2.5	Horizontal beam alignment in the HE beamline after installing an x -steerer	69
4.3.1	Cross sections for electron exchanges	71
4.3.2	Stripper tube at Felsenkeller	72
4.3.3	Charge fractions for different stripper pressures at 1.1 MeV beam energy	75
4.3.4	Charge fractions for different beam energies at an areal gas density of $0.3 \mu\text{g}/\text{cm}^2$	75
4.3.5	Charge fractions for different beam energies at an areal gas density of $0.5 \mu\text{g}/\text{cm}^2$	77
4.3.6	Transmission from FC2 to FC4	78
4.3.7	Transmission through the accelerator and the HE beamline	80
5.1.1	Implementation of the detectors in the simulation	83
5.1.2	GEANT4 implementation of the encapsulated HPGe Crystal	83
5.1.3	Fitting procedure for efficiency calculation	86
5.1.4	Summing effects	86
5.1.5	Comparison between the efficiency of the Miniball without target chamber for experiment and simulation	88
5.1.6	Comparison between the efficiency of the Septuple Cluster for experiment and simulation	88
5.1.7	Setup of the simulation	90
5.1.8	Comparison between the efficiency of the Triple Cluster in the setup for the first test for experiment and simulation	90
5.1.9	Comparison between the efficiency of the Septuple Cluster in the setup for the first test for experiment and simulation	91
5.1.10	Angular distribution of $^{12}\text{C}(\alpha,\gamma)^{16}\text{O}$	92
5.1.11	Simulated spectrum for the E2 resonance	93

5.2.1	Schematic view of the target chamber for the first test measurement	95
5.2.2	Detector setup for the first test measurement	95
5.2.3	Target depth profile calculated with SRIM	96
5.2.4	Target depth profile by ERDA	98
5.2.5	Beam-induced background	101
5.2.6	Target FL5 after irradiation	102
5.2.7	Accelerator voltage and target current throughout the beam time	104
5.2.8	$^{12}\text{C}(p,\gamma)$ spectrum MB2	104
5.2.9	Spectrum of the runs on the E1 resonance	106
5.2.10	Spectrum of the runs on the E2 resonance	108
5.3.1	Permanent magnet position on target chamber	109
5.3.2	Terminal stability after recalibration	110
5.3.3	55° target chamber	110
A.2.1	Charge fractions for different stripper pressures at various beam energies	119
A.2.2	Charge fractions for different beam energies at various stripper areal densities .	120
A.3.1	Simulation results Triple Cluster without target chamber	121
A.3.2	Simulation results Triple Cluster with target chamber	122
A.3.3	Simulation results Septuple Cluster without target chamber	123
A.3.4	Simulation results Septuple Cluster with target chamber	124

List of Tables

2.4.1 Muon intensity results in Felsenkeller	25
3.4.1 Sputter yields by SRIM	47
3.4.2 Dependency of the cathode voltage on the ion beam current	47
3.5.1 Operating parameters for beam analysis	52
3.5.2 List of extracted ions	55
3.5.3 Intensity of polyatomic carbon peaks	55
3.5.4 Ratio of carbon peaks compared to the isotopic abundances	55
4.3.1 Comparison of particle current of different charge states for various beam energies	79
5.1.1 Gamma source activities	84
5.1.2 Dead layers of the crystals	89
5.2.1 ERDA analysis results for the targets	97
5.2.2 High voltages for the crystals	97
5.2.3 Trapezoid reconstruction parameters	99
5.2.4 Q values for possible background reactions	100
5.2.5 Overview of the beam time	103

1 Introduction

When we study the world around us, everything we see is made up of atoms. How these atoms were synthesized, is investigated in the field of nuclear astrophysics. Experimental data on the elemental abundances in the universe is gained from several sources: samples from the earth, the moon or meteorites, absorption spectra of the sun and other stars or the observation of gamma lines from radioactive decays, to name a few. These abundances are then compared to the results of nuclear reaction networks, which are based on data of the relevant nuclear reactions and their cross sections in the astrophysically interesting energy-range. More precise information about these reactions, which are determined i.e. in accelerator-based experiments, can then be used to improve our models in the case of discrepancies between prediction and observation [Ili08].

Today, we believe, that during the early stages of the universe only three elements could be created: hydrogen, helium and lithium. A majority of the elements heavier than these three is the product of nuclear reactions inside stars or during stellar explosions, while a few isotopes are the product of cosmic rays. Therefore stars not only provide the energy to make life, as we know it, possible, but also the very building blocks of organic matter: carbon and oxygen. An important reaction for the synthesis of these is the $^{12}\text{C}(\alpha,\gamma)^{16}\text{O}$ reaction. Today, the cross section of this reaction in the astrophysically relevant low-energy region of 300 keV for core helium burning is only inaccurately known. Since this area was not yet experimentally accessible, because of the low cross section ($\approx 10^{-17}$ b) [BB06], scientists extrapolated from data at higher energies. To this end, the strong energy dependence of the cross section is eliminated by introducing the astrophysical S-factor S :

$$\sigma(E) = \frac{1}{E} e^{-2\pi\eta} S(E), \tag{1.0.1}$$

with σ the cross section, E the energy and $2\pi\eta$ the Sommerfeld parameter.

The accelerator laboratory at Felsenkeller is in principle able to measure $^{12}\text{C}(\alpha,\gamma)^{16}\text{O}$ down to an energy of 0.6 MeV in the centre-of-mass system (CMS). To achieve successful measurements of reactions with these low cross sections, a low background, an intense ion beam and a high target density are necessary. The first two will be investigated in this thesis.

Photons emitted by the $^{12}\text{C}(\alpha,\gamma)^{16}\text{O}$ reaction are highly energetic with energies of above 8 MeV. The main source of background in this area in the shallow-underground laboratory

Felsenkeller are muons. With the low expected signal of the reaction, it is important to precisely understand this background component. Therefore the muon intensity in the Felsenkeller laboratory is investigated in detail in this thesis.

At Felsenkeller, experiments in inverse kinematics are planned, so carbon needs to be ionized, accelerated to energies of about 2 to 10 MeV and then directed onto a helium target. To achieve a high carbon beam current, which is of tremendous importance for an experiment at these low cross sections, every part of this process will be analysed and improved as part of this thesis.

1.1 Evolution of stars

The $^{12}\text{C}(\alpha,\gamma)^{16}\text{O}$ reaction is believed to take place during helium-burning in stars. To increase the understanding of this process and the astrophysical sites, in which it takes place, this section will recall the most important steps in the evolution of a star based on the textbooks by Rolfs and Claus [Rol+88] and Iliadis [Ili08].

Whether a star can enter helium burning depends on its mass and its initial composition of elements. Stars with initial masses below 0.4 solar masses will only be able to fuse hydrogen, while higher-mass stars can enter subsequent burning stages, because they can reach higher temperatures in their core.

1.1.1 Helium burning

After all the hydrogen was fused to helium during hydrogen burning, hydrogen burning continues in a shell around the core for stars with initial masses above 0.4 solar masses. The radiation pressure of the core can not balance the gravitational force any more. In the result the core contracts and heats up, in turn increasing the temperature in the hydrogen burning shell as well. This extra energy blows up the hydrogen envelope tremendously, the star becomes a red giant. The convective envelope increases in size and the products of hydrogen burning are transported into the shell in the so-called first dredge up.

For stars with initial masses below $2 M_{\odot}$, during contraction of the core, it becomes electron degenerate. This means, that the gravitational collapse is halted by the pressure caused by the Pauli exclusion principle, where no two fermions, in this case electrons, can occupy the same quantum state. Therefore, when a temperature of around 0.1 GK is reached, and helium burning starts, temperature increases, while the pressure remains constant. The nuclear reaction rates increase and more and more energy is released, leading to a thermonuclear runaway, that is called helium flash. With this, the increasing temperature lifts the electron degeneracy. After that, the core balances by increasing in size and stable helium burning follows.

During this phase two nuclear reactions are taking place, that now will be described in more detail: The triple α reaction, that forms ^{12}C and $^{12}\text{C}(\alpha,\gamma)^{16}\text{O}$. Further α capture to neon has a higher Coulomb barrier and is non-resonant in the important energy region. Therefore it plays only a minor role for most helium burning sites [Cos+10; Ili08].

The triple alpha process is spanning the gap caused by no stable isotopes with $A = 5$ and 8. This happens in a two step process. First two α particles form the unstable ^8Be in its ground state, which dissociates back into two ^4He nuclei with a half-life of $8.19 \cdot 10^{-17}\text{ s}$: $^4\text{He} + ^4\text{He} \leftrightarrow ^8\text{Be}$. A small concentration of ^8Be will build up in the equilibrium of production and decay. Then ^8Be can fuse with another α to ^{12}C : $^8\text{Be}(\alpha,\gamma)^{12}\text{C}$. Normally, this two-stage process would be quite improbable, if it were not for two resonances. In the first part, the ground state of ^8Be is close to the $\alpha + \alpha$ threshold. The second reaction proceeds via the Hoyle state in ^{12}C , a $J^\pi = 0^+$ excited state, that is energetically close to the $^8\text{Be} + \alpha$ threshold and greatly enhances the probability of the process [BB06].

Because the half-life of ^8Be is so short, the second part of the reaction could not be measured experimentally yet. Nonetheless the cross section only has an uncertainty of around 15% in the relevant energy region, which was determined by indirect studies of the resonances [Fyn+05; Kir+12].

$^{12}\text{C}(\alpha,\gamma)^{16}\text{O}$ has no resonances directly in the Gamow window and is therefore slower. However, the high-energy tails of two sub-threshold resonances and the low-energy tail of a resonance with higher energy enhance the S-factor. Unfortunately this is leading to interferences, increasing the difficulty to obtain the cross section by theoretical means. Experiments could not yet reach down to the low energies, at which helium burning takes place. To date, the total S-factor at 300 keV is determined by An *et al.* to be $(162.7 \pm 7.3)\text{ keVb}$ [An+15] and by deBoer to $(140 \pm 21)\text{ keVb}$ [deB+17]. The low relative uncertainty given by An *et al.* [An+15] is part of a controversy, because the calculation of it is not explained in detail [deB+17].

These two reactions compete until the helium is exhausted. The core now contains a ratio of carbon to oxygen dominantly determined by the rates of the triple alpha process and $^{12}\text{C}(\alpha,\gamma)^{16}\text{O}$. A lower reaction rate of the latter would lead to less oxygen production and vice versa. With no fuel to halt gravitational collapse, the core contracts again.

For stars with initial masses below 9 solar masses, helium burning continues in a shell surrounding the core. This is followed by a helium shell and a shell, where hydrogen burning still continues in the deepest part, further supplying helium to the lower shell. This increases temperature in the helium zone and leads to another thermonuclear runaway. The hydrogen shell gets pushed out and cools down, so that now helium burning is the main energy source of the star. Following this another contraction takes place and hydrogen burning starts again, taking over the majority of the energy production. The process repeats itself and is called thermal pulse. During these, more and more material is lost from the star by stellar winds until all of the hydrogen envelope is lost. Then, only a electron degenerate carbon-oxygen

white dwarf remains, that will slowly cool down.

Stars with higher masses will be able to enter subsequent burning stages in an onion-like shape.

1.1.2 Subsequent burning stages

For stars with initial masses above $9 M_{\odot}$ no thermal pulses will occur and instead the temperature in the core reaches high enough temperatures to ignite carbon burning, while helium burning continues in a shell around the core. When the carbon fuel is exhausted, the hydrogen burning will restart in the shell and a complicated interplay between the helium and hydrogen shell takes place, that leads to helium shell flashes.

More massive stars will enter the subsequent stages of neon, oxygen and silicon burning, where the star displays an onion-like shape, with silicon burning in the core, followed by burning shells of oxygen, neon, carbon, helium and hydrogen. At the end of these burning stages, the star will either end as an oxygen-neon white dwarf, if the initial mass was between 9 to $11 M_{\odot}$, or in a core collapse supernova, which will leave a neutron star or a black hole.

1.2 The $^{12}\text{C}(\alpha,\gamma)^{16}\text{O}$ reaction

$^{12}\text{C}(\alpha,\gamma)^{16}\text{O}$ has been topic of intense research for not only experimentalists but also theorists for over 60 years. Intensive work was put into direct measurements of the reaction, but indirect techniques and theoretical calculations were utilized as well, to further the understanding of this particular reaction.

Fig.1.2.1 displays the level diagram of ^{16}O . For the $^{12}\text{C}(\alpha,\gamma)^{16}\text{O}$ reaction with a Q value of 7162 keV, transitions to the ground state and to four bound excited states of ^{16}O are possible [BB06]. These then decay by γ emission to the ground state, apart from the 0^+ state at 6.05 MeV, which decays by e^+e^- transition, because γ decay from a 0^+ to a 0^+ state is strictly forbidden by the conservation of angular momentum. Today, it is thought, that transitions to the ground state dominate over those to excited levels in the low-energy region [BB06].

Since no low-energy data of the cross section is available for this reaction, scientists extrapolate to the energy region of interest by utilizing nuclear structure information. However, this is especially difficult for this reaction, because it is dominated by broad overlapping and interfering resonances and a non-resonant part of the reaction, all of which are hard to accurately determine on a theoretical basis [deB+17]. Hence, new measurements at lower energies are necessary to improve the uncertainties and shed light on the oxygen to carbon ratio after helium burning in stars, which influences further nucleosynthesis.

The two following subsections, that focus on the importance of $^{12}\text{C}(\alpha,\gamma)^{16}\text{O}$ and prior measurements on this reaction combine the most relevant information from [deB+17] with new developments and measurements in the field.

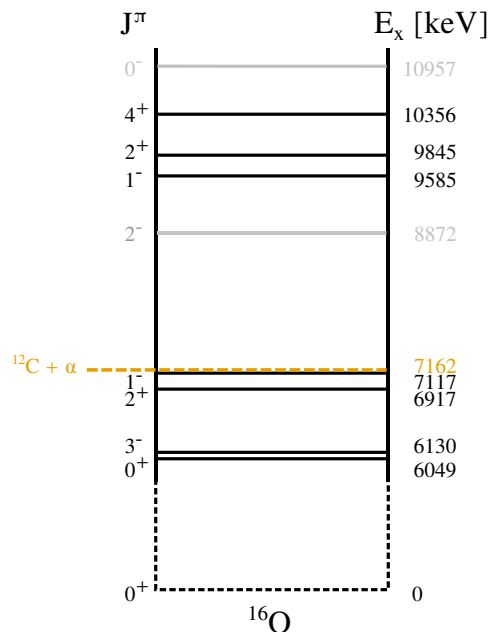


Figure 1.2.1: Energy levels of the compound nucleus ^{16}O . Levels, that are not important for $^{12}\text{C}(\alpha, \gamma)^{16}\text{O}$ because of their unnatural parity state, are marked in grey. The Q value of the reaction is given in orange.

1.2.1 Importance of the reaction

As mentioned before, the $^{12}\text{C}(\alpha, \gamma)^{16}\text{O}$ reaction has a huge impact on nucleosynthesis in stars, which was already noted by Fowler in his Nobel laureate lecture in 1983 [Fow84].

The carbon to oxygen ratio has a huge impact on subsequent burning stages. A variation in the $^{12}\text{C}(\alpha, \gamma)^{16}\text{O}$ rate affects the duration of helium-burning and the composition of the carbon-oxygen core [deB+17]. Stars with masses below $8 M_\odot$ will evolve to asymptotic giant branch stars, where further nucleosynthesis takes place. Exact modelling of this is challenging because of several sources of uncertainties, like the mixing of material, but it is clear, that $^{12}\text{C}(\alpha, \gamma)^{16}\text{O}$ has a large impact on the nucleosynthesis of elements heavier than ^{16}O [deB+17]. Helium burning continues in the helium shell, sometimes via helium flashes. In these, carbon and oxygen are synthesized, as well, and then mixed by convection in the envelope, where some of it is ejected as stellar winds. The composition of these is mainly determined by $^{12}\text{C}(\alpha, \gamma)^{16}\text{O}$ [deB+17; WH06].

If the star can not enter the subsequent burning stages, a white dwarf remains, which, in a binary system, might explode as a supernova of type Ia, where heavier elements are synthesized. The explosion process is heavily reliant on the initial composition of the white dwarf, which is determined by $^{12}\text{C}(\alpha, \gamma)^{16}\text{O}$ [deB+17] and the amount of ^{22}Ne [Mil+16].

The carbon to oxygen ratio is important for subsequent burning phases as well, since it determines, if and where in the core carbon ignition will take place. Therefore this reaction also has an impact on all isotopes, which are produced in the later burning stages, for example the radionuclides ^{26}Al , ^{44}Ti and ^{60}Fe [deB+17], which play an important role in the observation

of supernovae.

Additionally the ratio affects supernovae as well: in a paper by Sukhbold *et al.* [SW14] supernovae were simulated with the neutrino-transport model. Here, the energy from gravitational collapse is radiated from the star in the form of neutrinos, that then drive the supernova explosion. Sukhbold derived, that a combined uncertainty of the 3α process and $^{12}\text{C}(\alpha,\gamma)^{16}\text{O}$ of only 10% impacts, whether a massive star with mass of 19 to $25 M_{\odot}$ explodes in a supernova in the simulation by over $2 M_{\odot}$.

In massive stars most of the ^{14}N of the CNO-cycle will be converted to ^{22}Ne during helium burning, which is a neutron producer for the s-process by the reaction $^{22}\text{Ne}(\alpha,n)^{25}\text{Mg}$ [Rol+88]. In the late stages of helium burning $^{12}\text{C}(\alpha,\gamma)^{16}\text{O}$ limits the available ^4He nuclei for this reaction, which has an impact on the number of produced neutrons and therefore on the s-process, that synthesises many nuclides up to ^{209}Bi [Ili08].

The reaction has an impact on hydrogen burning via the CNO cycle as well. This cycle is the main energy source during hydrogen burning in stars with masses above $1.5 M_{\odot}$. The first generation of stars could at first not utilize this cycle, because they lacked the necessary carbon, oxygen and nitrogen, which were not produced during the Big Bang. Only after these elements were synthesized in the first star generations by the triple alpha process and $^{12}\text{C}(\alpha,\gamma)^{16}\text{O}$, hydrogen burning could proceed via the CNO cycle in new star generations, formed from their dust [Ili08].

1.2.2 Review of prior measurements

Starting in 1955 first efforts were undertaken to measure the $^{12}\text{C}(\alpha,\gamma)^{16}\text{O}$ reaction in the laboratory. Allan and Sarma [AS55] irradiated a carbon target with natural isotopic abundances with helium. The parasitic $^{13}\text{C}(\alpha,n)^{16}\text{O}$ reaction, that has a several orders of magnitude higher cross section, hindered their efforts by creating a huge background in their detectors. Therefore they could only deduce an upper limit for the reaction.

The first signal of the $^{12}\text{C}(\alpha,\gamma)^{16}\text{O}$ reaction was measured by Bloom *et al.* [BTW57] by subtracting the $^{13}\text{C}(\alpha,n)^{16}\text{O}$ background at α energies of around 3 MeV, where they investigated the 9.59 MeV state. Later on targets depleted in ^{13}C were used to measure a wider energy range and carbon build-up on the target was minimized. Larson and Spear [LS64] succeeded in covering a helium beam energy from 2.8 to 8.3 MeV, giving angular distributions of the reaction at higher energies.

The 1^- resonance at 9.59 MeV was first successfully investigated by Jaszczak *et al.* [JGM70]. They used highly ^{13}C -depleted ^{12}C targets and a bunched helium beam to separate the neutron events by the time-of-flight method. This resulted in the first excitation curve for the low-energy 1^- resonance. Alpha energies of 1.86 to 3.20 MeV were used and extended to 4.2 MeV in a later work [JM70].

Dyer and Barnes [DB74] then presented first accurate cross sections of the ground state tran-

sition. Since only E1 and E2 multipolarities are allowed for the decay of the 1^- and 2^+ state, they mostly positioned their detector at 90° , to single out the E1 contribution. This measurement was the first to investigate angular distributions of the reaction at low energies as well. They assumed, that the small E2 part, they could observe, was due to the direct capture mechanism, however, it was later found, that this stems from the 2^+ subthreshold state at $E_x = 6.92$ MeV [Ket+82].

This was followed by new data on the high-energy range of the reaction, namely above the proton separation energy of 12.13 MeV [MO64; KMV71; Bro+73; MO65; MKO68]. Two broad 1^- resonances at 12.45 and 13.09 MeV dominate this energy region and could influence astrophysical cross sections by interference effects.

After a gap of nearly a decade, first measurements in inverse kinematics on helium gas targets were performed. Kettner *et al.* [Ket+82] used a high-intensity carbon beam of 50 μ A with a windowless extended gas target. With this, they could reach down to a centre-of-mass energy of 1.34 MeV and conclude, that the E2 transition might influence the cross section as much as the E1 for low energies. Furthermore an excitation curve of the capture to the 6.92 MeV state was presented, but, since with NaI detectors the energy resolution was not sufficient, they could not distinguish the photons of this state from those of the 7.12 MeV state.

First experiments with lithium-doped germanium detectors were undertaken by Redder *et al.* [Red+87] in forward kinematics. ^{13}C in the targets was avoided by implanting ^{12}C into a gold plate. This achieved an estimated ^{13}C depletion of two orders of magnitude. Now the individual γ lines could be clearly distinguished and the angular distribution in the centre-of-mass energy range from $E_{\text{CMS}} = 1.7 - 2.84$ MeV was measured. Additionally the lowest measured energy could be pushed to $E_{\text{CMS}} = 0.94$ MeV. However, the reported cross section values at these low energies were higher than those by Dyer and Barnes [DB74].

Another experiment by Kremer *et al.* [Kre+88] with a recoil separator at CalTech was in agreement with the Dyer and Barnes data. They used theory input to determine the E1 to E2 ratio in the cross section.

An experiment by Ouellet *et al.* [Oue+92; Oue+96] was undertaken to rule out the discrepancy at low energy with a similar setup to the one by Redder *et al.* [Red+87]. The resulting cross section was, however, right between the two prior measurements, not resolving the discrepancy. Roters *et al.* [Rot+99] conducted another experiment in inverse kinematics on a gas target. They used Bismuth germanium oxide (BGO) detectors and could investigate angle-integrated cross sections and the E1 component at 90° . Gialanella *et al.* [Gia+01] followed this up with a similar experiment.

A detailed measurement of the angular distribution of the reaction at up to nine angles with HPGe detectors was done by Kunz *et al.* [Kun+01; Kun02]. This was followed up by experiments with the EURO GAM and GANDI arrays [Fey04; Ham+05a; Ham+05b; Ass+06]. These data were only partly peer-reviewed and the systematic uncertainties may have been

underestimated [BS13].

Another experiment with a gas target in a recoil separator was performed by Matei *et al.* at Tri University Meson Facility (TRIUMF) [Mat+06]. They investigated the energy range from $E_{\text{CMS}} = 2.22$ to 5.42 MeV with a focus on the transition involving the 6.05 MeV state.

Two alpha energies of 2 and 2.27 MeV were studied in detail by Makii *et al.* [Mak+09] by measuring in normal kinematics with Compton-suppressed NaI detectors at three angles and the time-of-flight method. The targets were produced by cracking ^{13}C depleted methane gas. The resulting cross sections were somewhat lower than prior data, but more precise and aligned well with previous R-matrix fits.

In 2012 Plag *et al.* [Pla+12] investigated the reaction with a solid target covered by a 4π BaF₂ detector array, which is segmented in a way, that data of twelve angles can be obtained, which were used to determine the E1 and E2 components.

An experiment at Kyushu University tandem laboratory by Ikeda *et al.* [Ike+03] is aiming for a centre-of-mass energy of 0.7 MeV and is still on-going. They use a gas target in inverse kinematics with time of flight and a recoil separator. First data at 2.4 MeV, 1.5 MeV and 1.2 MeV [Sag+17] were reported, while measurements for lower energies are currently taken.

A compilation of all existing measurements in the low-energy region can be found in fig. 1.2.2 for the total S-factor and in fig. 1.2.3 and fig. 1.2.4 for the E1 and E2 component, respectively. In all cases, the respective R-matrix fit by deBoer *et al.* [deB+17] is plotted as well.

In the future, several experiments at the recoil separators of TRIUMF, the Centre for Isotopic Research on Cultural and Environmental Heritage (CIRCE), and at St. George at Notre Dame University are planned. Furthermore, several experiments underground are in the planning stage at the Laboratory for Underground Nuclear Astrophysics (LUNA) [Pra20] and the Jinping Underground laboratory for Nuclear Astrophysics (JUNA) [Liu16] and are expected to deliver more data near the astrophysically relevant energies. Another accelerator underground at the Sanford Underground Research Facility (SURF) wants to focus on (α, n) reactions [Rob+16], but might put this reaction on their schedule in the future.

As can be seen, the focus of prior experiments laid on the E1 and E2 ground state transitions. This data could be supplemented by measurements of cascade transitions in a wide energy range to gain the total cross section of the reaction and would add to the measurements by [Ket+82; Red+87; Mat+06; Sch+11]. Additionally, experiments reporting differential cross sections would be important to further the understanding of the reaction. Until today this was only done by [DB74; Red+87; Fey04; Ass+06; Pla+12], where especially the data of Fey deviates.

Measurements at energies below 1.5 MeV are of special importance. Here some of the data points deviate from the fit and only few data points with large uncertainties down to 0.9 MeV are available to date. Therefore new data in this region and at even lower energies are necessary to improve the extrapolation to the astrophysical energy range for this reaction.

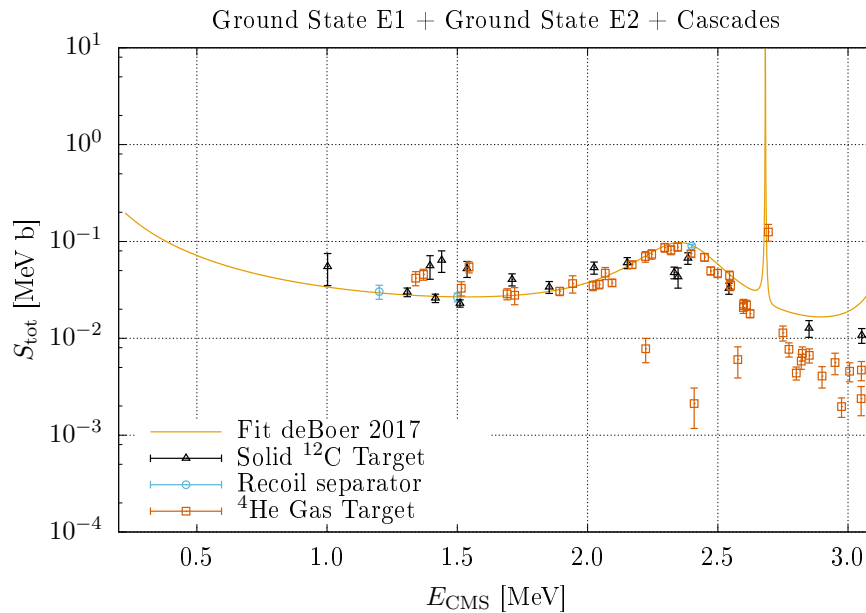


Figure 1.2.2: Compilation of total S-factor data of prior measurements on the $^{12}\text{C}(\alpha,\gamma)^{16}\text{O}$ reaction and an R-matrix fit (orange) by deBoer *et al.* [deB+17]. For core helium burning the relevant energy range is at 0.3 MeV. Black data points denote experiments in normal kinematics with solid ^{12}C targets [JGM70; JM70; Pla+12]. Skyblue data points are experiments with ^4He gas targets followed by a recoil separator [Sag+17], while vermilion data points were measured with ^4He gas targets [Ket+82; Mat+06].

With the groundwork laid down in this thesis, the Felsenkeller laboratory might be able to address all these areas, where there is a lack of data, in the future. With the planned extended gas target, experiments focusing on the total cross section of the reaction down to 0.6 MeV are in principle possible. The planned gas-jet target might be able to provide differential cross sections and the E1 and E2 components at 1 MeV and above. To cover a large solid angle for this endeavour, several HPGe detectors with good energy resolution are available at the Felsenkeller laboratory. So a significant contribution to the efforts on the measurements of $^{12}\text{C}(\alpha,\gamma)^{16}\text{O}$ by the Felsenkeller laboratory is in principle possible.

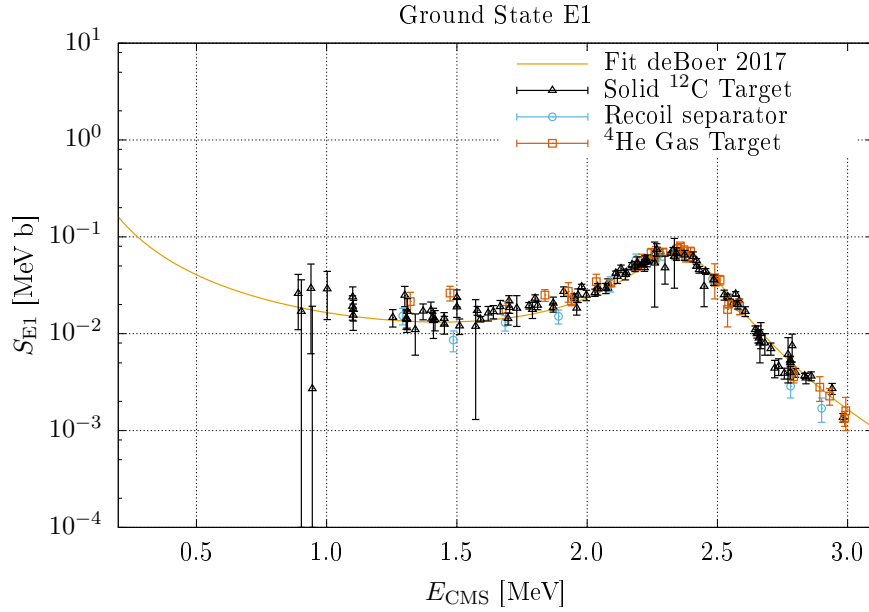


Figure 1.2.3: Compilation of S-factor data on the E1 to ground state transition of prior measurements on the $^{12}\text{C}(\alpha,\gamma)^{16}\text{O}$ reaction and an R-matrix fit (orange) by deBoer *et al.* [deB+17]. Black data points denote experiments in normal kinematics with solid ^{12}C targets [DB74; Red+87; Oue+96; Kun+01; Fey04; Ass+06; Mak+09; Pla+12]. Skyblue data points are experiments with ^4He gas targets followed by a recoil separator [Kre+88], while the vermillion data points were measured with ^4He gas targets [Rot+99; Gia+01].

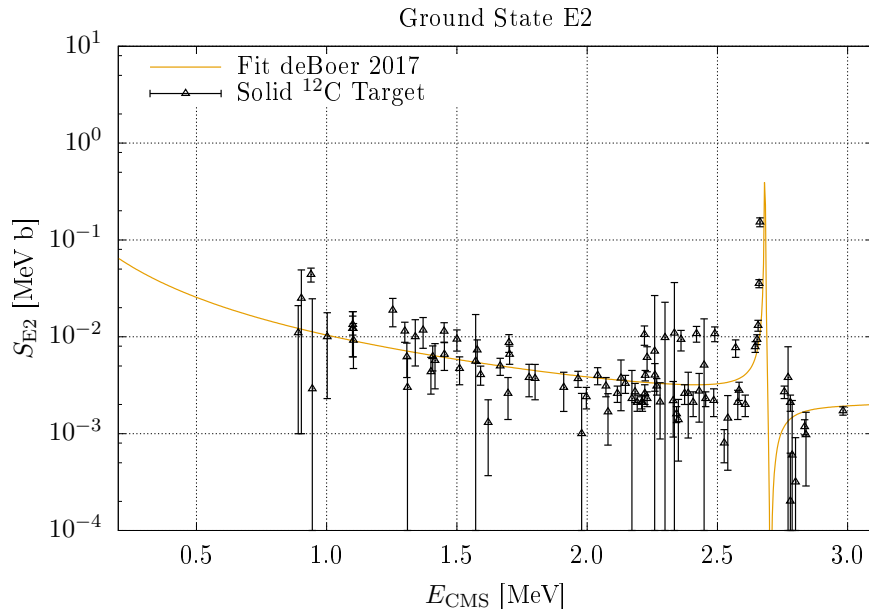


Figure 1.2.4: Compilation of S-factor data on the E2 to ground state transition of prior measurements on the $^{12}\text{C}(\alpha,\gamma)^{16}\text{O}$ reaction and an R-matrix fit (orange) by deBoer *et al.* [deB+17]. Black data points denote experiments in normal kinematics with solid ^{12}C targets [Red+87; Oue+96; Kun+01; Fey04; Ass+06; Mak+09; Pla+12].

1.3 Aim

The aim of this PhD thesis is a better understanding of the $^{12}\text{C}(\alpha,\gamma)^{16}\text{O}$ reaction. To accomplish this, the background in the Felsenkeller accelerator facility needs to be well understood. Since it mostly consists of muons, the muon intensity needs to be measured and analysed.

Further an intense ion beam will yield high statistics. To achieve this, the Felsenkeller accelerator needs to be put into operation and the ion beam current improved at each step of the creation and acceleration process: in the ion source, through the accelerator and the beamline to the target.

In order to test the capabilities of the new laboratory a first test measurement of the $^{12}\text{C}(\alpha,\gamma)^{16}\text{O}$ reaction with a solid ^4He target will be conducted at higher energies and analysed. This will pave the way for future experiments with a gas target at lower energies, where a higher target density will increase the statistics of experiments and reduce beam-induced background as well.

1.4 Structure of the thesis

Chapter 2 reports on the muon intensity in three tunnels of Felsenkeller, that was published in [Lud+19]. To understand the main background component in shallow-underground laboratories, the angle-resolved muon intensity is measured with high statistics. Furthermore a Monte Carlo description, based on precise geometry data of the tunnel and the overburden, is developed. The muon intensity in the shallow-underground laboratory CAVE in Monaco is examined as well.

This is followed by chapter 3 on the external ion source of the Felsenkeller accelerator. This ion source is put into operation and tested extensively, both on the surface and underground, to gain an intense, stable $^{12}\text{C}^-$ ion beam. Optimal operation parameters are extracted and new sputter targets for improved carbon current prepared. Parasitic beam components are analysed by a magnetic beam analysis.

After that the accelerator, the main component of the facility, is the focus of chapter 4. With a new LabVIEW based system, that yields complete control of each individual part of the facility, first experience is gathered. With focus on beam stability and intensity, every part of the system is tested and improved, namely the terminal potential stabiliser, the stripper pressure and the equipment for steering and focusing the ion beam.

A first test experiment with a helium-implanted target is conducted in chapter 5 to test the progress of the accelerator facility. Furthermore Monte Carlo simulations of the detectors and the experimental setups are undertaken to aid the analysis and the planning of future experiments. Both, the first test measurement and the simulations, lay the foundation for future experiments with a gas target and more detectors.

The thesis is concluded by a summary and an outlook in chapter 6.

2 Muon background measurements in shallow-underground laboratories

The following chapter is focused on the determination of the most problematic background component in shallow-underground laboratories: the muons. In the present work the muon telescope by the REGARD group [Olá+16] was used to measure the muon intensity at eight positions throughout the tunnel system of Felsenkeller.

First, section 2.1 will give a short overview on muons, their production in the atmosphere and muons underground. Then, section 2.2 will focus on the muon telescope itself. This will be followed by measurements on the surface in sec. 2.3 and underground in Felsenkeller in sec. 2.4. For the latter, the results on the muon intensity will be matched with a calculation and simulations. Section 2.5 will report on measurements in the shallow-underground laboratory of the International Atomic Energy Agency (IAEA) in Monaco.

2.1 The muon

The muon is a lepton with spin $\frac{1}{2}$ and a mass of 105.66 MeV. It has a mean lifetime of 2.2 μs , after which it decays into an electron, an anti-electron neutrino and a muon neutrino according to the standard model [Tan+18].

2.1.1 Muon production in the atmosphere

Muons, that are detected on the surface or underground, are produced by the collision of cosmic protons with nuclei of earth's atmosphere. This happens in the stratosphere and produces a myriad of particles, for example mesons, which can then decay into muons. The main contribution to the muon intensity on the surface of the earth stems from the decay of pions, while a smaller part is contributed by kaons. Since the mesons need to decay to produce a muon, there is a possibility, that they participate in another collision before decaying. They might be destroyed in these events, effectively decreasing the number of produced muons. This is especially important for pions as the lifetime of kaons is very short and an interaction before the decay is unlikely [Tan+18].

After production the muons have to pass through the atmosphere, where they lose energy through different processes: inelastic scattering, ionization and pair production. Which process

dominates, is determined by the energy of the muon. For the passage through the atmosphere, where muons lose around 2 GeV of energy on average, ionization is the most important process, which reduces the decay length from 15 km to 8.7 km for a 2.4 GeV muon [Tan+18].

Fig. 2.1.1 shows the energy distribution of muons for two different zenith angles at the surface of the earth. To explain this spectrum, all of the above described processes have to be taken into account. At $\theta = 0^\circ$ the muon spectrum is shifted to lower energies, because pions with higher energy reach deeper into denser layers of the atmosphere, where they have a higher chance of interacting with other particles instead of decaying into a muon. Furthermore the path through the atmosphere is the shortest, resulting in a low probability of the muon decaying, before reaching the surface. For 45° the spectrum is shifted to higher energies. Now it is more likely, that high-energy pions decay before they interact and for muons to decay before they reach the surface, both effects resulting in muons with higher energy. [Tan+18]

Due to this, seasonal effects can be observed. The density of the atmosphere is a major factor for the production of muons and their energy spectrum. Especially important is the temperature and the pressure of the layer of the atmosphere, where most muons are created. The effect of the temperature is indirect proportional: higher temperatures and lower pressures lead to lower densities, higher muon energies and therefore more muons being able to penetrate the stone and reach underground laboratories. The temperature has a bigger effect than the pressure [Sag86].

Another effect with a time dependency is the solar activity. Long-time measurements of the muon intensity exhibit an anti-correlation to the 11 and 22 year periodic solar cycles [Men+16]. This is thought to be caused by the varying magnetic field of the sun during the cycle [RC19].

2.1.2 Muons underground

When muons pass through matter, they continuously lose energy by ionization and three radiative processes: bremsstrahlung, pair production and photonuclear interactions. For low energy muons, ionization is the main source of energy loss, while for high energy the radiative processes dominate. This leads to a lower number of muons in underground settings due to absorption and a shift to lower energies in the muon spectrum.

A plot of the vertical intensity for various background sources as a function of depth is shown in fig. 2.1.2. In Felsenkeller, the muons are mitigated by a factor of around 40, but are still the main component of the background, while the nucleonic part of cosmic rays is completely absorbed. For laboratories deeper underground neutrons from (α, n) reactions and fission get increasingly important.

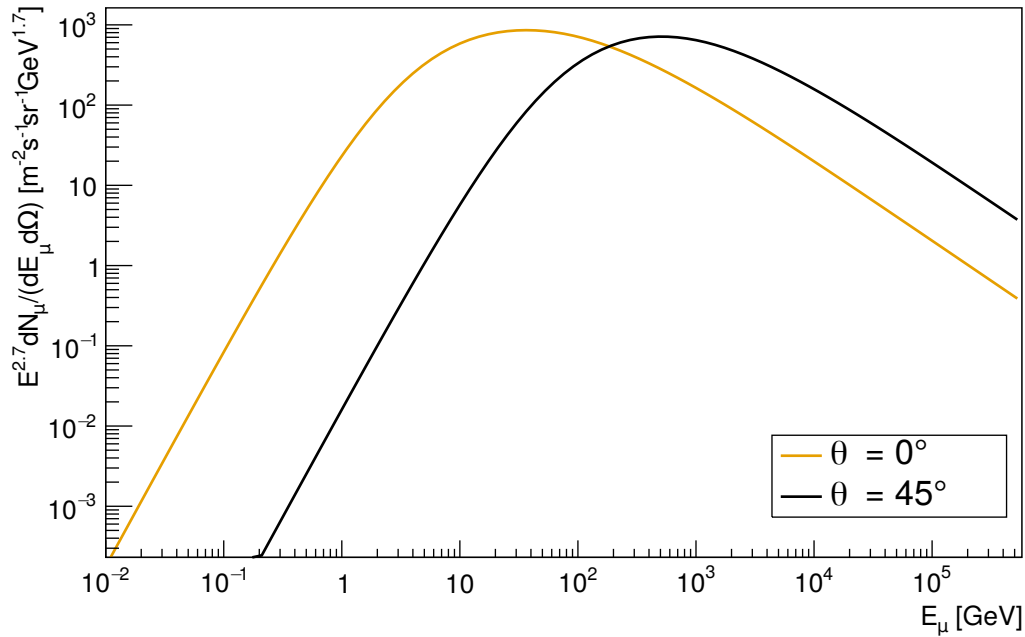


Figure 2.1.1: Energy spectrum of muons for the two different zenith angles $\theta = 45^{\circ}$ (orange) and $\theta = 0^{\circ}$ (black) as given by the parametrization by Tang *et al.* [Tan+06].

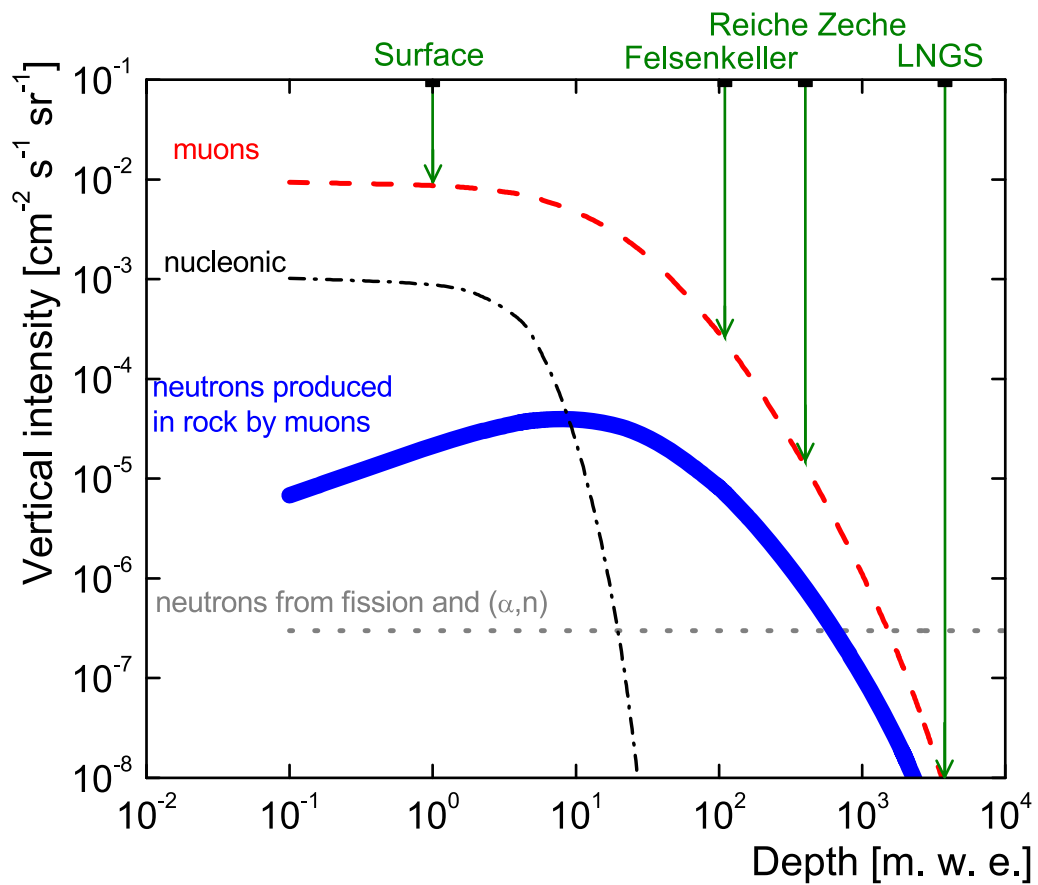


Figure 2.1.2: Vertical intensity of various background components as a function of depth. Two shallow-underground sites with Felsenkeller and Reiche Zeche and the deep-underground laboratory LNGS are marked.

2.2 The REGARD muon telescope

The REGARD muon telescope was especially designed for the usage in caves and therefore provides high robustness, a good angular resolution and a large effective area with transportability and low power-consumption [VHK11; Bar+12; Var+13].

Six close cathode chambers, which are vertically spaced by 3.5 cm and have an active area of $25.6 \times 25.6 \text{ cm}^2$, are placed in a plexiglass box, which is continuously flushed by ATAL (82% argon and 18% carbon dioxide) with a flow rate of 0.5 l/h.

Each chamber (see fig. 2.2.1) consists of a printed circuit board divided into 64 pads with 4 mm width on ground potential. Above this baseplate 64 field wires are tightened perpendicular to the pads in a distance of 1.5 mm, spaced by 4 mm on a potential of -600 V. In the centre of two field wires are sense wires on a potential of 1060 V resulting in an electrical field of 8.3 kV/cm. A cathode on -600 V and positioned 10 mm above the baseplate completes the chamber design. The mechanical robustness is ensured by several support pillars in-between the cathode and the baseplate. Due to the lower distance of the field wires to the baseplate, they can be fixated at it, resulting in less heavy support structures. Furthermore the yield gets nearly independent of the distance in this setup, which relaxes restrictions on mechanical deviations, for example caused by overpressure of the flushing gas [VHK11].

The electronics, powered by a 12 V battery or via plug, are mounted on a printed circuit board above the chambers and are separated into three parts: a mainboard for the data acquisition and the low voltage part, a high voltage module for the chambers and a raspberry pi for data saving and maintenance. Raw data can then be copied via Wi-Fi to a laptop for further analysis. The high voltage on the field wires can be set from the outside and checked by two monitors, which display the voltage and the current on the sense wires.

If an ionizing particle passes through the detector it ionizes the detector gas. Due to the high voltages the resulting electrons get accelerated and ionize more gas atoms, creating an avalanche, that is detected by the sense wires. This then induces current in the neighbouring field wires and the cathode strips underneath. If two of the chambers detect a signal above a threshold of 400 mV in coincidence, an event is saved containing the fired field wires, pads and

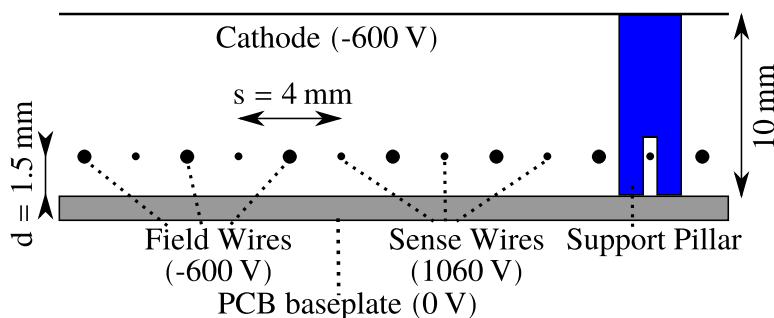


Figure 2.2.1: Horizontal cut of one close cathode chamber

a timestamp. After a dead time of 100 μs the device is ready for another hit.

All six chambers and the plexiglas wall correspond to an areal density of 2.63 g/cm². Therefore electrons with a energy of at least 8 MeV [Ber+05] and muons with 30 MeV [GMS01] will be able to pass these in the continuously slowing down approximation. However, since the electron is far lighter, it is more probable to be scattered multiple times and will most likely not pass through the detector in a straight line, which is a requirement to get counted as a muon. Photons from natural radioactivity have energies below 2.615 MeV and are not able to hit all chambers in coincidence. Background in the detector by other particles than muons will be discussed in the next subsection and in subsection 2.4.2.

2.2.1 Experimental planning

Due to the limited size of the detector it is not possible to measure the whole upper hemisphere in one measurement. With an opening angle of $\pm 56^\circ$ three measurements, one in vertical and two in horizontal orientation, would be necessary to cover every direction. However for larger angles the detection area gets smaller, e.g. one third at 40° , and statistics deteriorate. Therefore it is more suitable to add four measurements in a diagonal orientation to a total of seven measurements (see figure 2.2.2). A comparison of the statistical uncertainties for three and seven measurements with the same total measurement time is presented in fig. 2.2.3. The improvement in the area of $\theta = 45^\circ$ is apparent, while for high θ , where the muon intensity is low, the three measurements are better. Since these directions are not important for the purpose of the studies conducted here, seven measurements were performed at each location in the underground laboratories. The different measurements are then combined during offline analysis (see next subsection).

2.2.2 Data analysis

As mentioned previously, data is recorded by the telescope in the form of hit channels in the x and y direction per chamber and timestamps. To calculate the muon intensity one has to identify muon tracks in the data.

After reading in the raw data, the two spatial directions characterized by the pads and the field-wires are scanned for muon tracks independently. This is done by looking for clusters in the hit channels, that are qualified by one to six hit channels next to each other. If there are clusters in at least five of the six chambers, a linear fit is performed. The track with the best χ^2/dof below 2 is selected, yielding the slope of the track in the coordinate system of the telescope. Should there be more than one track per event, only the one with lower χ^2/dof will be accepted, however for underground measurements the rate of muon events with two muons in a temporal coincidence of 200 μs is rare and happened in below 0.01% of the muon events in all underground runs.

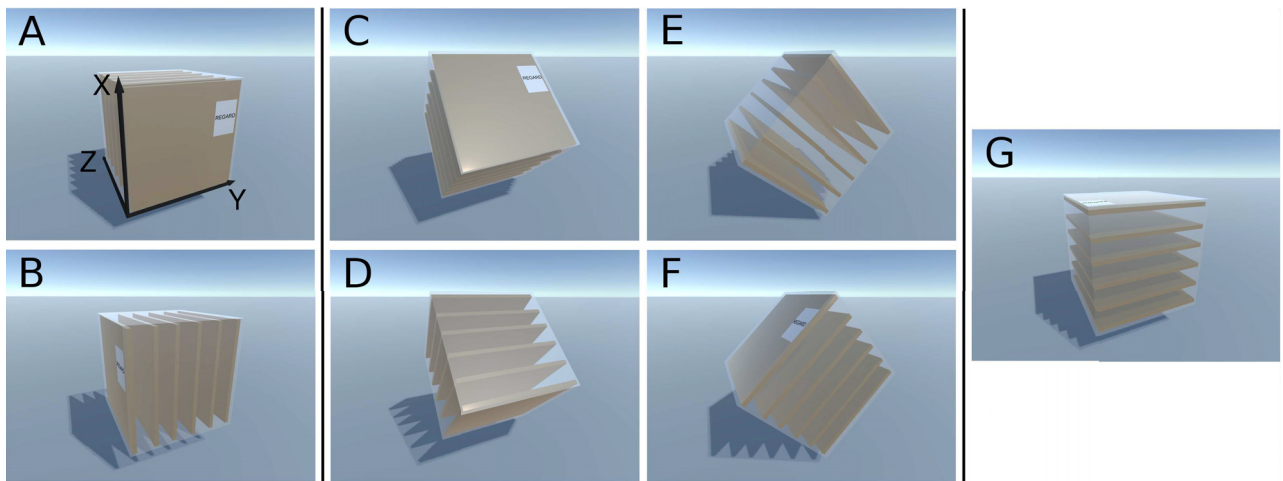


Figure 2.2.2: Illustration of the seven orientations of the muon telescope, which were used at each measurement position. A shows the coordinate system of the telescope as well.

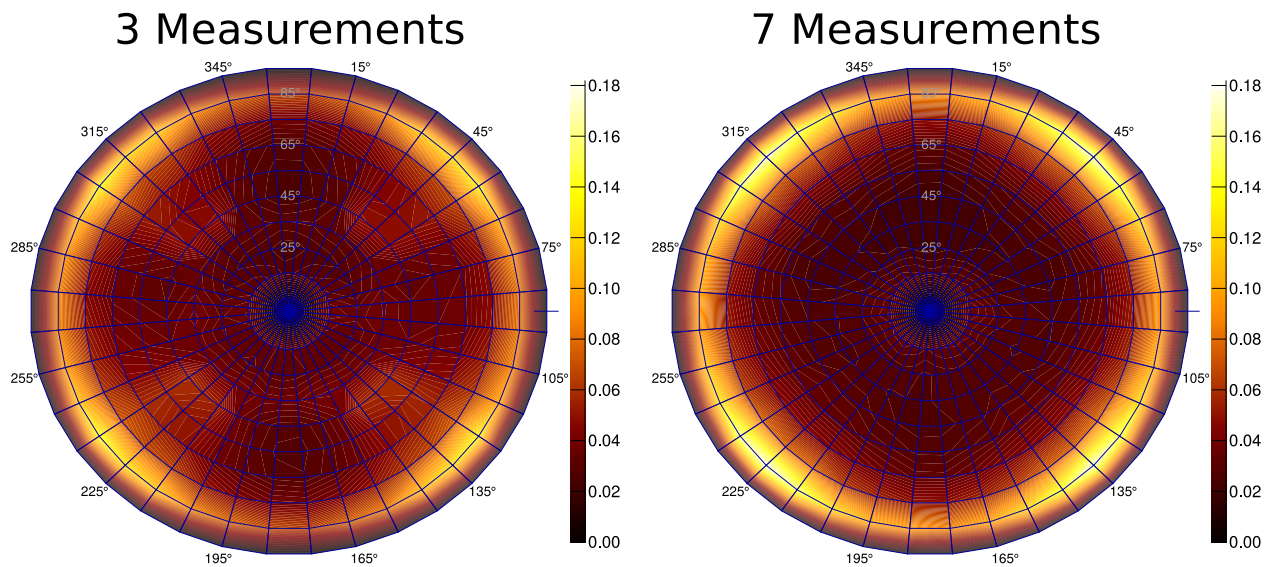


Figure 2.2.3: Comparison of the relative statistical uncertainties between three (orientations A, B and G in fig. 2.2.2) and seven measurements (orientations A to G) on the surface with the same total time. For three measurements the uncertainties are higher for zenith angles around 45° , while the seven measurements perform worse for high zenith angles.

This fitting procedure is first done for 2000 tracks to determine the parameters of the correction for the alignment of the chambers. Due to mechanical imperfections they can be slightly misaligned and/or tilted. To correct for this the difference between the coordinate of the cluster and the calculated coordinate of the linear fit is filled into a histogram (see figure 2.2.4). Later track coordinates are then shifted by the mean of this histogram. In addition to this correction, the histogram yields a measure for the spatial resolution of the telescope by the standard deviation $\sigma_{x,y}$. During the measurements these varied between $\sigma_x = 1.08 - 1.29$ mm and $\sigma_y = 0.97 - 1.23$ mm resulting with the height of the telescope of 17.5 cm in an upper limit for the resolution of ≤ 7.4 mrad or $\leq 0.85^\circ$, which is far smaller than the later used bin size. Following this pre-analysis the above described method is applied again, with the difference, that now the track coordinates are corrected by the alignment. Now also tracks with five triggered chambers are accepted, if the sixth point of the track would be inside the detector volume.

After that, the efficiency ε_i of the single chambers is calculated. The examined chamber is excluded and the other chambers are searched for tracks. ε_i then is the number of tracks, where there is a hit in or near the channel calculated by the fit in chamber i divided by the total number of tracks. This yields efficiencies for the chambers above 94% as can be seen in fig. 2.2.5. The total efficiency of the telescope is then calculated as follows:

$$\varepsilon = \prod_{i=1}^6 \varepsilon_i + \sum_{i=1}^6 \prod_{j=1}^6 [(1 - \delta_{ij})\varepsilon_i + \delta_{ij}(1 - \varepsilon_i)], \quad (2.2.1)$$

where $\delta_{ij} = 1$ for $i = j$ and 0 otherwise.

Now the slope of the tracks has to be converted from the telescope coordinates to the azimuthal angle φ and the zenith angle θ , taking into account the orientation of the telescope during the run (see fig. 2.2.2). For this, the slope coordinates are rotated to the reference position and then passed into the following equations, with the assumption, that all muons come from the upper hemisphere:

$$\theta = \arctan \left(\sqrt{m_{\text{Pad}}^2 + m_{\text{Fw}}^2} \right), \quad (2.2.2)$$

$$\varphi = \arccos \left(\frac{m_{\text{Pad}}}{\tan \theta} \right) = \arccos \left(\frac{m_{\text{Pad}}}{\sqrt{m_{\text{Pad}}^2 + m_{\text{Fw}}^2}} \right). \quad (2.2.3)$$

These angles are now filled into a histogram, with a correction factor for the effective detection area of this track, ranging from 1 for muons perpendicular to the muon telescope to 17000 for muons, which pass on a diagonal through the detector. When all events are analysed the

muon intensity I is calculated from this histogram, as follows:

$$I(\varphi, \theta) = \frac{dN}{A d\Omega t \varepsilon}, \quad (2.2.4)$$

with dN being the bin entry, that corresponds to an effective number of events, A the detection area, $d\Omega$ the solid angle of the bin, t the dead-time corrected measurement time and ε the total efficiency.

As mentioned before one orientation of the telescope cannot cover the whole upper hemisphere. Therefore, measurements with different orientations have to be conducted and later on added. This was done by a weighted mean of the single measurements taking into account the statistical uncertainties of the individual measurements. Bins, that were not fully covered by a given measurement, are omitted from this procedure. The consistency of the different orientations was checked by filling the deviations between two measurements bin by bin into a histogram, which is shown in fig. 2.2.6, that yields the expected Gaussian distribution with $\sigma \approx 1$. The result of the weighted mean is a full map of the muon intensity of the upper hemisphere. From this the integrated muon intensity J can be calculated by integration of I over all angles.

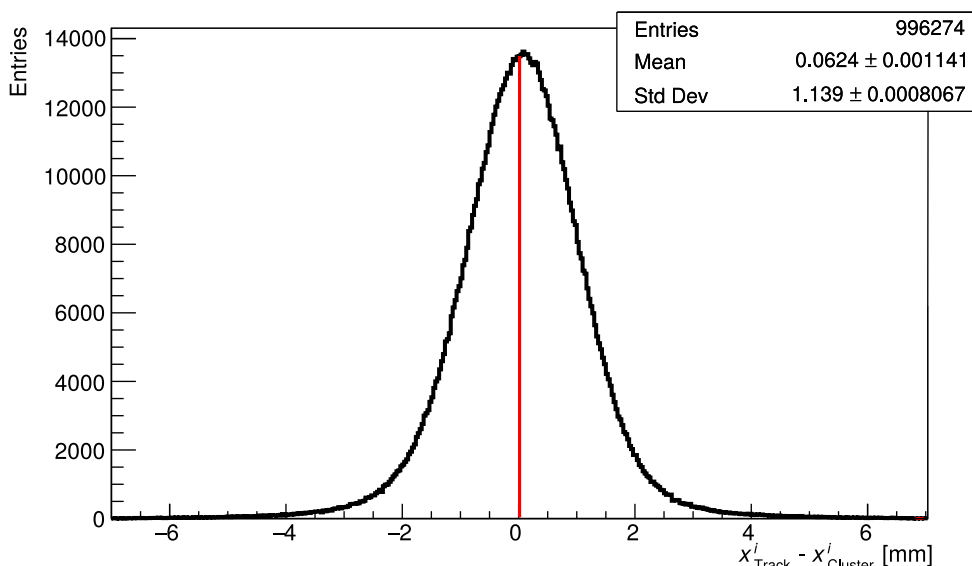


Figure 2.2.4: Histogram of the difference between the x coordinates of the calculated track point and the centre of the cluster in the channel data for a horizontal surface based measurement. The red line marks the mean of the distribution, which is later used in the analysis to correct the cluster coordinates. The standard deviation gives an upper limit for the angular resolution of the telescope. Note, that this plot was done with all tracks of the measurement for clarity, while for the pre-analysis only the first 2000 are used.

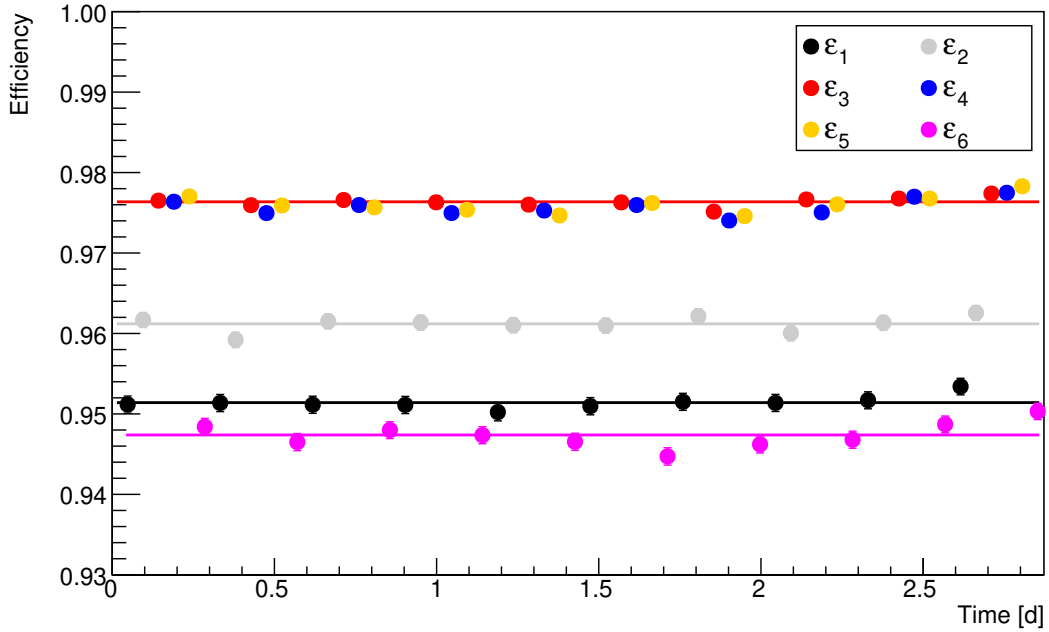


Figure 2.2.5: Efficiencies ε_i of the six chambers of the muon telescope for a measurement on the surface with ε_1 being the top and ε_6 the bottom one. The data are fit with a straight line and the lines for ε_4 and ε_5 are omitted for clarity.

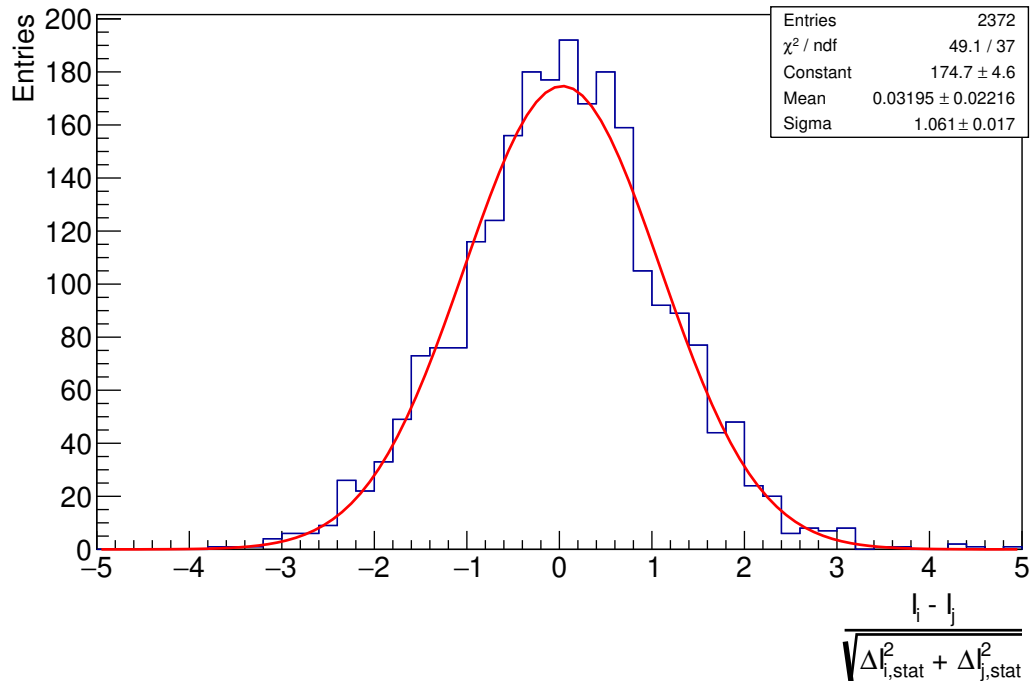


Figure 2.2.6: Bin entries of different orientations at the same bin of the polar histogram compared by dividing the difference of the two by their total statistical uncertainty for the measurement on "Hoher Stein". The red line shows a fit to a Gaussian distribution.

2.3 Measurements on the surface

For comparison and testing purposes several measurements were undertaken on the surface as well. However, these might not only include muon events, but also high-energetic electrons, which are mostly shielded in underground settings. In subsec. 2.4.2 it will be shown by simulations, that electrons of energies above 10 MeV are suppressed by the telescope by more than one order of magnitude. [Tan+18] gives the vertical intensity of electrons and positrons with an energy of above 10 MeV as $30 \text{ m}^{-2}\text{s}^{-1}\text{sr}^{-1}$, which would lead to a contribution of less than 3% for the surface measurements.

Two of those were done in building 620 on the campus of Helmholtz-Zentrum Dresden-Rossendorf (HZDR) at 280 metres above sea level (m.a.s.l.) and another on top of the observation tower "Hoher Stein", which is located directly above the tunnels of Felsenkeller at 200 m.a.s.l. For these measurements, durations of half a day per orientation of the telescope proved sufficient due to the high muon intensities.

The results of these measurements are shown in fig. 2.3.1. While the two measurements on the top of buildings show next to no characteristics, the one in the basement of the building 260 exhibits a strong influence by the wall of the building, which was right next to the telescope and is visible in the muon intensity by a line of reduced intensity. Further, the effect of the ceiling of the stories above can be seen by comparing the unshielded area in the direction of the window ($\varphi = 0^\circ$) to the one facing the building.

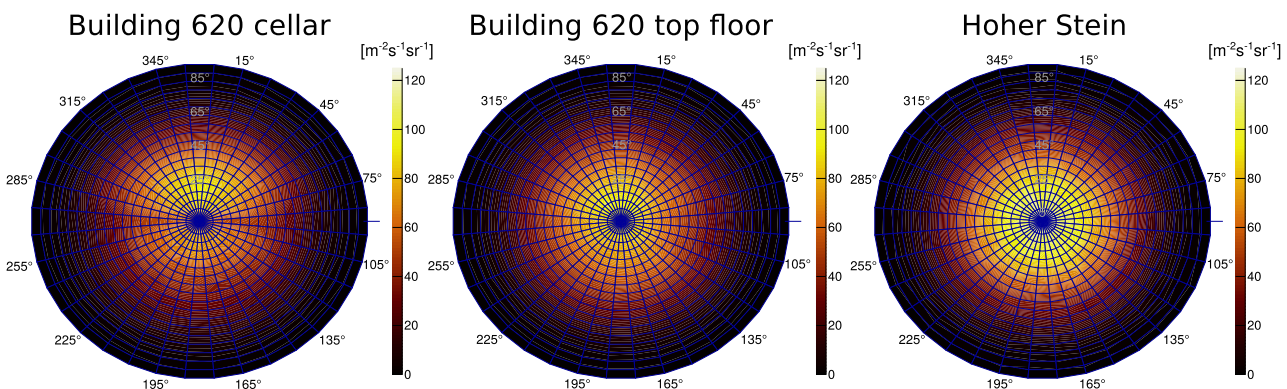


Figure 2.3.1: Intensity for three different positions on the surface, one in the basement of a three storied building at a outer wall (left), one on the highest story of the same building (centre) and one on top of the observation tower "Hoher Stein" (right). Note that the intensity maps are not oriented after the cardinal directions.

2.4 Measurements in Felsenkeller

The Felsenkeller site is located in "Plauenscher Grund" in Dresden, Germany. The terrain is dominated by the flat valley of the river "Weißeritz" at 140 m.a.s.l. and a steep cliff followed by a high plain 60 m above the site (fig. 2.4.1). The area was used as a quarry, that was turned into a brewery in the 19th century, which was then closed in 1991. During the 1850s nine horizontal storage tunnels were blasted into the cliff, which are interconnected at their ends. A plan of the tunnels is shown in fig 2.4.2. The overburden of the tunnels is characterized by 45 m of Hornblende monzonite, with a density of $(2.69 \pm 0.06) \text{ g/cm}^3$, measured from samples taken from tunnels VIII and IX, which are now the site of an underground accelerator facility. Measurements were undertaken at eight positions in the tunnels of Felsenkeller, four of them in tunnels VIII and IX, before construction of the laboratory took place:

- Position 1 deep inside the connection tunnel linking tunnels IX and VIII to all other tunnels
- Position 2 at the end of tunnel VIII
- Position 3 at the position of the later constructed measurement bunker
- Position 4 at the later constructed activation measurement bunker

Afterwards the laboratory was constructed, during which small parts of the ceiling of the tunnels was removed and a concrete building erected. These changes influence the here measured muon intensity only slightly, because they compensate each other. In addition to that four measurements in tunnel IV were done, where a γ -counting facility is present since 1982:

- Position 5 at the end of tunnel IV
- Position 6 in Messkammer 1 (MK1) shielded by 68 cm serpentinite rock and 2 cm old (i.e. pre-1945) steel for a total areal density of 200 g/cm^2
- Position 7 in Messkammer 2 (MK2) with 210 g/cm^2 areal density shielding, consisting of 6 cm old steel, 3 cm lead and 27 cm iron pellets.
- Position 8 in a workshop area (WS) surrounded by a thin composite wall

At each of these positions, seven measurements with different orientation of the telescope were taken (see fig. 2.2.2) for a duration of three to four days per orientation. For positions 1-4 this was done in two campaigns: the first one covered the vertical and horizontal measurements on all positions from June to July 2015, while later from March to May 2016 the 45° measurements were added. In this time period, there was also done a measurement in horizontal direction at position 1 as a comparison. For positions 5-8 all orientations were done subsequently from June to October 2016. Possible influences of this large timespan are discussed in subsec. 2.4.1.

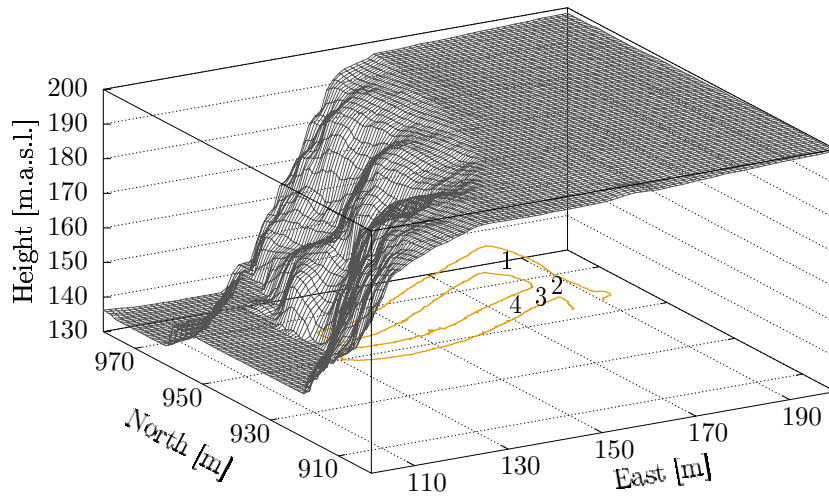


Figure 2.4.1: Terrain of the Felsenkeller site deduced from the DGM1 geodata. The axes are relative to the reference point (5409000,5654000) in the RD/83 system (see subsec. 2.4.2 for more details). The river valley of the Weißeritz connects to a flat plain, that is cut off by a steep cliff, that is followed by another plain. The measurement positions 1 to 4 are marked in the tunnels, 5 to 8 would be further south and are not shown here.

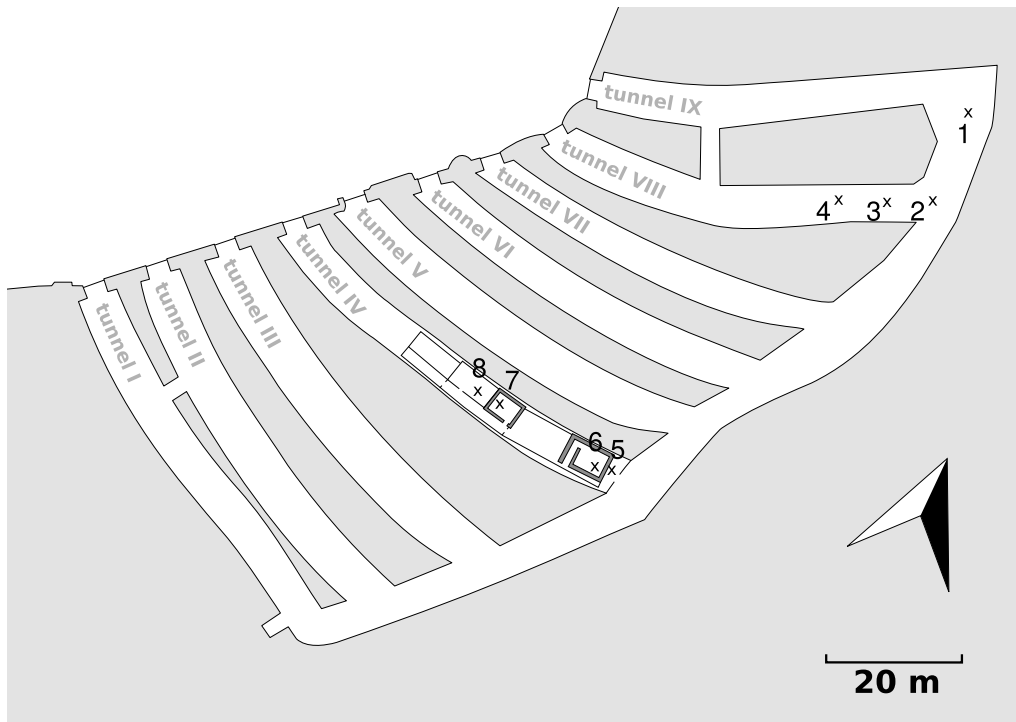


Figure 2.4.2: Map of the nine tunnels in the Felsenkeller underground site and the connection tunnel. Measurement points 1 to 4 in tunnels VIII and IX are marked as well as positions 5 to 8 in tunnel IV.

Position	θ_{max} [°]	φ_{max} [°]	I_{max} [m ⁻² s ⁻¹ sr ⁻¹]	J [m ⁻² s ⁻¹]
1	65±5	280±10	2.26(5)	5.0(4)
2	55±5	280±10	1.80(4)	4.6(5)
3	55±5	300±10	1.96(5)	4.9(4)
4	55±5	280±10	2.66(6)	5.4(4)
5	0±5	—	1.73(2)	4.6(4)
6	55±5	280±10	1.71(4)	4.7(4)
7	55±5	260±10	2.82(5)	6.0(4)
8	55±5	260±10	4.17(7)	7.0(4)

Table 2.4.1: Direction ($\theta_{max}, \varphi_{max}$) and value I_{max} of the highest muon intensity and the integrated muon intensity J for all measurement positions. For I_{max} and J , only statistical errors are shown.

In the following all measurements for one position were analysed as described in the previous section. The results are shown in fig. 2.4.3. All of them show a pronounced muon intensity in the vertical direction and a reduction in muon intensity for lower polar angles. However, there is an exception for this behaviour in all of the measurements at a polar angle of 55°, that coincides with the direction of the shortest distance to the cliff. The tunnels themselves, which are at $\varphi \approx 70^\circ$ and 250° , do not have a visible impact on the muon intensity in the binning chosen here.

A quantitative comparison (see tab. 2.4.1) shows, that the values for the second maximum differ. The positions deep inside the tunnels (positions 2, 5 and 6) have lower muon intensity in the direction of the cliff. However barring these differences, the integrated muon intensity is the same for all positions but positions 7 and 8. These are also the positions closest to the tunnel entrance and the cliff above tunnel IV is not as steep as for the other tunnels, so a higher muon intensity is expected there. With these values, the integrated muon intensity is suppressed by a factor of 30 to 40 in Felsenkeller compared to the surface (190 m⁻²s⁻¹ [Gri01]). The statistical uncertainties on the muon intensity range from 3% for small zenith angles to $\leq 12\%$ in the intermediate area to $\approx 20\%$ for $\theta = 85^\circ$ and up to 40% for single bins badly covered by the measurements, due to the low muon intensity.

Apart from these differences the muon intensity is homogeneous and falls off with a $\cos^n \theta$ -distribution, which is consistent with the flat plain over the tunnels. The exponent n of this function is dependent on the shielding of the measurement point. Therefore $n = 1.84 \pm 0.07$ for position 3, which is slightly lower than a measurement in a horizontal tunnel under Mont Blanc on the Italian side at a similar depth of 140 m.w.e. (metres water equivalent), where $n = 2$ [Cas+65]. The measurement at "Hoher Stein" yields $n = 2.12 \pm 0.07$. Both fits can be seen in fig. 2.4.4.

The quality of the shielding of an underground laboratory is often expressed in terms of the vertical depth of it. Barbouti provides an empirical fit describing the vertical muon intensity

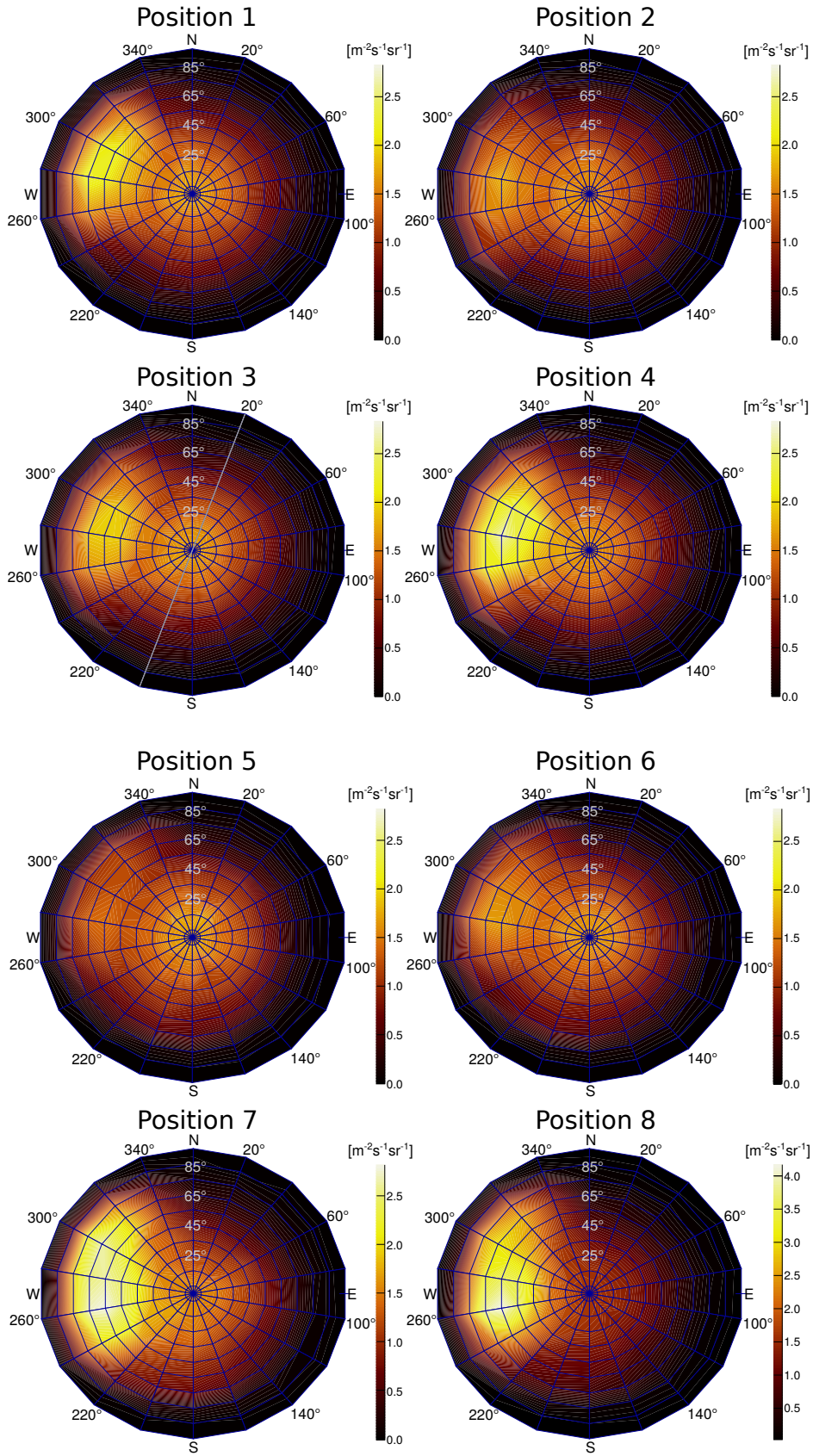


Figure 2.4.3: Muon intensities of the eight positions in Felsenkeller. Note the different colour scale for location 8.

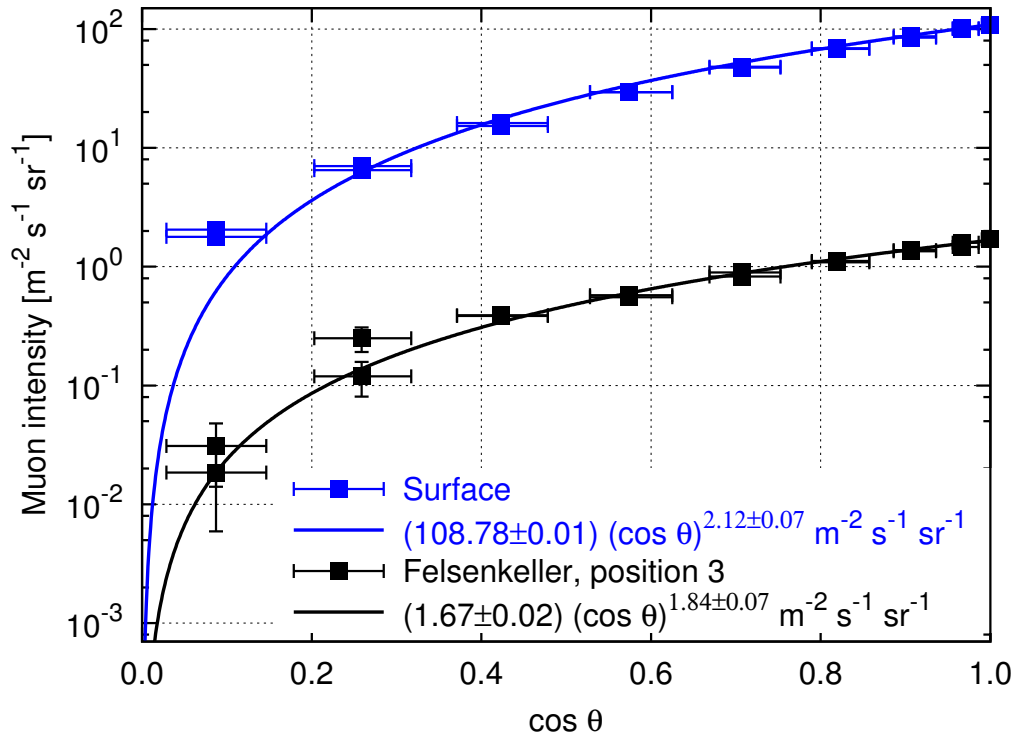


Figure 2.4.4: Fit of the surface measurement at "Hoher Stein" and the underground measurement at position 3 to $\cos^n \theta$. Each point represents a 10° wide bin in θ . The φ direction is marked in fig. 2.4.3 by a thin grey line. The horizontal error bars are chosen, so that 68% of the muon tracks are inside the area covered by the bin.

as a function of the depth from the top of the atmosphere. As can be seen in fig. 2.4.5 the measurements performed here, both in Felsenkeller and CAVE, Monaco, agree very well with this parametrization.

2.4.1 Systematic uncertainties on the muon intensity

Since the muon telescope saves no timing differences for the individual chambers, it is impossible to distinguish between muons coming from above and below. However, up-going muons are all induced by neutrinos and the intensity of these neutrino-induced muons can be measured in deep underground experiments and amounts to $10^{-8} \text{m}^{-2} \text{s}^{-1} \text{sr}^{-1}$ [Gri01], which is negligible for the here presented measurements.

During measurements spanning several days, the efficiency of the chambers (see fig. 2.2.5), the event rate and the muon rate remained stable (see fig. 2.4.6). Therefore, differences in the muon intensity between day and night can be ruled out.

Furthermore, if there are two muons passing through the detector in the data acquisition time window of $200 \mu\text{s}$, only the one with the better linear fit will be counted. This occurred in below 0.01% of the cases at the shallow-underground laboratory Felsenkeller.

As mentioned in sec. 2.3 the telescope can in principle also detect electrons above an en-

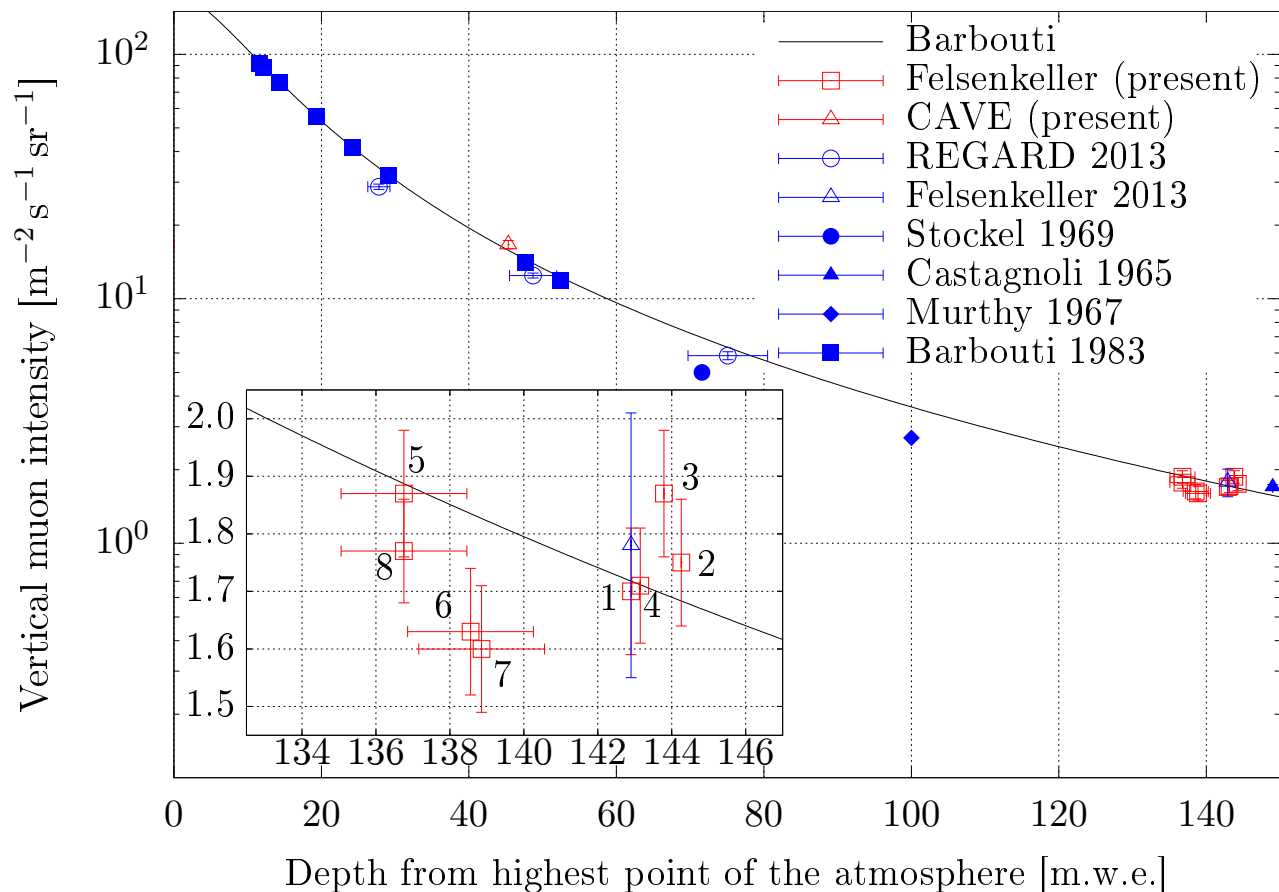


Figure 2.4.5: Vertical muon intensity as a function of depth from the highest point of the atmosphere. Measurements in Felsenkeller with a 4° opening angle, are shown in open red squares. The measurement in CAVE, Monaco (see sec. 2.5), also with 4° opening angle is shown as a red open triangle. Note, that to the purposed depth of the laboratory of 35 m.w.e. the depth of the atmosphere of 10.33 m.w.e. was added. Filled blue data points are taken from tables in [Gri01]. Previous data by the REGARD group in Budapest, Hungary are represented by the open blue circles [Olá16]. A prior measurement in Felsenkeller (open blue triangle) was adapted to the updated density of the rock [Olá+16]. The empirical parametrization by Barbouti *et al.* [BR83] is plotted as the black curve. In the inset a detailed view of the Felsenkeller measurements is presented in linear scale. Systematic errors on the depth due to the uncertainty of the density of the rock are not included in the horizontal error bars.

ergy threshold of 8 MeV [Ber+05]. Cosmic ray electrons are completely shielded by the rock surrounding Felsenkeller. However, muon-induced electrons might have enough energy to penetrate all layers of the detector. But simulations (see subsec. 2.4.2) show, that most will be scattered inside the telescope and therefore the electron track will be discarded.

2.4.2 Matching the measurements

In order to compare these measurements one calculation and two simulation based methods were employed. All three of them require detailed knowledge about the rock overburden and the geometry of the tunnels itself, as well as an atmospheric muon parametrization. From these, the muon intensity inside the tunnels can be derived. This was done exemplary for position 3, where the detectors for the in-beam spectrometry will be placed in the finished laboratory.

The data of the terrain was supplied by the official geodata "Digitales Geländemodell 1" (DGM1) with a grid of 1 m (see fig. 2.4.1). DGM1 is based on aircraft laser measurements, where the last echo point was used, to rule out vegetation. It has an uncertainty of 0.2 m for the grid points and 0.15 m for the elevation. The data in the ETRS89_UTM (European Terrestrial Reference System 1989, UTM zone 33) and DHHN2016 (Deutsches Haupthöhennetz 2016) elevation reference system surrounding Felsenkeller was kindly provided by the Staatsbetrieb Geobasisinformation und Vermessung Sachsen, Dresden. The tunnel data was supplied by three dimensional laser scans conducted by Ingenieurbüro Leibiger, Kesselsdorf in the RD83 system with the DHHN92 elevation system with a precision of less than 1 cm. The difference

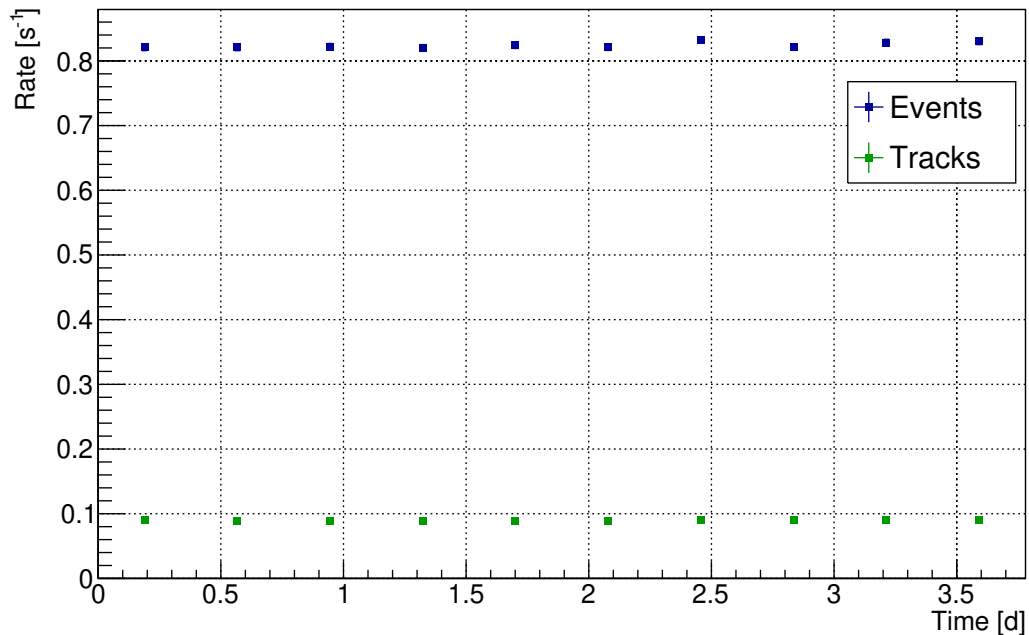


Figure 2.4.6: Event and track rate of the muon telescope for a measurement in tunnel IV of Felsenkeller. Both rates are stable over the whole measurement time.

between DHHN92 and DHHN2016 amounts to 3 cm at most for Saxony, which is neglected for the present purpose. Furthermore the ETRS89 data was converted to RD83, leading to an additional uncertainty of a few centimetres.

The muon parametrization was adopted from Tang *et al.* [Tan+06], that uses a modified Gaisser parametrization [Gai90]. While the latter is most commonly used for deep underground calculations and only applies for $E_\mu > 100 \text{ GeV}/\cos\theta$, the modifications by Tang ensure a validity for $E_\mu > 1 \text{ GeV}/\cos\theta$, which is sufficient for the overburden of Felsenkeller, and $\theta < 85^\circ$.

Calculation with the range-energy relation

The range by muons in rock can be approximated by the Gaisser range-energy relation [Gai90]:

$$E = \left(\frac{a}{b}\right) [\exp(bR_\mu) - 1], \quad (2.4.1)$$

with $a = 0.217 \text{ GeV m.w.e.}^{-1}$, $b = 4.5 \cdot 10^{-4} \text{ m.w.e.}^{-1}$ and R_μ the muon range in m.w.e. Based on this equation the cut-off energy can be calculated for a given slant depth, that describes the distance muons have to travel through the rock. Every muon with lower energy is supposed to be absorbed by the rock and secondary particles are neglected. The slant depth was calculated for a total of 60 azimuthal and 30 zenith bins by using the geodetic tunnel and terrain data. The mean distance from the measurement position to the surface and to the tunnel walls was calculated by filling the data points of the tunnels and the surface into the corresponding polar bin and then dividing by the number of entries in the bin. Furthermore, it was taken into account, that a muon might pass more than one tunnel by subtracting the total travel distance in the air of the tunnels from the distance to the surface. The total distance travelled through rock multiplied by its density $\rho = 2.69 \text{ g/cm}^3$ results in the slant depth in m.w.e. Using the slant depth and the range-energy relation, one can integrate the muon parametrization at the surface by Tang *et al.* starting at the cut-off energy, which results in the muon intensity at the desired position. The effective energy threshold for muons of the telescope itself is 30 MeV and was neglected for this calculation. With this the muon intensity was calculated for all 1800 bins. Afterwards the histogram was rebinned to the binning used for the measurements. The result of this procedure is shown in the right upper panel of fig. 2.4.7.

Monte Carlo simulation

As an independent approach the same data on terrain and tunnels was used in Monte Carlo simulations on GEANT4 (version 10.4) with the physics list "Shielding2.1 EMZ". This is a reference physics list of GEANT4 containing electromagnetic and hadronic physics. It is best suited for shielding, high-energy or underground applications.

In a first attempt the slant depth already derived for the range-energy calculation was used to simulate rock columns with a $10\text{ m}\times 10\text{ m}$ base and the slant depth as height. The material of the rock column is assumed to be monzonite, the composition of which is described in [Wal11]. Two million muons representing the muon parametrization were started at the top of each of these columns and propagated through it. In the end the surviving muons were counted. By multiplying the muon intensity on the surface given by the parametrization with the fraction of surviving muons, the muon intensity underground for one of the bins is derived. The result is shown in the lower left panel of fig. 2.4.7.

However this method would not include muons, that pass through the rock, but are scattered into another bin of the polar histogram. Also, the calculation of the slant depth relies on an approximation, by taking the mean distance of all available terrain data points for a single bin. Especially for abrupt changes in the terrain, for example at the bottom or top of the cliff or at the tunnel walls, this can lead to deviations. To test the impact of these systematic uncertainties of the prior simulation and also to explore the impact of secondary particles like electrons, the full terrain including the tunnels was modelled in GEANT4.

The DGM1 data was provided as a point cloud. To import this data into GEANT4 this point cloud was meshed and converted to the GDML format. First, an area of $300\text{ m}\times 300\text{ m}$ around the desired position was taken from the DGM1 data. Then data points describing the bottom of the rock at 120 m were added, in order to convert the point cloud of the surface to an actual volume. These were then imported to MeshLab, meshed and exported as an STL file, which was converted to GDML. For the tunnels a similar approach was undertaken with the difference, that the point cloud was sampled beforehand to reduce calculation time of the mesh.

With the geometry in place, muons representing the muon parametrization by Tang *et al.* were started in a dome above Felsenkeller aiming at the desired position, where a half-sphere with a diameter of 1 m is serving as detector. To cut calculation time short, the simulation focused on high zenith angles by the number of started muons at each θ following a $\cos\theta$ -distribution. With a total of 8.36 million muons propagated through the rock, it was ensured that the energy distribution of the muons was represented for all directions. Information on angles, energy and particle were taken for every started muon and every particle reaching the detector. The latter numbered 175000 muons. The number of muons reaching the detector divided by the started muons for a corresponding bin and multiplied by the muon intensity on the surface, then yields the lower right panel of fig. 2.4.7.

All methods agree with the measurement, but there are slight deviations visible as well. One is, that the maximum in north-western direction is more pronounced in all of the methods. Also for the highest $\theta = 85^\circ$ both simulations overestimate the muon intensity, while the range-energy calculation underestimates it. To better compare the methods quantitatively the

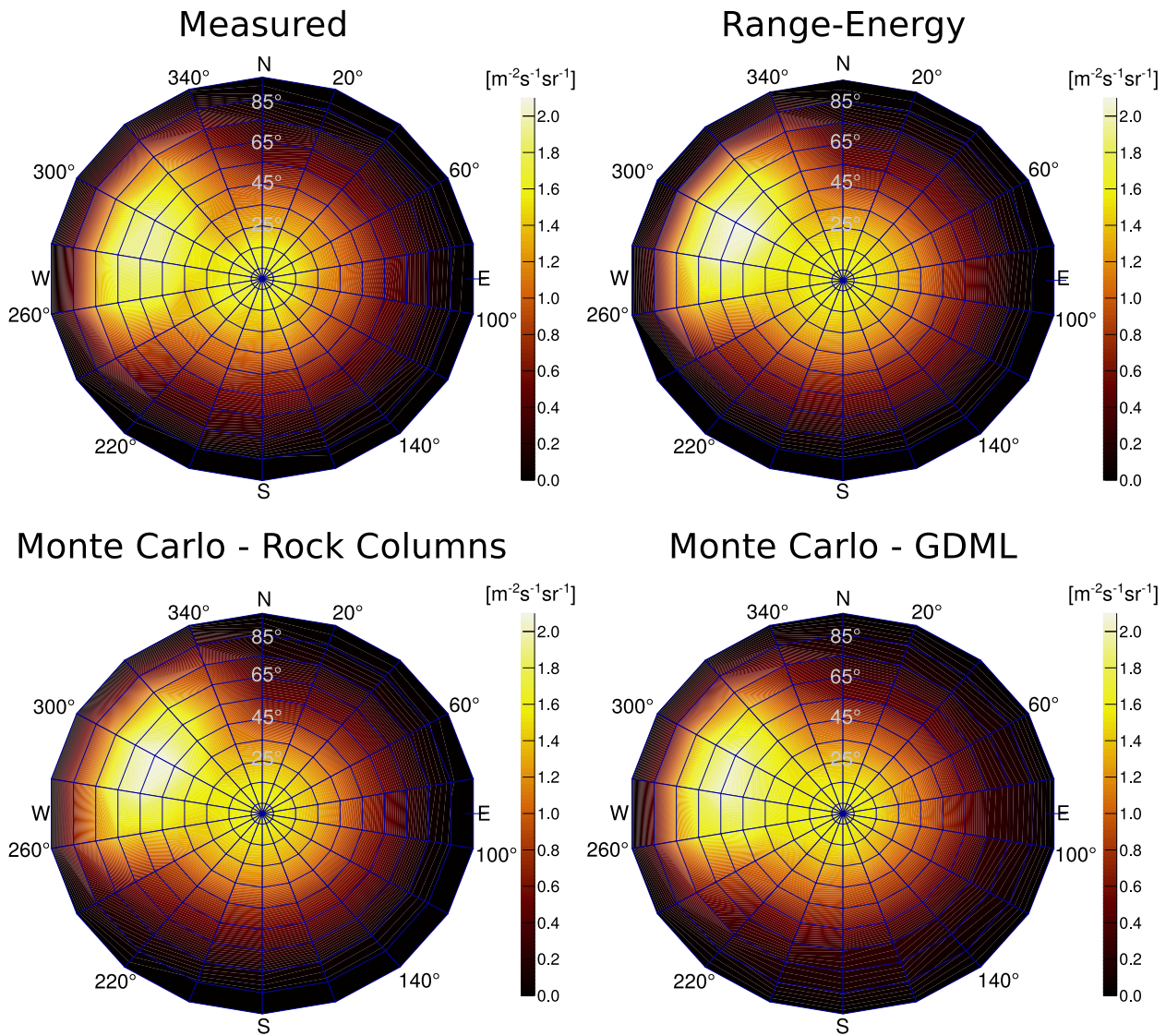


Figure 2.4.7: Comparison of the muon intensities of the measurement (upper left) with a range-energy calculation (upper right), a Monte-Carlo simulation propagating the muons through rock columns of a calculated depth (lower left) and a Monte-Carlo simulation with implementation of the surface and tunnel layout (lower right) at position 3. All methods agree very well with the measurement. However, in all cases the maximum in north-western is slightly more pronounced and for the range-energy calculation the muon intensity falls off faster for high θ angles. See text for a more detailed comparison.

residuals r_i in terms of σ were calculated for each bin as follows:

$$r_i = \frac{I_i - I_{\text{exp}}}{\sqrt{\Delta I_i^2 + \Delta I_{\text{exp}}^2}}, \quad (2.4.2)$$

with the muon intensity of the measurement I_{exp} , the muon intensity of the method I_i and their corresponding uncertainties. Note that the uncertainties for the simulation are only statistical, while for the range-energy calculation the main source of uncertainty is the slant depth.

All methods show a good agreement with the experiment, where the vast majority of points are within the 3σ uncertainty range. However, several outliers exist for all methods, that deviate as much as 16σ . These are contributed by bins with the highest θ , where statistics are low and the calculation of the slant depth error prone, because of the large area of terrain, that is included in one bin. The terrain data, used for the calculations, had to be limited. Therefore, some structures are not included, that might influence the muon intensity as well, i.e. the hill in south-western direction. Furthermore, the muon intensity at sea level by Tang *et al.*, which was utilized in all methods, deviates for $\theta > 85^\circ$ by up to 40%. For these reasons, these bins were omitted from the following analysis.

Fig. 2.4.8 shows the residuals of the different methods and the measurement. The σ parameter of the residual distribution shows, how well the method matches the measurement. The best agreement was reached by the range-energy calculation, which included the systematic uncertainties of the slant depth. The rock column simulation tends to underestimate the muon intensities and outliers are spread evenly in both directions. This results in the highest disagreement between rock column method and the measurement, where $\sigma = 3.43$. For the GDML simulations the muon intensity was slightly lower than in the experiment as well, but here the agreement is better with $\sigma = 1.65$. Therefore it is the second best description of the measurement. To better understand, how the deviations in the simulations come to pass, a systematic analysis would be necessary, for example by changing the density of the rock.

This suggests, that the applied method for calculating the slant depth overestimates the thickness of the rock. By calculating the same quantity with the absolute value of the numerator from eq. 2.4.2, one obtains the mean deviation from the measurement. Here, the range-energy calculation performs best with a value of 1.24σ , while the GDML simulation gives 1.65σ and the rock column simulation 2.76σ . For the latter, the uncertainty of the rock thickness was not taken into account, which might lead to this higher deviation. Highest deviations of up to 16σ were found within the bins for $\theta = 85^\circ$ for all methods. For the simulations these bins have the lowest statistics and do not take into account the uncertainty of the rock density. For the rock column simulation this factor is especially severe, because for a flat plain, the approximation for the mean rock thickness does not perform well for high θ . Here, the slant depth varies too much for different angles to be well described by the mean, that was used in the analysis. Furthermore it could be the case, that the description of the muon intensity is

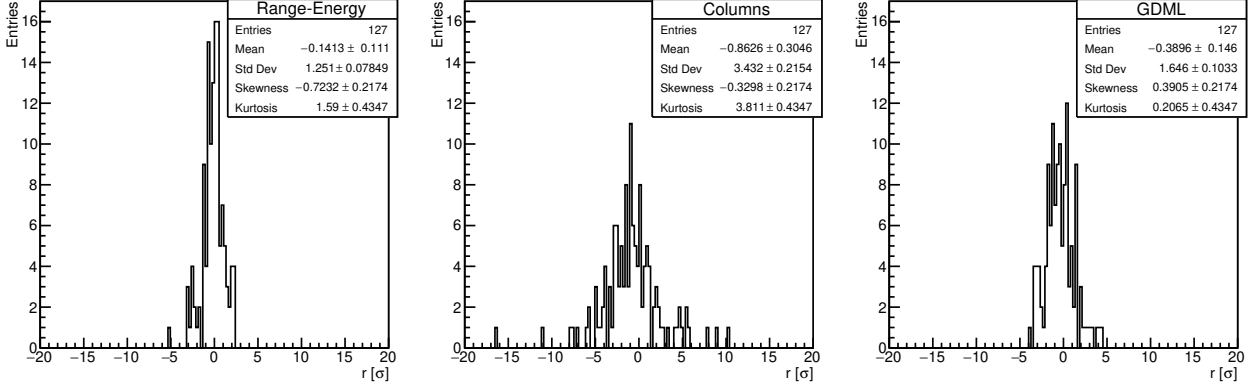


Figure 2.4.8: Residuals of the three different methods with the experimental data for all bins but the ones with the highest θ . All three methods, the range-energy calculation (left), the rock column simulation (middle) and the GDML simulation (right) agree with the experiment. Outliers are mainly contributed to bins with high θ . See text for a more detailed discussion.

lacking for nearly horizontal muons.

This does not affect the integrated intensities with $J_{\text{Column}} = (4.88 \pm 0.02) \text{ m}^{-2}\text{s}^{-1}$ for the rock columns, $J_{\text{GDML}} = (4.88 \pm 0.15) \text{ m}^{-2}\text{s}^{-1}$ for the GDML simulation and $J_{\text{range-energy}} = (4.9^{+0.5}_{-0.3}) \text{ m}^{-2}\text{s}^{-1}$ for the range-energy calculations, which all agree very well with the experimental result of $J_{\text{exp}} = (4.9 \pm 0.4) \text{ m}^{-2}\text{s}^{-1}$.

In addition to the muons, information on secondary particles, such as neutrinos, electrons, neutrons and their anti-particles, were saved as well. Out of these, neutrinos and neutrons do not contribute to the detector signal, though, neutrons play an important role in the background in HPGe detectors underground. Unfortunately, statistics for the neutrons, with only 3000 reaching the detector, are low and therefore a substantially higher amount of initial muons would be necessary to deduce the muon-induced neutron energy spectrum. Additionally, the simulation did not include the layout of the concrete bunker of the new laboratory, that impacts neutron production and moderation. In principle, the simulation could be extended to analyse neutrons, however this is outside the scope of this thesis and was already done for the Felsenkeller laboratory by Marcel Grieger (HZDR) with FLUKA [Gri+20].

If we take a look at the electrons and positrons, there were 18006 passing through the detector. All these electrons, that reached the telescope were propagated through the different layers of the telescope in a new simulation. Most of the started electrons get scattered on their way through the telescope and will not be counted as a muon track. If one counts only the electrons, where the polar angles in the last chamber differ by 20° for φ and 10° for θ , 920 of the 18000 remain (see fig. 2.4.9). It is noted, that this is a rather conservative estimation since all particles were propagated perpendicular to the telescope and therefore interacted with the lowest amount of material possible. The $< 0.5\%$ remaining uncertainty is included in the systematic error budget.

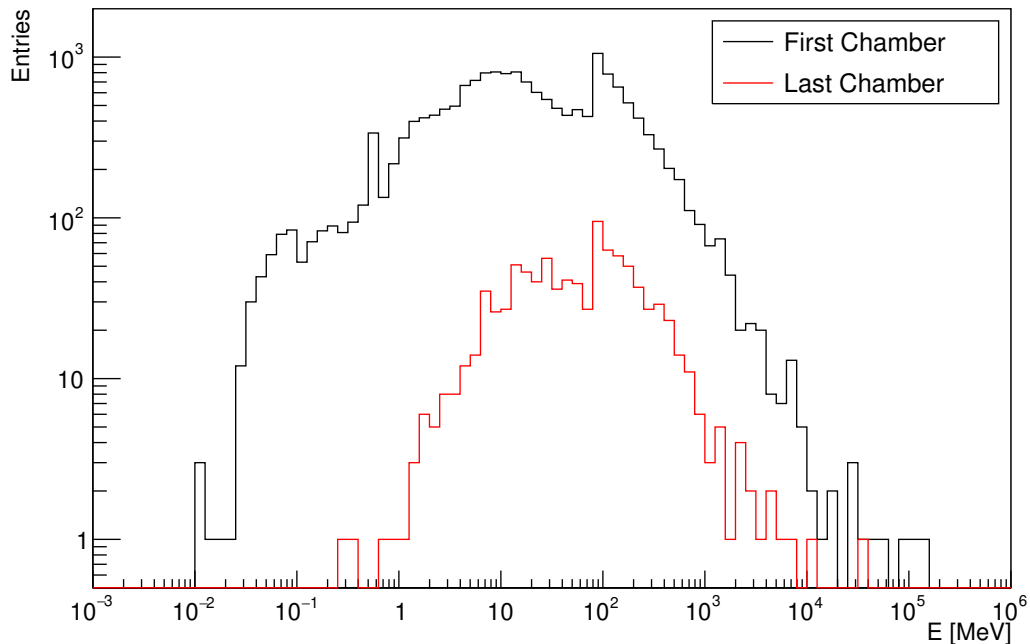


Figure 2.4.9: Energy spectrum of the electrons before (black) and after (red) passing through the telescope in double-logarithmic scale. Only electrons, that differ less than 20° for φ and 10° for θ were counted for the latter.

2.4.3 Temperature Correction

The detailed description of the terrain enables the determination of the influence of temperature fluctuations on the muon intensity as well. As mentioned in sec. 2.1.1 the temperature of the atmosphere impacts the muon intensity underground. The effect can be quantified, if the geometry of the rock above the laboratory and the temperature in different layers of the atmosphere is known.

All calculations in this subsection follow closely the paper by the MINOS collaboration [Ada+10] and the one by the Daya Bay Collaboration [An+18].

They consider the atmosphere of the earth to be an isothermal body with an effective temperature T_{eff} , that is calculated by multiplying the temperature in different layers of the atmosphere with a weight function. The change in the muon intensity I_μ can then be parametrized with the temperature coefficient α_T as follows:

$$\frac{\Delta I_\mu}{I_\mu^0} = \alpha_T \frac{\Delta T_{\text{eff}}}{T_{\text{eff}}^0}. \quad (2.4.3)$$

The data for the temperature is derived from the data of the European Centre for Medium-Range Weather Forecasts (ECMWF). They provide an interpolation for a specified location based on a global atmospheric model for temperatures at 37 discrete pressure levels ranging from 1 to 1000 hPa with a time resolution of 6 h. This dataset was employed to calculate T_{eff} for Felsenkeller during the timespan of the measurements (fig. 2.4.10).

Knowing the effective temperature, α_T needs to be determined to calculate the change in muon intensity. This coefficient is mainly dependent on the depth of the laboratory, which can be described by the averaged threshold energy $\langle E_{\text{th}} \cos \theta \rangle$. This quantity was calculated for Felsenkeller by using the range-energy approach as described in subsec. 2.4.2. The energy threshold for a given angle was then multiplied with $\cos \theta$ and weighted by the muon intensity in the corresponding bin, which results in $\langle E_{\text{th}} \cos \theta \rangle = (25.5 \pm 1.0) \text{ GeV}$. It is noted, that the averaged threshold energy is sensitive to the shape of the overburden, not only to the vertical depth. A hypothetical Felsenkeller with a completely flat overburden would have $\langle E_{\text{th}} \cos \theta \rangle = 28.8 \text{ GeV}$. With this information the temperature coefficient α_T can be calculated theoretically [Ada+10]. Further, an uncertainty analysis was performed in this paper, which states, that uncertainties on the input parameters contribute with 3%, while the main error budget is driven by the uncertainty of the mean energy threshold. Taking this into account yields $\alpha_T = 0.265 \pm 0.014$ for the Felsenkeller laboratory. The mean temperature of the upper atmosphere at Felsenkeller throughout the year is 223.5 K. The changes during the measurement period, displayed in fig. 2.4.10, have a maximum of 8%. Therefore, the maximum seasonal change in muon intensity is 2% following eq. 2.4.3 and is taken into account in the total systematic uncertainty.

2.4.4 Other temporal effects on the muon intensity

Next to the temperature there are other effects that can influence the muon production and therefore the muon rate in an underground laboratory. Changes in the pressure would also affect the density in the atmosphere. However the effect is far lower than the temperature one, with the barometer coefficient $\beta \approx 0.02\%/mb$ [Sag86] and therefore neglected.

Another temporal effect on the muon intensity is the solar cycle. Experiments on the muon intensity running over long periods of time exhibit an anti-correlation between intensity and the solar cycle with a 11 and 22 year periodicity, which is in the order of a few percent [Men+16] and was taken into consideration for the systematic uncertainty as well.

In the future, a permanent muon veto in the activity measurement bunker will be installed, which will take into consideration the results of this thesis and will collect data on the muon intensity continuously. The results of these measurements can be used to further investigate the changes of the muon intensity caused by temperature and barometric pressure fluctuations, as well as the solar cycle, in Felsenkeller.

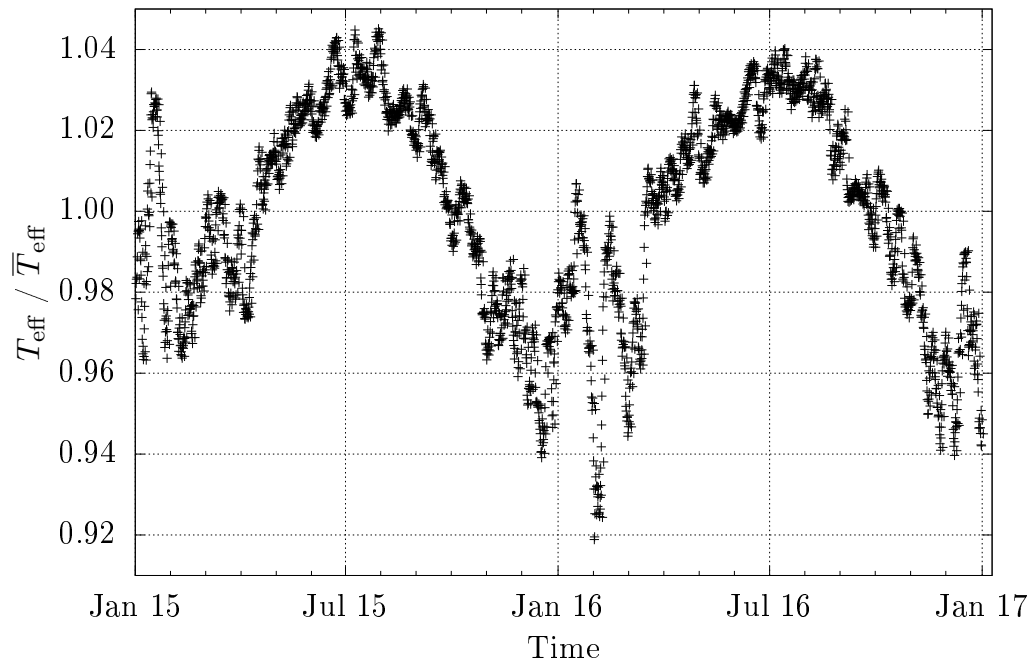


Figure 2.4.10: Deviation from the effective temperature from January 2015 to December 2016 for Felsenkeller during which the measurements took place. The maximum deviation is 8% from the mean effective temperature of 223.5 K.

2.5 Measurements in the IAEA Monaco

The IAEA hosts an environment laboratory in Monaco, which is used for a variety of applications, for example characterisation of reference materials, low-level radioanalytical services and applied research in the fields of environmental pollution and tracer studies. It also contains the underground laboratory CAVE, that is located in an underground car park. While the vertical depth is estimated to be 45.33 m.w.e., including the depth of the atmosphere, [PCL04], the amount of shielding material in other directions is hard to determine, because of the unique geometry of Monaco. Not only is the city located at the foot of a mountain range spanning from the south-west to north-east, but there is also another hill in south-eastern direction with a height of ~ 30 m (see fig. 2.5.2). In addition to that many buildings in Monaco have extensive cellars and the laboratory itself is positioned in-between the entrance and exit driveways of the car park. Therefore a simulation based analysis, as done in subsec. 2.4.2, is not possible for CAVE. So, an experimental approach was deemed necessary to investigate the background components in this underground laboratory.

As it is possible to achieve a better angular resolution in this relatively shallow underground laboratory, the measurement time per orientation was extended to at least one day for the horizontal and 45° orientations and two and a half days for the vertical orientation. The telescope itself was positioned on top of the active shielding of the HPGe detectors in the laboratory (see fig. 2.5.1).

The result of the measurements is shown in fig. 2.5.3, note that the number of bins in φ direction

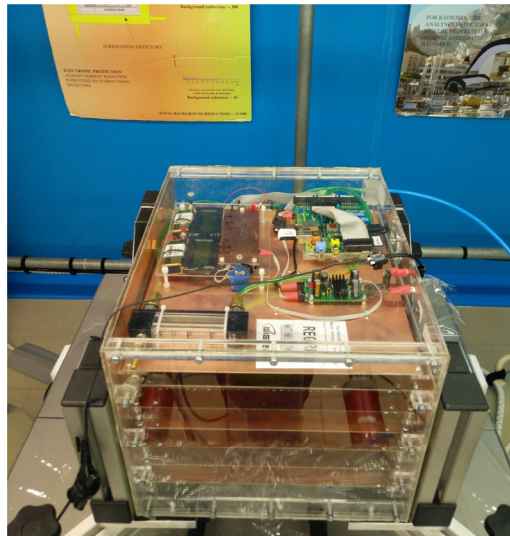


Figure 2.5.1: Position of the muon telescope in the IAEA shallow-underground laboratory CAVE in Monaco for the horizontal measurement. It was placed directly on the active shield of the HPGe detector.

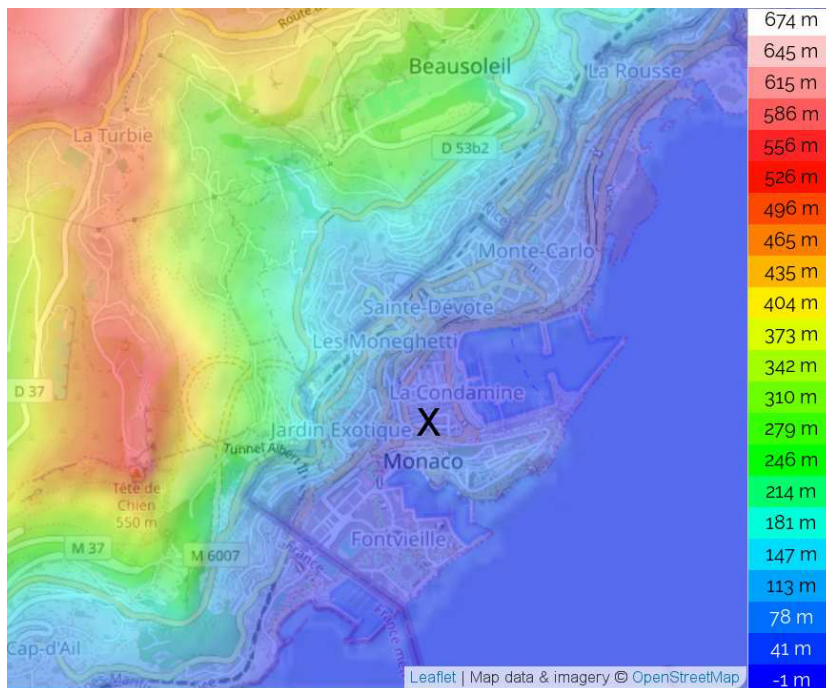


Figure 2.5.2: Elevation map of Monaco. The position of CAVE is indicated by the cross marker. Taken from [OVH20].

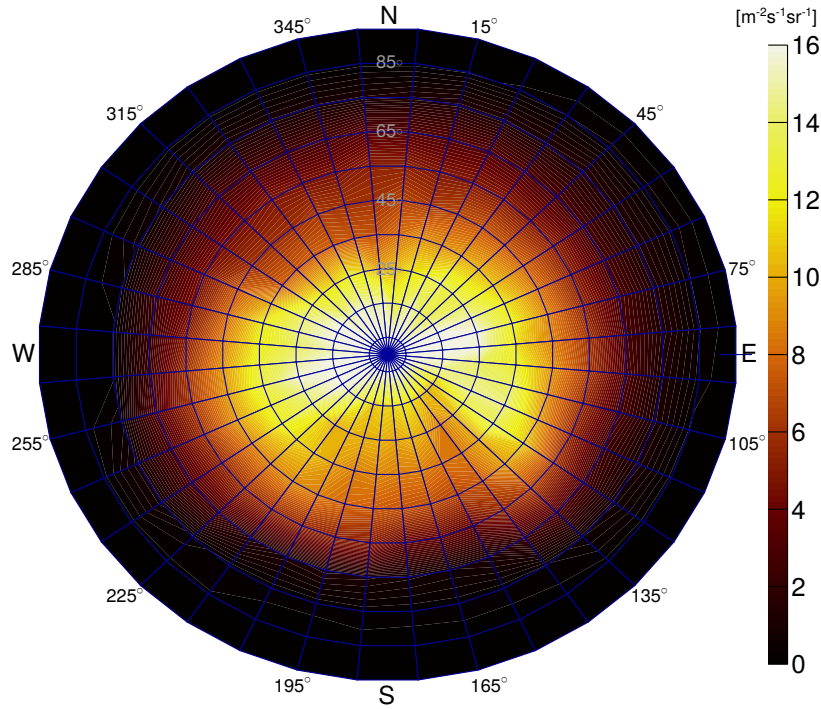


Figure 2.5.3: Muon intensity in the shallow-underground laboratory CAVE in Monaco. The intensity is inhomogeneous due to the varying overburden. Note, that the colour scale is increased by a factor of 8 compared to the Felsenkeller measurements.

is doubled compared to the measurements in Felsenkeller. Remarkably, the muon intensity is quite inhomogeneous; the vertical muon intensity is with $(15.825 \pm 0.008) \text{ m}^{-2} \text{ s}^{-1} \text{ sr}^{-1}$ slightly lower than the two maxima at $\theta = 15^\circ$ with $(17.5 \pm 0.5) \text{ m}^{-2} \text{ s}^{-1} \text{ sr}^{-1}$ to the east and $(16.8 \pm 0.5) \text{ m}^{-2} \text{ s}^{-1} \text{ sr}^{-1}$ to the west, that are caused by the roadways to the car park. Furthermore, it is visible, that from $\varphi = 35^\circ$ to 125° and in western direction, where plains reach into the sea and therefore less shielding is present to the muons, the muon intensity is enhanced. To the north, the effect of the mountain range is visible, while the hill to the south-east can be seen in the higher zenith angles. The lower angles might be shielded by the building above the car park. The integrated intensity is $J = (32.3 \pm 0.4) \text{ m}^{-2} \text{ s}^{-1}$.

2.5.1 Calculation of the averaged threshold energy

For Felsenkeller the averaged threshold energy $\langle E_{th} \cos \theta \rangle$ could be calculated from the data of the surrounding rock. This is not possible for CAVE. However, the muon intensity was measured and with that the threshold energy for a given angle can be calculated as the lower bound of the integral over the muon spectrum at sea. This was evaluated by the `Eval` function of Wolfram Mathematica [Inc] for all bins. Averaging the resulting energy thresholds as described in subsec. 2.4.3 yields $\langle E_{th} \cos \theta \rangle = (6.46 \pm 0.18) \text{ GeV}$, which is a factor of 3.6 lower

than in Felsenkeller. The uncertainty was calculated by rerunning the Mathematica script with the lowest and highest muon intensities $I - \Delta I$ and $I + \Delta I$ for each bin.

3 Re-installing and testing the sputter ion source for the Felsenkeller accelerator

The Felsenkeller accelerator facility hosts two ion sources, an internal one for ion beams of noble gases and hydrogen and an external one for all other ion species. This chapter will report on the external ion source. Sec. 3.1 gives a general overview of the ion source, while sec. 3.2 will report on first tests at the Rossendorf campus. This will be followed by the setup at the Felsenkeller laboratory in sec. 3.3 and improvements to the ion beam current in sec. 3.4. Additionally, a magnetic analysis of the ion types contained in the beam, was performed in sec.3.5. The last section,3.6, describes a realignment of the ion source.

3.1 The ion source

The external ion source installed at the Felsenkeller is a 134 sample multi-cathode source of negative ions by caesium sputtering (134 MC-SNICS) manufactured by NEC [Log+99]. It was part of the accelerator facility in York, where it was in use for accelerator mass spectrometry from 1999 to 2012 [You+08] and afterwards transported to Dresden, Germany.

The ion source produces negative ions by sputtering samples with caesium ions. A schematic of the source is shown in fig. 3.1.1. Caesium, which is contained in a stainless steel cylinder at the bottom of the ion source is heated up by a heating coil and caused to evaporate. Then it is guided by a heated canal into the evacuated source interior between the ionizer and a caesium-focus lens. Here it is ionized by the heat of the ionizer and, now positively charged, accelerated by the voltage of the cathode and focused by the lens. However, not all caesium is ionized, a fraction also condenses on the cooled surface of the sample. This thin caesium layer is now bombarded by the caesium beam, sputtering the sample and the thin layer on top of it. The sputtered atoms have a chance to strip an electron off the condensed caesium and, in turn, become negatively charged. These negatively charged ions are then accelerated and extracted from the ion source by the voltages of the cathode, the extractor and the bias. Furthermore, they are focused by two lenses: the caesium-focus lens and an einzel lens positioned behind the extractor. Extracted electrons are scattered out of the beam by a quadrupole consisting

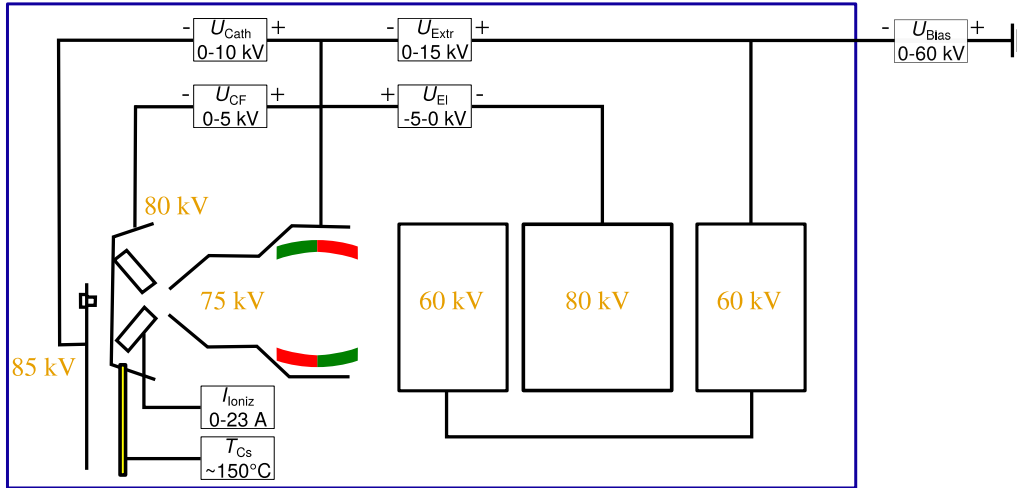


Figure 3.1.1: Schematic of the 134 MC-SNICS installed as the external ion source in Felsenkeller. All power supplies in the blue cage are on the voltage provided by the bias. Caesium is fed into the source through the yellow pipe from the caesium oven, ionized by the ionizer, accelerated by the cathode voltage U_{Cath} and focused by the caesium focus U_{CF} onto the sample. Sputtered sample atoms are ionized by a layer of condensed caesium and are extracted by U_{Cath} and the extractor voltage U_{Extr} . Behind this, a permanent magnet is installed to scatter accelerated electrons out of the beam, followed by the einzel lens with voltage U_{El} . The maximum possible potentials of each part are marked in orange.

of permanent magnets behind the extractor.

The source hosts 134 samples in a wheel, that are enclosed by the sample holder. During operation, the sample can be switched in seconds by turning the wheel pneumatically. This ensures nearly constant operation for a long duration of time without breaking the vacuum. If the cathode wheel needs to be changed, a gate valve can be lowered, that shuts out the caesium containing parts of the source. After this, the back of the ion source can be vented and the cathode wheel exchanged without danger of exposing the highly reactive caesium to air.

After exposing the cathode wheel to air, the burning-in phase of a sample, defined as the time until the maximum current is reached, will take several hours compared to just switching the sample, where maximum current is reached in about an hour.

3.2 Setup at HZDR

First tests to extract a carbon beam were undertaken at the HZDR in Rossendorf in the framework of Martina Koppitz' bachelor's thesis [Kop17] under my supervision. The setup is shown in fig. 3.2.1. It consisted of the ion source directly connected to an electrostatic analyser, followed by an electrostatic steerer, a slit system, a beam profile monitor and, at the end, a Faraday cup, where the beam current was measured. However, the whole setup was

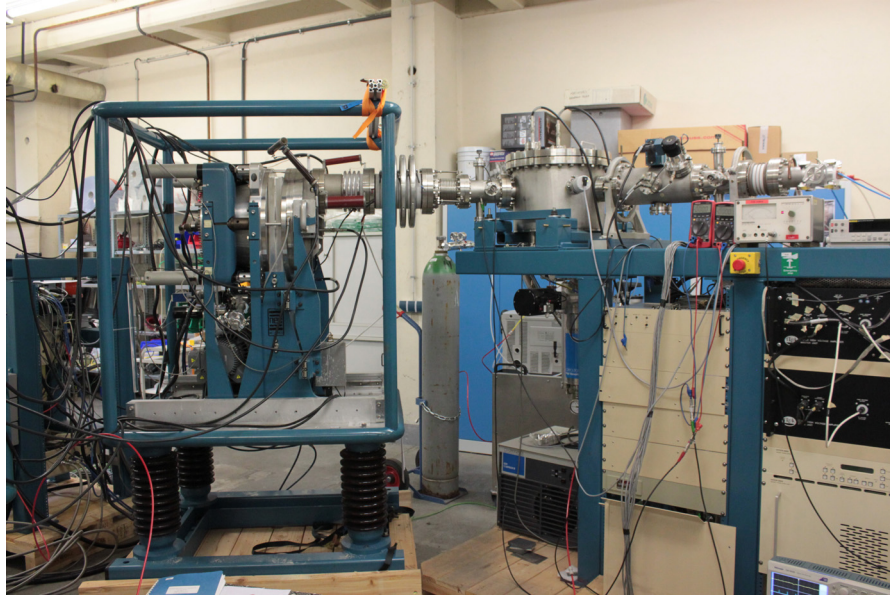


Figure 3.2.1: Ion source test stand at building 622 at HZDR. The ion source is directly connected to 45° electrostatic steerer, followed by a slit system, a beam profile monitor and a Faraday cup. The whole setup was positioned on wooden pallets and aligned with the help of a laser.

positioned on wooden pallets and only roughly aligned. Furthermore the Faraday cup was not suppressed for secondary electrons and there was no magnet to filter for specific ions. The sample holders were made of aluminium with a hole of 1.1 mm in the centre. This hole was filled with pencil lead. The beam energy was limited to 30 keV due to radiation safety.

3.2.1 Results at HZDR

Despite these issues, the beam could be extracted from the source and focused onto the Faraday Cup, where currents of up to 45 μA were reached. However, this current displays the sum of all negative ions extracted from the source minus the secondary electrons lost because of the lacking secondary electron suppression.

After that, aluminium sample holders with 1 mm and 2 mm diameter holes were filled with carbon rods. A drawing of these can be found in fig. 3.2.3 and a comparison of the ion current over time in fig. 3.2.2. The 2 mm sample holder reaches high ion current in the beginning and then gradually falls off until it drops to a low beam current after 13 h. The 1 mm one shows the same behaviour in the beginning, however the current eventually reaches a plateau, with only very slowly decreasing current on the Faraday cup over time. Since higher ion beam current is more desirable for experiments in nuclear astrophysics, later on only sample holders with a 2 mm hole were used.

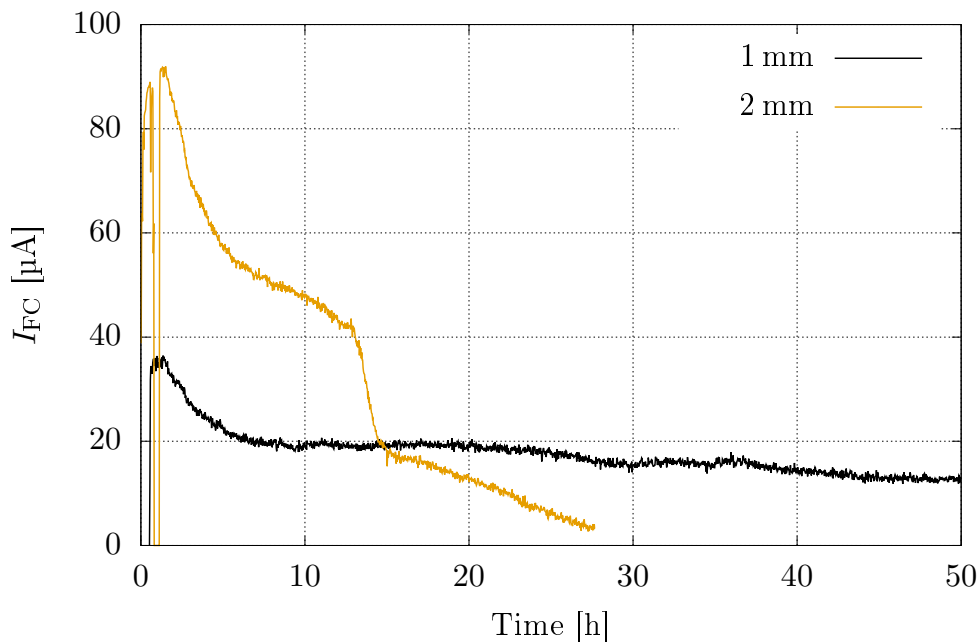


Figure 3.2.2: Comparison of the ion beam current over time for two different sample holders: one with a 1 mm diameter hole and one with a 2 mm one.

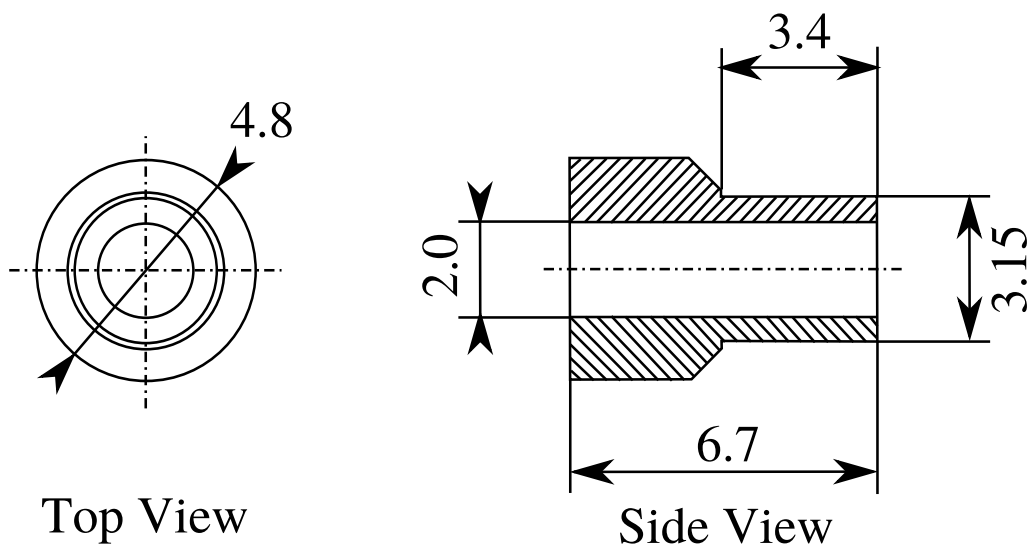


Figure 3.2.3: Top (left) and side view (right) of the sample holders used in the external ion source. All units are in mm. At HZDR aluminium holders with a 2 mm (shown in the drawing) and a 1 mm core drilling were used. At Felsenkeller only 2 mm holders of aluminium or copper were installed.

3.3 Setup at Felsenkeller

After these successful tests at HZDR in Rossendorf the ion source was transported to Felsenkeller and installed in the air-conditioned laboratory at the end of tunnel IX. A theodolite was employed for the alignment of the beamline. Unfortunately, since it is not possible to look through the ion source with this instrument, the source itself was aligned with lasers. This had to be corrected later on (see sec. 3.6).

In addition to the setup at HZDR, there is a slit system (SLS1), an additional Faraday cup (FC1), that gives information on the total extracted beam current, and a vertical electrostatic steerer (YS1) directly behind the source. This is followed by an electrostatic analyser (ESA) deflecting the beam by 45° and after that a magnet, that bends the beam by 90° into another Faraday cup (FC2). Therefore, it is possible to measure the beam current of a certain ion type, since the magnet is sensitive to m/q of the ion, where $q = -1e$ for all ions extracted from this type of ion source.

After that there are an additional electrostatic steerer, both vertical (YS3) and horizontal (XS1), and an einzel lens (EL). This is the same setup, that was used in York, with a slit system at the desired focus point of each focusing element. A schematic of the setup is shown in fig. 3.3.1.

The ion source could now be operated at an extraction voltage of 60 kV. This voltage is the sum of the cathode, the extractor and the bias voltage and was used for all following tests and measurements, which were conducted with the help of Julia Steckling, who published parts of the results in her bachelor's thesis [Ste19] under my supervision.

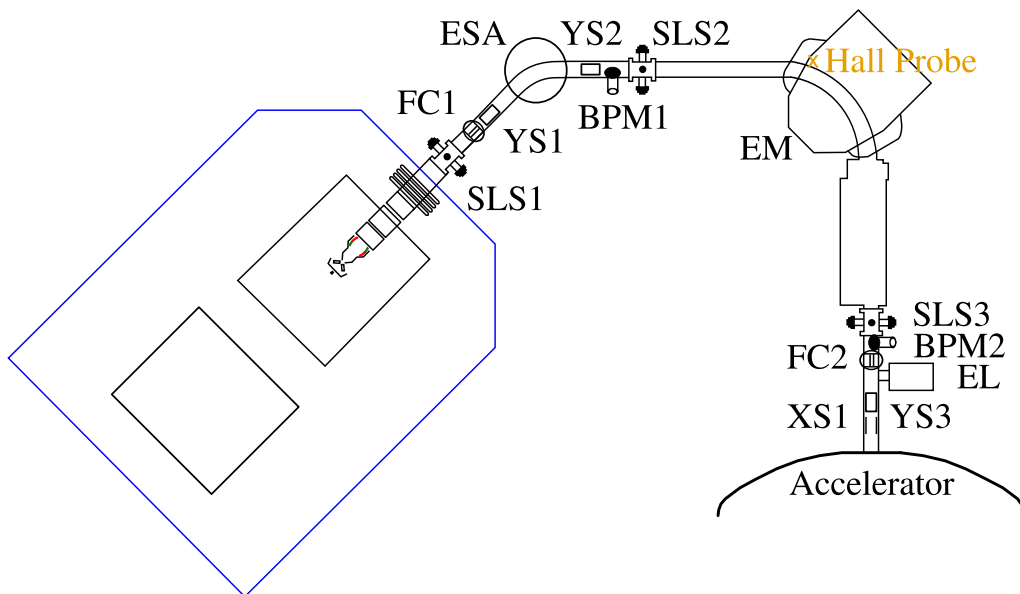


Figure 3.3.1: Setup of the beamline leading from the ion source to the injection of the beam into the accelerator. The position of the Hall probe is marked in orange.

3.4 Improvements of the ion source for carbon beam

There are several possibilities to increase the ion current extracted by the MC-SNICS, which is important to ensure high statistics in nuclear astrophysics accelerator experiments. One possible option is to increase the number of ions created. This could, in principle, be done by increasing the amount of caesium ions, that impinge on the sample, by increasing the oven and the ionizer temperature. However, both options are not possible, because more caesium in the source will lead to more condensation on the isolating parts of the source. Condensed caesium is conductive and will cause breakdowns of the high voltages. The ionizer was running at the highest power recommended by NEC during the whole time of operation. Nevertheless, the voltage of the caesium focus and the cathode can increase ion production as well. The first, because more caesium ions will hit the sample, the second, because the sputtering process is depending on the energy of the caesium ions.

The other option is improving the extraction of the ions. Here, the caesium focus and the cathode voltage are of importance as well, because they will influence the produced ions in addition to the caesium ions. Then there is the extraction and the bias voltage, as well as the einzel lens voltage. However, tests showed, that the extracted current is best at the maximum extraction voltage of 15 kV and the bias voltage has only a minor impact on the ion current. Therefore, the latter was used to keep the energy of the extracted ions at a constant 60 keV, when other parameters were changed.

A very reliable and stable default setting, that yields about 40 μA of $^{12}\text{C}^-$ at FC2 and was used for the experiment described in chap. 5, is achieved with the following parameters:

- a cathode voltage U_{Cath} of 5 kV,
- an extraction voltage U_{Extr} of 15 kV,
- a bias voltage of U_{Bias} of 40 kV,
- a caesium focus voltage U_{CF} of 2 kV,
- a einzel lens voltage U_{El} of 0 V,
- an ionizer current I_{Ioniz} of 23 A and
- an oven temperature T_{Cs} of 140°C

Setups with higher currents will be described in the following subsections.

3.4.1 Influence of the cathode voltage

As already mentioned, the cathode voltage influences the energy of the sputtering caesium ions as well as the ion optics. The thickness of the caesium layer on top of the carbon was

assumed to be mono-atomic with 0.26 nm [Sla64]. A thicker layer would shift the sputter yields dramatically in favour of the caesium, so that nearly no carbon is sputtered any more. SRIM-2013 [ZZB10] calculates the following sputter yields with the "Monolayer Collision Steps / Surface Sputtering" option and an angle of incidence of 0°:

U_{Cath} [kV]	Y_{C}	Y_{Cs}
3	0.24	1.31
5	0.40	1.86
7	0.53	2.30

Table 3.4.1: Sputter yields Y_i for different cathode voltages U_{Cath} and a 0.26 nm Cs layer on top of the carbon. The calculation was done with SRIM-2013 with the "Monolayer Collision Steps / Surface Sputtering" option for 10000 started Cs ions.

It is apparent, that the sputter yield rises with the energy of the Cs^+ ions in the energy range under study here. However, the sputtered atoms need to be ionized as well, so ionization efficiency might go down for increasing sputter yield.

During the measurements, the cathode voltage was increased in 0.5 kV steps. For each measurement point all other focus voltages were adapted to maximal current of $^{12}\text{C}^-$ on FC2, which resulted in an increase of both caesium focus and einzel lens. The bias voltage was modified, so that the total beam energy is constant at 60 keV. Unfortunately, the ion source became unstable with breakdowns for cathode voltages of above 6.5 kV and the ionizer power supply went out for periods of time, so that no points could be measured for higher voltages. This is thought to be caused by a badly focused beam at these voltages, where parts of it might hit the ionizer. A good beam focus was achieved with a ratio of 1:3 for U_{Cath} to U_{Extr} . The maximum voltage of the extractor is at 15 kV, so that it can not be adapted to higher cathode voltages. The results are displayed in tab. 3.4.2. The $^{12}\text{C}^-$ current increases with the cathode voltage and did not reach the maximum yet.

In previous measurements, however, the ionizer problem was not as severe and a maximum current of 172 μA was reached at a cathode voltage of 7.5 kV, $U_{\text{CF}} = 5$ kV and $U_{\text{El}} = 1.5$ kV with another sample. Above this voltage the beam could not be focused well enough, which led to a decrease in $^{12}\text{C}^-$ current. This ion current value is in agreement with the ones given

U_{Cath} [kV]	I_{FC2} [μA]
5.0	68
5.5	123
6.0	147
6.5	160

Table 3.4.2: Dependency of the cathode voltage U_{Cath} of the ion source on the ion beam current I_{FC2} for one sample. The current of $^{12}\text{C}^-$ increases with the cathode voltage and the maximum is not yet reached at 6.5 kV. During the measurements all other parameters were adapted to maximum current and a beam energy of 60 keV.

in the NEC data sheet [Cor17], that states, that 100 μA are typical, but $^{12}\text{C}^-$ currents of up to 200 μA can be extracted.

3.4.2 Influence of the caesium focus

The caesium focus (see fig. 3.1.1) has two tasks: to focus the caesium beam onto the sample and to guide the ionized sputtered atoms into the extractor. Since the focus point is energy-dependent, higher cathode voltages also require higher focus voltages. At $U_{\text{Cath}} = 7.5\text{ kV}$, the caesium focus voltage had to be at the maximum of 5 kV for the caesium, which leads to an overfocus for the ion extraction, that can be compensated by the einzel lens.

During operation of one sample, the hole sputtered into the sample by the caesium will grow continuously. Therefore, it is necessary to adapt the caesium focus to the increasing distance of the sample surface. Tests with the reliable setup at $U_{\text{Cath}} = 5\text{ kV}$ have shown, that, to ensure maximum possible ion current, the caesium focus needs to be changed by about 100 V every few hours during experiments.

Since the alignment of the different electrodes in the ion source is not perfect (see sec. 3.6), the caesium focus voltage shifts the beam slightly when changed, resulting in areas of the sample and the sample holder being sputtered, that were not hit before. This behaviour increases the extracted ion current for a short duration after increasing the caesium focus, as can be seen in fig. 3.4.1. This changes at maximum current and beyond, where this effect is inverted and I_{FC2} slowly declines. After 6 min, the current seems to be stable after changing the caesium voltage.

The first maximum in current is reached at $U_{\text{CF}} = 4\text{ kV}$. For $U_{\text{CF}} = 4.4$ and 4.5 kV the $^{12}\text{C}^-$ current increases again for unknown reasons. When going down from $U_{\text{CF}} = 4.8\text{ kV}$ the voltage for the current maximum, which is lower by around 5 μA , decreased by 0.2 kV. This could be caused by the shifting position of the caesium beam spot on the sample as well.

3.4.3 Study of different sample holder material

With the ion source several sample holders (see fig. 3.2.3) made of aluminium, were delivered. However, the Ion Beam Centre at HZDR operates their sputter ion source by a different manufacturer, with copper holders.

Here it was tested, whether copper or aluminium perform better in the fields of rise time, the time until maximum current is reached, maximum extracted $^{12}\text{C}^-$ current and lifetime. In [Szü+19] one sample with a copper holder and one with an aluminium one were compared with each other. In both cases the ion source was cold beforehand and then operated at 5 kV cathode voltage until the burning-in phase was finished, after which U_{Cath} was increased to 6 kV and all other voltages adapted for maximum $^{12}\text{C}^-$ current.

For the aluminium, this happened after 1.5 h. The current rose to $\sim 80\mu\text{A}$ in 2 h and then

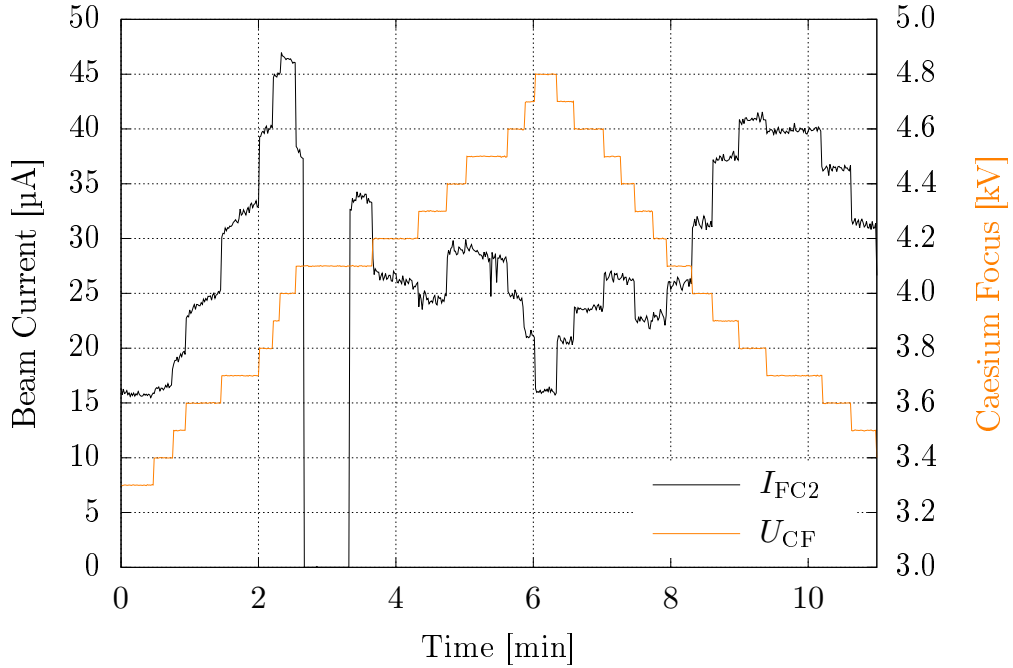


Figure 3.4.1: Dependency of the caesium focus voltage of the ion source (orange) on the ion beam current (black). The current of $^{12}\text{C}^-$ increases with the caesium focus voltage, reaches a maximum and then declines due to overfocusing. This measurement was performed at $U_{\text{Cath}} = 5 \text{ kV}$. At 3 min FC1 was inserted.

slowly declined. The copper one took 4.5 h to burn in, far longer than the aluminium one, and then continued to rise up to $110 \mu\text{A}$ in 8 h until the measurement was stopped.

Therefore, aluminium holders are better suited for experiments, since they provide the highest ion current far earlier, even though the peak is lower than for the copper ones. Additionally, other samples with aluminium holders performed better, reaching currents of $110 \mu\text{A}$, while other copper samples had lower burn-in and rise times, when the source was already active before the sample was switched.

3.5 Magnetic beam analysis

In the following, the beam extracted by the ion source was analysed by an electromagnet. The magnetic field forces the charged particles onto a circle, where the Lorentz force equals the radial force. From this relation, the B field necessary to guide an ion of mass m and energy E through the magnet is calculated as follows:

$$B = \frac{\sqrt{2mE}}{qr}, \quad (3.5.1)$$

with $r = 45.7 \text{ cm}$ being the bending radius of the magnet. Since all ions extracted have charge $q = -1e$ and with that the same energy after passing the acceleration potentials of the ion

source, this equation essentially only depends on the mass of the ions.

Unfortunately, at the point of the measurements, only the current through the magnet was logged automatically and not the magnetic field, which is measured by a Hall probe outside of the yoke of the magnet (see fig. 3.3.1). In order to calculate the ion mass for a given current through the magnet, first the relationship between the current through the magnet I_{Magnet} and the magnetic field at the Hall Probe B_{Hall} was determined. Afterwards, known isotopes were used to deduce the factor from the measured field at the Hall probe to the field influencing the ion beam.

3.5.1 Hysteresis of the electromagnet

To determine the hysteresis of the electromagnet, the relation between I_{Magnet} and B_{Hall} was investigated. The current was increased in 5 A steps from 0 A to a maximum of 120 A and back to 0 A. The corresponding magnetic field of the Hall probe was noted down by hand. As can be seen in fig. 3.5.1 the magnet shows no hysteresis with the points for ramping up and down aligning. A linear fit $B_{\text{lin}}(I_{\text{Magnet}})$ from 0 A to 75 A and a quadratic fit $B_{\text{quad}}(I_{\text{Magnet}})$ for higher current, where the iron yoke of the magnet is saturated, describe the data well.

3.5.2 Conversion from the magnet current to the ion mass

The hall probe could not be positioned directly between the yoke of the magnet and therefore only picks up a magnetic field B_{Hall} , that is proportional to the magnetic field B_{Beam} in the beamline, where $B_{\text{Beam}} = \alpha \cdot B_{\text{Hall}}$. This leads to a modified version of eq. 3.5.1:

$$m = \frac{(qrB_{\text{Beam}})^2}{2E} = \frac{(qr\alpha B_{\text{Hall}})^2}{2E}, \quad (3.5.2)$$

where α can then be determined experimentally from easily identifiable peaks.

Middleton investigated the mass analysis spectrum of a ^{12}C sample for a caesium sputter source [Mid77]. He observed a structure of peaks: $^{12}\text{C}^-$ with a relative intensity of ≈ 1.5 , $^{12}\text{C}_2^-$ with 1, $^{12}\text{C}_3^-$ with 0.08 and $^{12}\text{C}_4^-$ with 0.01. A comparison to the here observed peak ratios will be presented in the next subsection.

This structure could be identified in our spectrum as well, yielding the possibility to calculate α and the expected ion mass from I_{Magnet} , which is shown in fig. 3.5.2. From the first four carbon peaks $\alpha = 2.12$ was calculated. Therefore, only approximately half of the magnetic field is picked up at the current position of the Hall probe. With this information the peaks can be easily identified, because the ion masses can be calculated from the logfiles, which only contained I_{Magnet} .

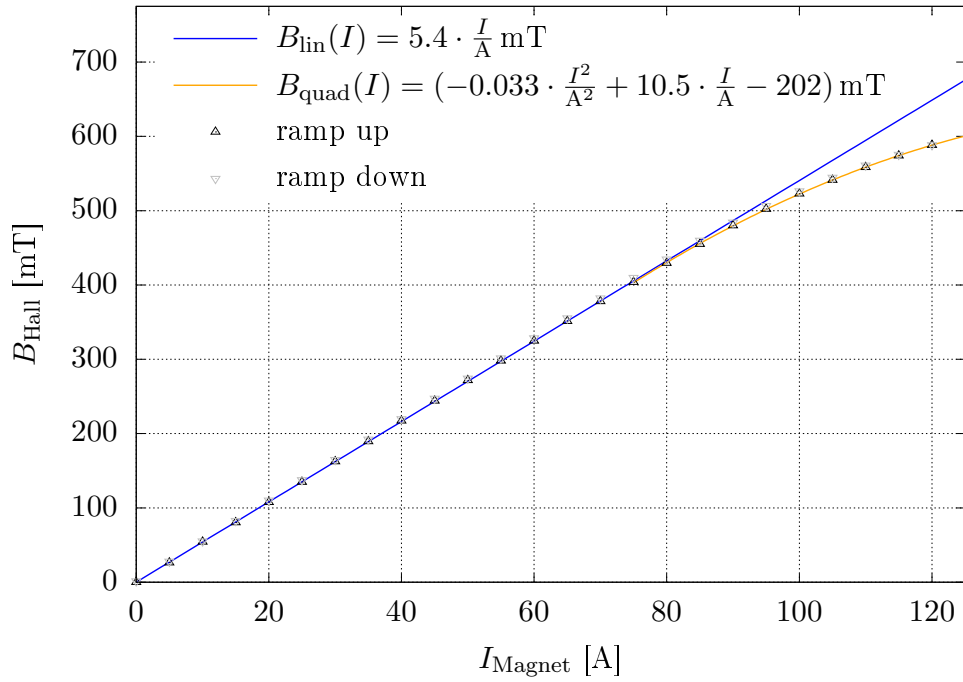


Figure 3.5.1: Hysteresis of the electromagnet at the low-energy beamline. There is only a small difference between ramping up and down of the magnet. Furthermore B_{Hall} depends linearly on I_{Magnet} until 75 A (blue fit), after this it can be described by quadratic function (orange fit).

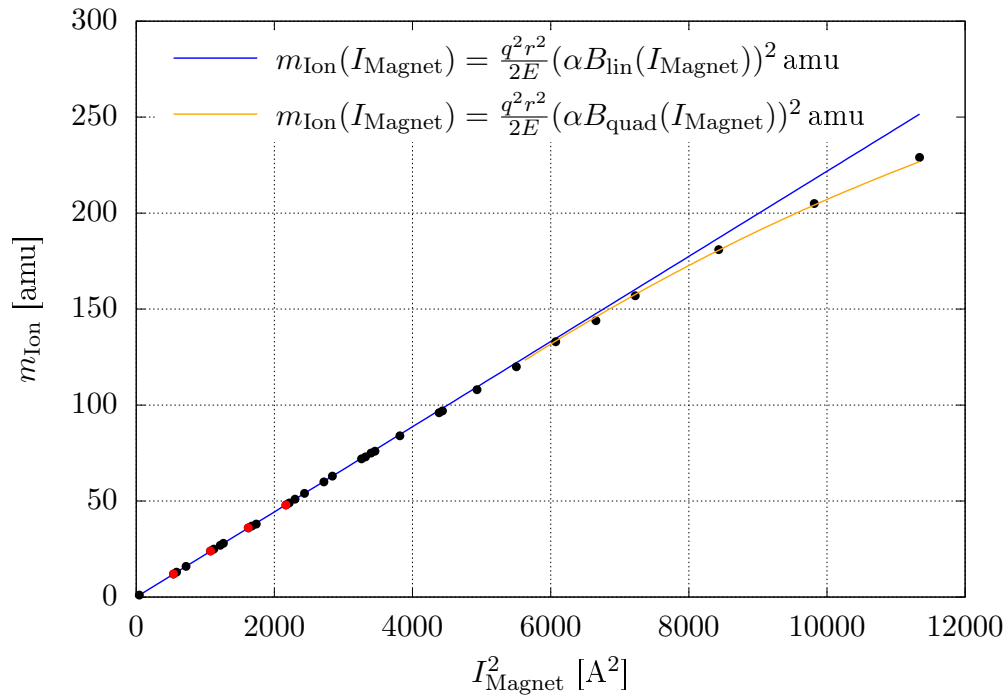


Figure 3.5.2: Relation between the mass of an ion and the current through the analysing magnet. The easily identifiable carbon peaks with mass 12, 24, 36 and 48 (red points) were used to fit the proportionality factor α between B_{Hall} and B_{Magnet} .

3.5.3 Beam analysis

The beam extracted by the ion source was analysed with the electromagnet for two different cathode holders. The operation parameters are listed in tab. 3.5.1.

Note, that the external source was in both cases set to the parameters, that extracted the highest current on FC1. Unfortunately, for the copper cathode, U_{Cath} could only be increased to 6 kV, because of the ionizer outages, as described in subsec. 3.4.1.

During the measurement the beam current on FC1 was measured at the beginning and the end of each scan. It decreased for the aluminium holder from 220 μA to 180 μA , while it increased from 93 μA to 123 μA for the copper holder.

In order to scan for different ions in the beam, the magnet current was increased in steps until there was a beam visible on the beam profile monitor behind the analysing magnet. This peak was then scanned in detail with smaller current steps. All the slits were extracted, sacrificing mass resolution for the ability to measure weak peaks as well. Since the electronics of the I_{FC2} had noise in the nA region, which might be caused by scattered ions, only peaks with a current of at least 10 nA are shown in fig. 3.5.3.

The identified peaks are listed in tab. 3.5.2. For aluminium all carbon peaks $^{12}\text{C}_n$ from $n = 1$ to 12 are visible, as well as the $^{133}\text{Cs}^{12}\text{C}_{2k}$ peaks for $k = 1$ to 5. For copper, due to the lower overall current provided by the sample, only $n = 1$ to 6 and $k = 2,3$ were observed. The most notable difference are ions consisting of the sample holder material. For copper, there are peaks at $m = 63, 65, 75, 87$ and 89 amu, the latter compounds of carbon and copper, which are not visible in the case of aluminium. On the other hand aluminium forms negative ions with itself and with carbon with the mass numbers 27, 51, 54, 63, 75 and 99. To verify the assignment of ions to the peak, compounds can be split in the stripper gas of the accelerator and the fractures analysed at the high-energy magnet. Due to time constraints, this was not done in the scope of this thesis.

For both holders, there are ions apparent, which do not derive from carbon, caesium and the sample holder material, namely hydrogen at $m = 1$ amu and a peak at $m = 16$ amu, that could be either methane or oxygen or both. However, no other oxygen containing peaks could be observed, so that methane seems the more plausible option.

Especially for high ion masses, the resolution for the ion masses deteriorates, so that, i.e. $^{133}\text{Cs}^-$ and C_{11}^- can not be distinguished anymore. This can be seen at $m = 72$ of the aluminium holder, where peaks of two ions with mass difference 1 overlap. A list of all reasonable ions is

Sample holder	U_{Bias} [kV]	U_{Extr} [kV]	U_{Cath} [kV]	U_{CF} [kV]	U_{El} [kV]	$I_{\text{FC1,max}}$ [μA]
Al	37.5	15	7.5	5	1.5	220
Cu	39	15	6	3	1.5	123

Table 3.5.1: Operating parameters for the ion source during the beam analysis of a copper and an aluminium sample holder.

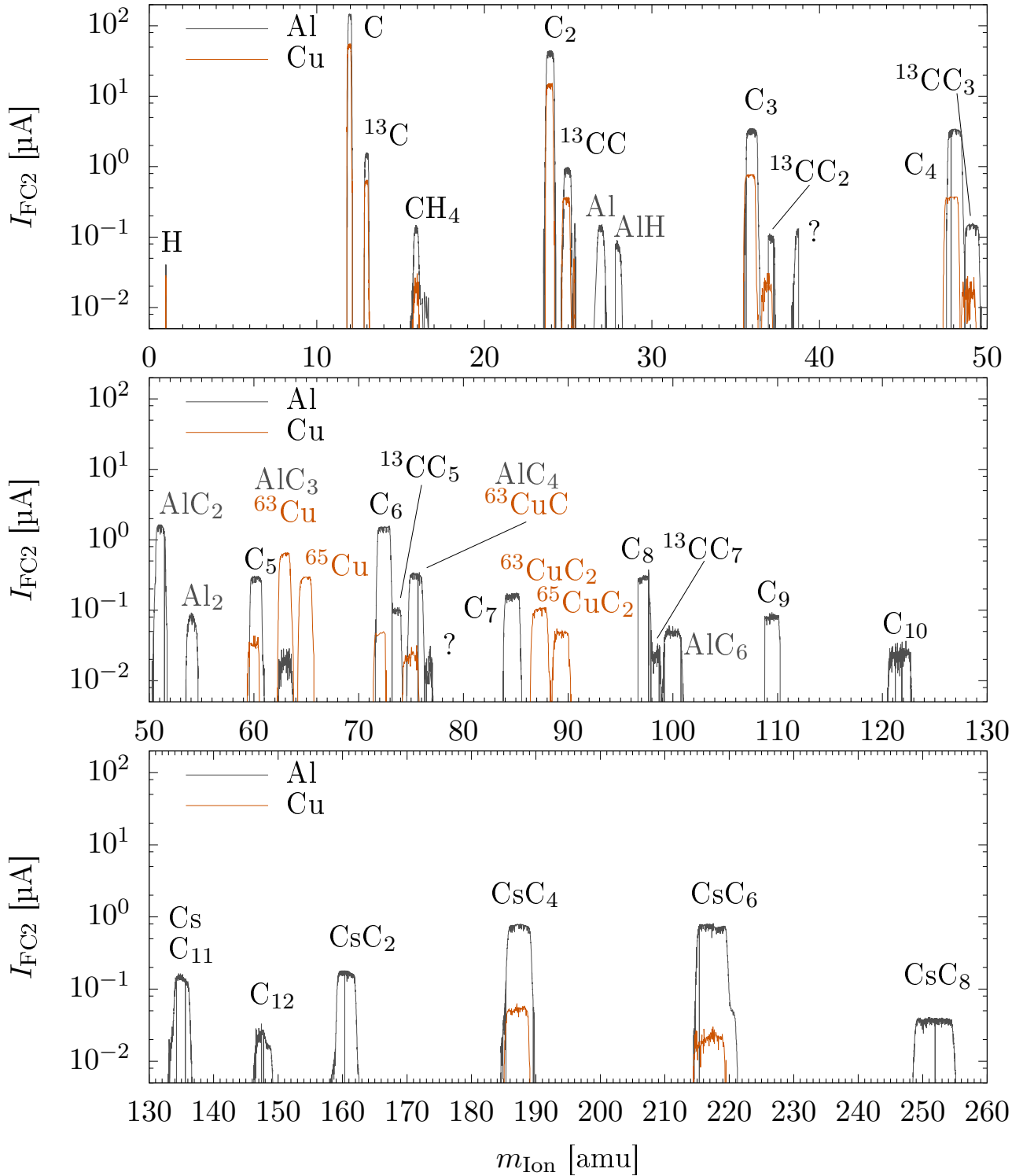


Figure 3.5.3: Analysis of the beam extracted by the ion source with an electromagnet for two different sample holder materials: aluminium (grey) and copper (orange). Most prominent ions for each peak are noted in the plot. Note, that the mass numbers of ^1H , ^{12}C , ^{27}Al and ^{133}Cs were omitted for clarity. A list of these and possible other ions can be found in tab. 3.5.2.

shown in tab. 3.5.2. Two ions extracted from the sample in the aluminium holder could not be identified: $m = 38$ and 76 amu. These could be carbohydrates as well, like $^{12}\text{C}_3\text{H}_2^-$ in the case of the former.

Middleton further observed a characteristic pattern of the intensity of the polyatomic carbon peaks, where the peaks with an odd number of carbon atoms are less intense than even numbered ones [Mid77]. This is true for the aluminium holder, but not for the copper one, as is shown in table 3.5.3. For the aluminium holder the pattern follows the one found by Middleton up until C_{11}^- , which is enhanced by $^{133}\text{Cs}^-$ and therefore higher in our case. For copper the intensity is declining with the number of carbon atoms in the molecule until the peaks could not longer be measured. This could be caused by the different cathode voltage used for this sample holder.

In order to rule out other ions in some of the peaks, the isotopic abundances were carefully evaluated. The ratio of the ion peaks with mass 13 amu to the one with mass 12 amu should follow the ratio of ^{13}C to ^{12}C and for the polyatomic carbon peaks $I(12n + 1)/I(12n) = nN(^{13}\text{C})/N(^{12}\text{C})$. This ratio is displayed in table 3.5.4. For the aluminium holder at $n = 1, 2$ and 4 the experiment follows the expectation. Since $n = 6$ and 8 are higher than the expected values, there could be another ion with the same mass as the peak containing ^{13}C . At $n = 3$ the ratio is lower, leading to the conclusion that the only ^{12}C peak might contain another ion. For copper, $n = 1$ is only slightly higher, while all the others are significantly higher compared to the expected result.

The same is possible for the copper isotopes, where the ^{65}Cu to ^{63}Cu ratio of the intensities is both 0.45 for the mono-atomic peaks and the CuC_2 compounds. This perfectly matches the ratio of the isotopic abundances $N(^{65}\text{Cu})/N(^{63}\text{Cu}) = 0.45$ [IAE20].

m_{Ion} [amu]	Ion candidates		m_{Ion} [amu]	Ion candidates	
	Al	Cu		Al	Cu
1	$^1\text{H}^-$		72	$^{12}\text{C}_6^-$	
12	$^{12}\text{C}^-$		73	$^{13}\text{C}^{12}\text{C}_5^-$	-
13	$^{13}\text{C}^-$		75	$^{27}\text{Al}^{12}\text{C}_4^-$	$^{63}\text{Cu}^{12}\text{C}^-$
16	$^{16}\text{O}^-$, $^{12}\text{CH}_4^-$		76	?	-
24	$^{12}\text{C}_2^-$		84	$^{12}\text{C}_7^-$	-
25	$^{13}\text{C}^{12}\text{C}^-$		87	-	$^{63}\text{Cu}^{12}\text{C}_2^-$
27	$^{27}\text{Al}^-$	-	89	-	$^{65}\text{Cu}^{12}\text{C}_2^-$
28	$^{27}\text{Al}^1\text{H}^-$	-	96	$^{12}\text{C}_8^-$	
36	$^{12}\text{C}_3^-$		97	$^{13}\text{C}^{12}\text{C}_7^-$	-
37	$^{13}\text{C}^{12}\text{C}_2^-$		99	$^{27}\text{Al}^{12}\text{C}_6^-$	-
38	?	-	108	$^{12}\text{C}_9^-$	-
48	$^{12}\text{C}_4^-$		120	$^{12}\text{C}_{10}^-$	-
49	$^{13}\text{C}^{12}\text{C}_3^-$		132,133	$^{133}\text{Cs}^-$, $^{12}\text{C}_{11}^-$	-
51	$^{27}\text{Al}^{12}\text{C}_2^-$	-	144	$^{12}\text{C}_{12}^-$	-
54	$^{27}\text{Al}_2^-$	-	157	$^{133}\text{Cs}^{12}\text{C}_2^-$	-
60	$^{12}\text{C}_5^-$		181	$^{133}\text{Cs}^{12}\text{C}_4^-$	
63	$^{27}\text{AlC}_3^-$	$^{63}\text{Cu}^-$	205	$^{133}\text{Cs}^{12}\text{C}_6^-$	
65	-	$^{65}\text{Cu}^-$	229	$^{133}\text{Cs}^{12}\text{C}_8^-$	-

Table 3.5.2: List of all possible ions found in the extracted beams of the two different holders.

	$^{12}\text{C}_2^-$	$^{12}\text{C}_3^-$	$^{12}\text{C}_4^-$	$^{12}\text{C}_5^-$	$^{12}\text{C}_6^-$	$^{12}\text{C}_7^-$	$^{12}\text{C}_8^-$	$^{12}\text{C}_9^-$	$^{12}\text{C}_{10}^-$	$^{12}\text{C}_{11}^-$	$^{12}\text{C}_{12}^-$
Middleton	100	8	10	1.1	3.6	0.6	1.2	0.3	0.2	0.07	0.07
Al	100	7.9	7.8	0.7	3.5	0.4	0.7	0.2	0.07	0.3	0.05
Cu	100	5.0	2.4	0.3	0.3	-	-	-	-	-	-

 Table 3.5.3: Intensity of the polyatomic carbon peaks normalised to $^{12}\text{C}_2^-$ as extracted by the copper and aluminium sample holder in comparison to those by Middleton [Mid77].

n	1	2	3	4	6	8
Expected [%]	1.10	2.20	3.30	4.40	6.60	8.80
Al [%]	1.10	2.23	2.90	4.41	7.33	10.00
Cu [%]	1.16	2.41	3.89	5.41	-	-

 Table 3.5.4: Ratio of the intensity of carbon peaks with mass $m + 1$ to m . The expected row is the result of the ratio of the isotopic abundances of ^{13}C to ^{12}C .

3.6 Realignment of the ion source

During operation, breakdowns of the high voltages on the plates of the ESA were observed. It is thought, that these might be caused by the halo of the beam hitting the plates. Inserting the slits at SLS1 in front of FC1, showed, that the beam is off-centre at this position. In principle this could be corrected with the two vertical steerers, the electrostatic analyser and the electromagnet. However, there are two reasons, why the realignment of the source would be beneficial. First, each focusing element has a slit system at the focus point behind it. With this, one can improve the focus by nearly closing the slits and optimizing the source parameters for maximum ion current on the following Faraday cup. This procedure only works, if the beam is centred at the slit system. Second, changing parameters of the source itself, like the caesium focus voltage, move a misaligned beam in spatial direction as well, so that even if the beam is shot nicely into the accelerator for one parameter set, this might not apply to another one. Since an off-centre beam resulted in breakdowns of the ESA and can lead to beam losses in the accelerator, it was deemed necessary to improve the alignment of the external ion source. For this purpose, several adjustment screws are located at the base of the ion source. Furthermore, there are two alignment kits by NEC available. One can be installed on the source itself, while the other is for the acceleration tube of the source containing the einzel lens and the extractor.

If the kit is placed on the source one can pass a cylinder through it, that fits through the inner parts of the ion source tightly into the top hole of the cathode wheel, where normally the sample in operation would be installed. If the cylinder gets stuck, adjustment screws on

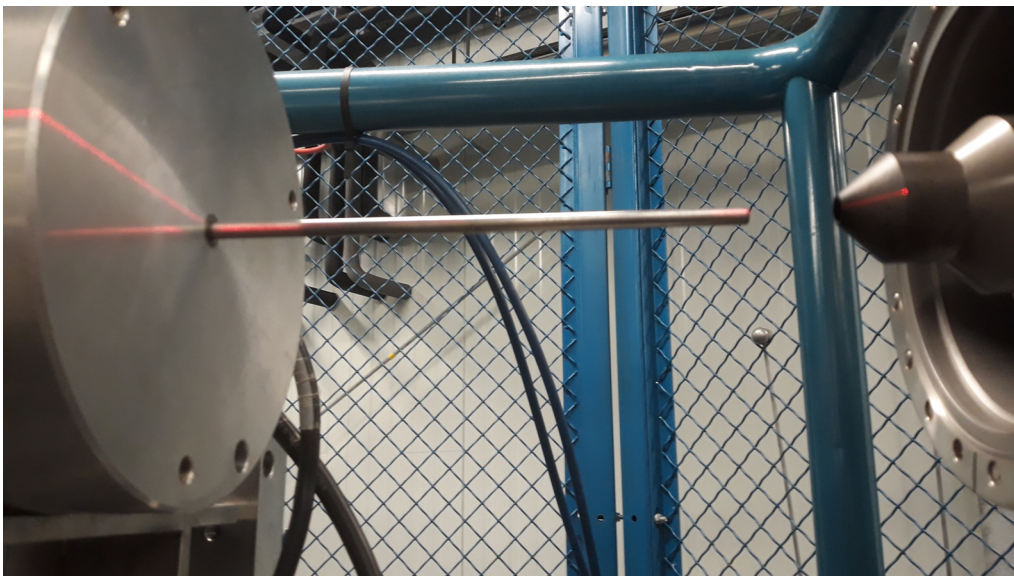


Figure 3.6.1: Vertical realignment of the ion source with the help of an alignment kit and a laser. The metal rod shown, was inserted without resistance through the ionizer and caesium focus into the cathode wheel. The laser is in the centre of the rod at the source, at the other end of the rod and at the extractor.

the ionizer, the caesium focus and the cathode wheel can be used, until the metal stick passes through without resistance. Additionally, the horizontal and vertical orientation of the source was checked in respect to the following beam line with lasers. This procedure is shown for the vertical alignment in fig. 3.6.1.

For the extractor, a similar kit was available. There a stick was inserted into the extractor from one side and three connected plastic cylinders into the einzel lens from the other side. During the process adjustment screws were used to improve the alignment.

Before and after realigning, the position of the beam was checked at the slit system SLS1 directly behind the MC-SNICS. For this, one slit was inserted until FC1 picked up no current and pulled out in 0.5 mm steps. For a Gaussian beam, this yields the integral of a Gaussian function. As can be seen in fig. 3.6.2 the position of the beam was improved a lot in y -direction, where it was too far below and is now satisfactory. In x -direction the beam position worsened and is 2.2 mm off to the left after the realignment, instead of 1.2 mm to the right. However, with the available equipment, it can not be aligned any more accurately, so that redoing the procedure might only worsen the situation. The transmission through the accelerator was satisfying in this setup, as will be described in detail in subsec. 4.3.6. Periodic breakdowns of the ESA voltages remain for some parameter sets of the external ion source, but it is unclear, what causes them.

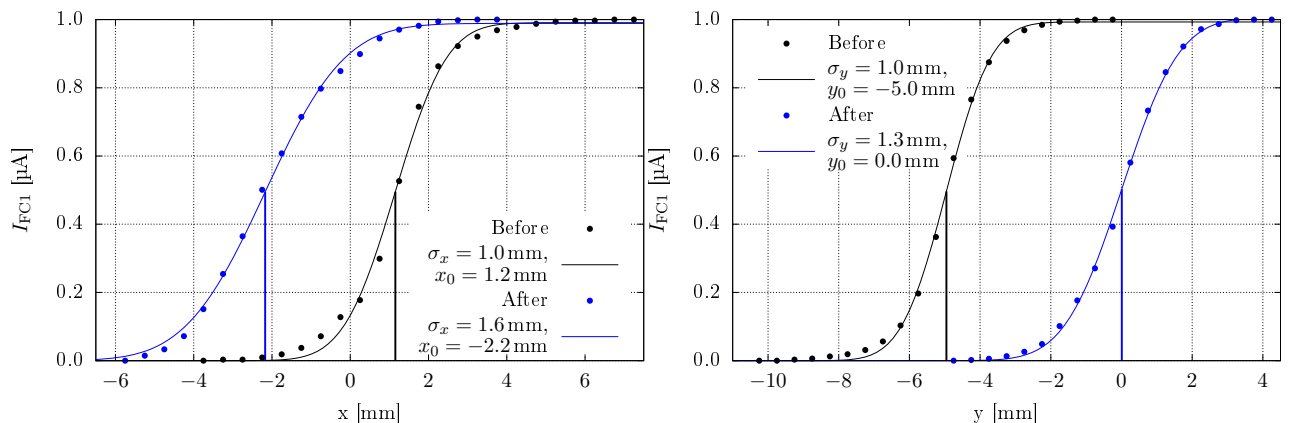


Figure 3.6.2: Measurement of the beam position before (black) and after (blue) the realignment with the slit system directly behind the ion source for x - (left) and y -direction (right). The centre of the beam is marked with a vertical line in each case. While the y -direction improved tremendously, the x -direction got shifted too far to the left.

4 Commissioning of the accelerator

The beam of $^{12}\text{C}^-$ provided by the ion source, needs to be accelerated to the energies necessary for nuclear astrophysics. For this, an electrostatic accelerator is used. Sec. 4.1 will report on the Felsenkeller accelerator, sec. 4.2 will follow the path of the beam out of the accelerator into the HE beamline. The influence of the stripper pressure inside the terminal will be discussed in detail in sec. 4.3.

4.1 The accelerator

The accelerator, that was installed in Felsenkeller, is a 15SDH-2 Pelletron by NEC. It is a tandem accelerator based on a Van-de-Graaff generator and consists of an 8.5 m long pressure vessel filled up to 6 bar with the insulation gas SF_6 to avoid discharges of the high voltage. This tank contains the acceleration column, that is interrupted by the terminal in the centre of the accelerator. The terminal hosts the internal ion source and the gas stripper. Two pellet chains connect the terminal with the high-energy end of the accelerator. They consist of steel pellets linked by nylon and are operated by an electric engine.

The high voltage is maintained by up- and down-charging. For this, the steel cylinders are positively charged by induction at the high-energy end and carry this charge to the terminal, where they deposit it at a sheave (see fig. 4.1.1). After the negative charge is induced, it is transported away from the terminal and deposited in another sheave at the end of the accelerator. This process creates a positive charge excess on the terminal, leading to a positive accelerating voltage. The higher the induction voltages, the more charge is transported to the terminal and the accelerating voltage increases. Stable voltage on the terminal is maintained by a closed-loop control system, which is described below.

The negative ion beam produced by the sputter ion source is shot into the low-energy column of the accelerator, where it is electrostatically accelerated by the positive voltage of the terminal. On the terminal, the beam passes through a stripper tube filled with nitrogen of a typical areal density of $0.5 \mu\text{g}/\text{cm}^2$, in which the ions lose electrons and get positively charged. Therefore they are now repelled by the positive terminal voltage. The total energy of a beam provided by the sputter ion source after acceleration is then given as follows:

$$E = E_{\text{Sputter}} + (1 + q) e \cdot V_{\text{Term}}, \quad (4.1.1)$$

with E_{Sputter} being the energy before injection, q the charge state of the ions after the stripping, e the elementary charge and V_{Term} the voltage of the terminal. The stripping process will be discussed in detail in sec. 4.3.

4.1.1 Accelerator conditioning

After long idle time or after disturbing the vacuum inside the accelerator columns, the accelerator needs to be brought back to the desired high voltage slowly, because gas and moisture were absorbed throughout the acceleration columns. When the high voltage is increased, these particles get relocated by the high electric field gradient. If too much gas is moved at once, it can cause discharges of the terminal voltage within the acceleration tube [Cha82].

Therefore, the terminal needs to be charged slowly, by increasing the induction voltages. For each induction voltage normally an equilibrium would be reached, where the charge brought to the terminal equals the current through the resistors of the two columns. However, during conditioning, this is not the case and the charging current is slightly higher than the added column currents. The excess current of a few μA is a manifestation of this gas redistribution to lower electric field gradients.

An occurring discharge is visible on the pressure gauges before and after the accelerator as well, where the pressure increases sharply by orders of magnitudes. Additionally, a current on FC3 and an x-ray burst, caused by back-accelerated electrons, on the dose rate measurement station near the sputter ion source can be observed sometimes.

During the operation of the facility, accelerator conditioning had to be done four times. The high voltage as a function of time for the first time is shown in fig. 4.1.2. One can see, that major discharges occurred at 2.4 MV, 3 MV, 3.1 MV and 3.2 MV until the terminal was brought up to the desired final high voltage of 3.2 MV. After this, the insulating gas was pumped from the accelerator for maintenance, while the beamline was under vacuum the whole time. In this case the accelerator could be brought back to high voltage without any discharges. This points to air getting absorbed in the beamline as the reason for the discharges as mentioned beforehand.

In the third conditioning effort the aim was a high voltage of 4.2 MV. However, starting at 3.5 MV frequent discharges occurred, even after the high voltage was kept on a certain value for several days. After six days of conditioning a maximum high voltage of 4.1 MV could be reached. Aitken *et al.* [AJP84] report, that damaged modules of the columns may be the cause of this. This can be checked at the Felsenkeller accelerator by using shorting rods to test the high voltage capability of individual modules, but was not done in this thesis due to time constraints and could be investigated in the future.

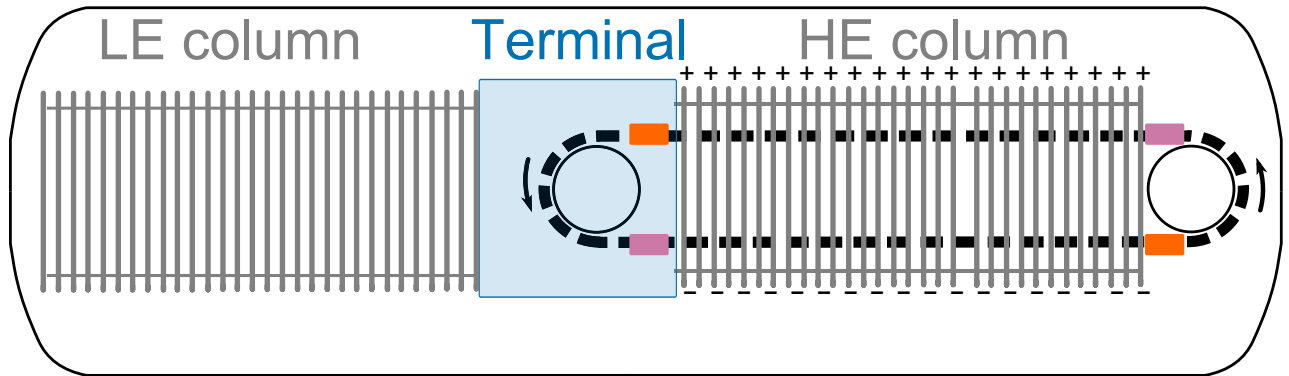


Figure 4.1.1: Schematics of the Pelletron tandem accelerator at Felsenkeller. In the upcharging process positive charge is induced by an induction electrode (purple) on a chain and transported to the high voltage terminal (blue), where it is deposited at sheaves. A suppression electrode (orange) prevents sparking. Afterwards, during downcharging, the chain is charged negatively and the charge transported to the end of the HE column, where the same process happens again. The second charging chain was omitted for clarity.

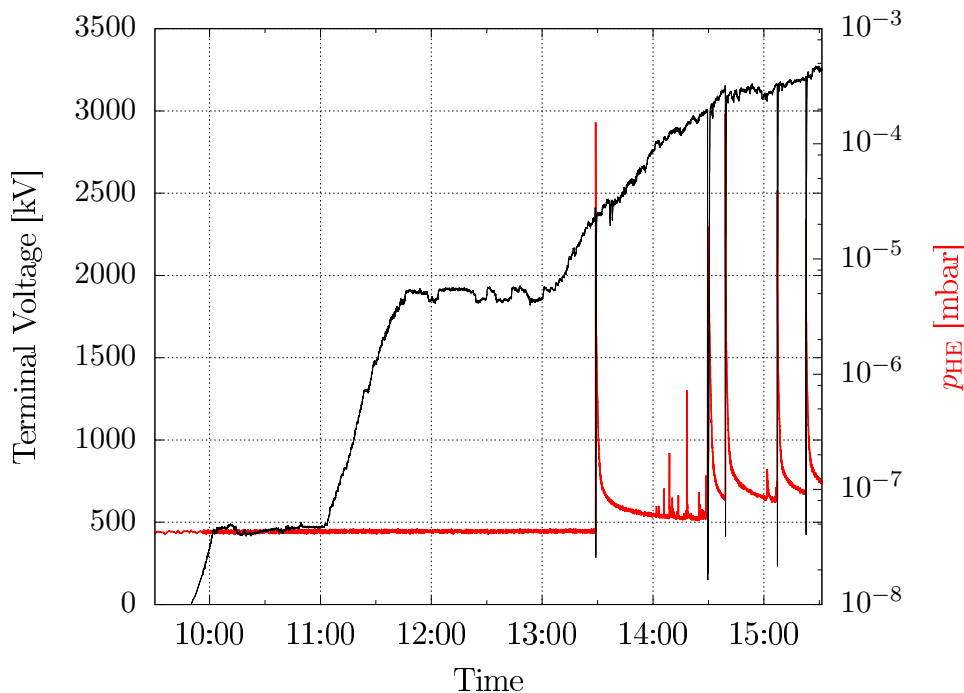


Figure 4.1.2: Conditioning of the accelerator. The terminal voltage is increased slowly with completely retracted corona probe. Five major discharges occurred starting at 2.4 MV, that are visible in the pressure of the high-energy beamline p_{HE} as a sharp increase as well. After the first discharge small pressure fluctuations happened, that were not the source of small discharges.

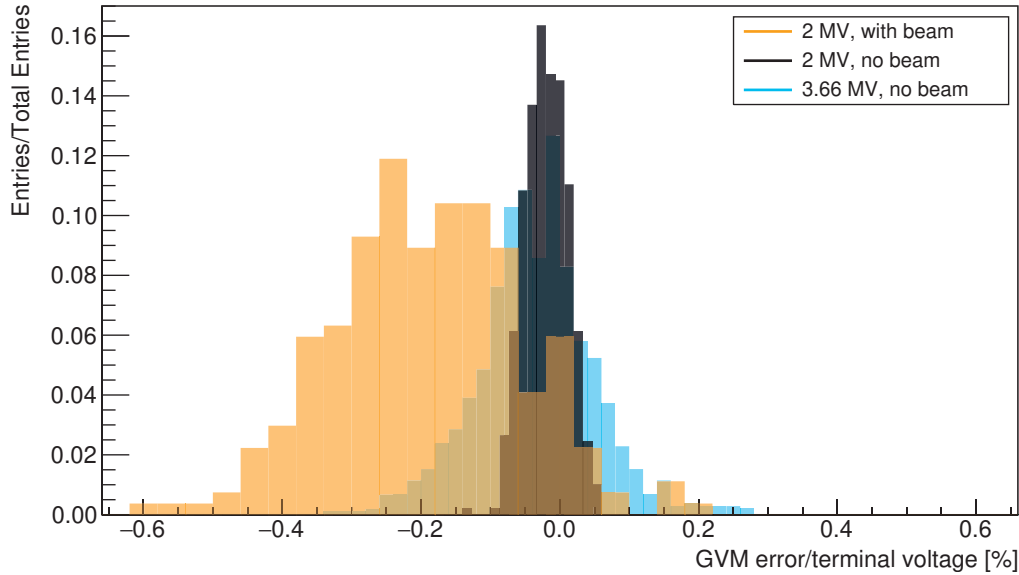


Figure 4.1.3: Histogram of the GVM error signal divided by the desired terminal voltage normalized to the number of entries for different voltages with and without beam. In all cases the accelerator was in GVM control mode. See text for more details.

4.1.2 Terminal voltage stability

From the terminal a constant current runs through the low-energy and high-energy beamline, where equal resistors connecting electrodes lead to a uniform gradient of the electric field.

Another source, that draws current, is the corona probe, that is the main part of the control system. It consists of needles on a probe, that cause constant corona discharges to the terminal electrode, because the insulating SF_6 becomes conductive as a result of the high electric field. Furthermore, the probe is connected to the anode of a triode, whose resistance is controlled by the grid voltage and therefore the current drawn by the probe. If the terminal voltage is too low, the grid voltage is lowered, increasing the resistance of the triode, resulting in less current drawn by the probe and an increased terminal voltage [Cor09a].

To ensure, that this process works for all desired terminal voltages, the probe can be moved, so that the electrical field at the needles remains constant. For higher voltages it needs to be pulled away from the terminal, while for lower voltages it can be inserted closer.

Charging current and loading currents need to be balanced for a stable high voltage. For that matter, there are two different control modes available: generating voltmeter (GVM) and slit control. In the first case the terminal voltage is determined by measuring the electric field. For this a rotor is placed above four plates on the tank wall. Two of the plates are grounded. When the rotor moves, it shields the plates from the electric field or exposes them to it. This results in an AC current, that is proportional to the electric field and thus the terminal voltage. The difference of this voltage to the desired one is then used to adjust the corona probe to draw more current, if the voltage is too high, or less vice versa.

The other option is the control via a slit system behind the high-energy magnet. This slit

control measures the current on two horizontal slits, that are inserted into the beam. The system then compares both slit currents by taking the difference of the left to the right one. If this difference is positive, the terminal voltage is too high and more corona probe current will be drawn.

During operation slit mode is more desirable, because it provides a fixed beam energy, that is determined by the magnetic field of the high-energy magnet. GVM mode can show drifts from the set voltage over time, caused by the varying performance of the ion source. Therefore, it is only used to set the terminal voltage, when no beam is extracted yet or to recover from sparks in the terminal.

These two control modes serve as one part of the control loop system, that is responsible for low-frequency changes of the terminal voltage. In order to measure high-frequency terminal ripple, which can be caused by differently charged pellets, capacitor pick-off plates (CPO) are installed at the tank wall close to the terminal. A CPO consists of a plate, that serves as capacitive voltage divider between terminal and tank. The impact of the tank vibration on the signal is minimized by the installation of two CPOs at the top and the bottom of the tank wall. The signals of these two are added up, adjusted in gain, filtered and then combined with the GVM or slit signal [Cor09b].

This control system leads to oscillations around the desired set high voltage and to deviations in the beam energy, especially for high charge states. In order to investigate this problem, the GVM error signal, that is the difference of the voltage measured by the GVM to the desired voltage, was examined. It was logged for two different voltages without beam running through, and at the lower voltage, but this time with $40\ \mu\text{A}$ of $^{12}\text{C}^-$ shot into the accelerator. The result is shown in fig. 4.1.3. For the lower voltage of 2 MV without beam the terminal is more stable. For a higher voltage the relative energy deviation increases, which results in even higher absolute voltage differences.

The worst scenario for the voltage stability is, when beam is being transmitted through the accelerator. Here the width of the distribution is the largest. This could be caused by parts of the beam hitting the terminal and disturbing the control system. The mean is shifted to the left, which hints at the fact, that the corona probe position and the induction voltage on the chain were not optimized carefully enough, potentially increasing the terminal ripple. Furthermore, the experiment was conducted at the beginning of the accelerator commissioning, while the other two took place later on, when already more experience with the machine had been obtained.

For the best case, the σ_{rel} of the Gaussian distribution amounts to 0.03%, which are 0.58 kV. This is comparable to the measurements by Lobanov *et al.* [Lob+12], where they achieved a σ_{abs} of 1.65 kV at 13.5 MV terminal voltage, which would be a σ_{rel} of 0.012%. The data sheet by NEC gives $< 1\ \text{kV}$ at 5 MV [Cor98], which is better by 0.01% than the best value reached here.

Terminal instability leads to a drift of the beam in x -direction for several millimetres after the high-energy magnet and large parts of the beam will be absorbed by a collimator in front of the target. Additionally, it is one of the bottle necks for high ion current. If high current is shot into the accelerator, the terminal voltage will oscillate with higher amplitudes. This results in a higher energy spread of the beam, that is translated into beam position deviations in x -direction after the high-energy magnet. As a result, these deviations will lead to beam losses at the high-energy slits or the collimator in front of the target. Ultimately, higher injected current leads to increased stress on the terminal, for a small increase in the mean target current, if any. A recalibration of the terminal potential stabiliser is discussed in sec. 5.3.

4.2 The high-energy beamline

In contrast to the low-energy part of the beamline, which was unchanged, the beamline at the high-energy end of the accelerator had to be adjusted from the setup in York to fit into the tunnels of Felsenkeller. For this, it was extended by a 1.65 m long drift tube. The analysing magnet was followed by an analysis beamline part in York, that hosted movable Faraday cups for atomic mass spectroscopy purposes. This part was omitted in the Felsenkeller setup. Instead the slit system, used for the control of the terminal voltage (see previous section), was installed there, followed by a magnetic quadrupole (MQ) and then the end part of the original York beamline. The whole setup is shown in fig. 4.2.1.

After first tests with beam running through the beamline, it became apparent, that the setup was not optimal. The adaptations from the original York setup changed the ion optics in a way, that made transmission of the beam much more difficult. The slit system, that serves as the accelerator control, was not positioned at the focus point, causing the beam waist there to be larger and the control more inaccurate. Additionally, the magnetic quadrupole was located close to the focus point, where it had only a negligible focusing effect on the beam. In order to remedy these two problems, the slit system was moved to a position ≈ 1.7 m after the magnet and the magnetic quadrupole, which was 0.6 m behind the magnet, to a distance of 3.1 m. As a result the target chamber had to be moved 1.5 m back from the high-energy magnet as well. For beam diagnosis purposes, two Faraday cups were installed in the high-energy beamline: FC3 shortly after the exit of the accelerator and FC4 behind the analysing magnet. Furthermore, several tools are hosted, where the beam position can be measured, namely slit systems and beam profile monitors (BPM) of type BPM80 by NEC. The first were already mentioned in sec. 3.6, while the latter consist of a thin rotating wire shaped in such a way, that during one revolution, first the horizontal and then the vertical plane of the beam is scanned. When this wire is hit by the beam, secondary electrons are produced, which are then collected and amplified [KAM94]. The amplifier outputs a voltage, that is proportional to the beam current and then read out by the digital oscilloscope PicoScope 2000 Series. The time information can

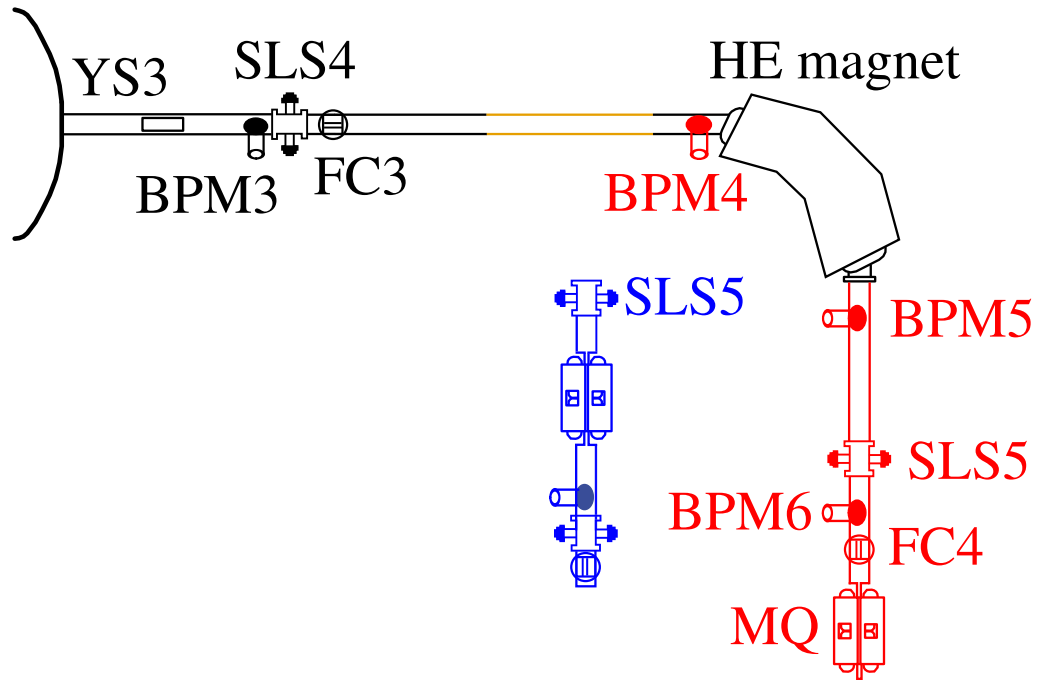


Figure 4.2.1: Schematics of the high-energy beamline. Blue elements show the arrangement before it was changed, the red ones the beamline afterwards. Before the HE magnet the beamline was not changed compared to the York design apart from inserting the 1.65 m drift tube (shown in orange). The turbo pumps and gate valves are left out in the picture.

be converted to spatial coordinates by using fiducial peaks, which are produced by magnets the wire passes and are read out in another channel of the digital oscilloscope. A tool, which was written by the students Hans-Martin Bartram (HZDR) and Tim Pokart (HZDR) under my supervision, converts the time information to spatial coordinates and displays the smoothed beam profiles in these in real-time. A calibration of the signal to the transmitted beam current was attempted, but unfortunately, it was non-linear and depending on the position and the energy of the beam. With this, only an online monitoring of the beam shape and position is possible, but not of the beam current.

While the slit systems have to be inserted into the beam manually and block the beam completely, the BPMs only absorb a small portion of the beam current and record data automatically. The correct derivation of the beam position by the BPMs was verified by using the steering possibilities on the beamline. Changes in the y -steerer or the electromagnet only affected their respective coordinate, while the position in the other dimension remained unchanged.

As can be seen in fig. 4.2.1, the high-energy beamline initially hosted two BPMs, while later on two additional BPMs, one up and one downstream of the electromagnet, were installed.

4.2.1 Vertical beam alignment

During the first tests, conducted before the alignment of the external ion source (see sec. 3.6), the beam was not centred in y -direction according to the BPM images. One option to remedy this is a vertical electrostatic steerer close to the exit of the accelerator. Increasing the voltage of this steerer led to an improvement of the position until the beam would not move any more, but decrease in intensity (see fig. 4.2.2), which pointed towards some obstacle in the path of the beam. This could in part be fixed with the quadrupole, since focusing elements also steer the beam, should it be off-centre. However, this resulted in a defocus of the beam, high losses and insufficient current on the target.

A possible explanation for this is, that the beam hits parts of the vacuum chambers, which would cause the incident spot to heat up by the deposited energy. Indeed, an area with increased temperature of a few K could be identified in the centre of the high energy magnet by looking through openings on the backside of the magnet with a thermal camera. It turned out, that the magnet was misaligned. This was fixed by turning the alignment screws while running beam through the magnet until the beam position on the following BPM was perfect. This, and the realignment of the external source (see sec. 3.6), led to a nearly perfect alignment of the beam in y -direction (see fig. 4.2.3).

4.2.2 Horizontal beam alignment

The x -direction shows a similar problem. Here the beam is already off-centre at the exit of the accelerator, which might be caused by misalignment of either the electrical quadrupole at the end of the accelerator or one of the two columns in the tank. Since the beam consists of ions of different charge states and, in tandem mode, different E/q , the quadrupole at the exit of the accelerator not only focuses the beam, but also steers it differently for each individual charge state. This is indicated by several overlapping peaks on the BPMs (see fig. 4.2.4).

The only steering option in horizontal direction is the analysing magnet, which is not sufficient to force the beam into the centre again. Since it already exits the tank off-centre by 1 mm to the left and with an angle of 0.06° for one parameter set, two steering positions would be necessary. It is only possible to guide the beam onto the target with an angle, so that it is centred at the collimator shortly in front of the target and hits the target itself slightly off-centre. This can be seen in fig. 4.2.4, where the current on target was maximized for a $^{12}\text{C}^{3+}$ beam.

However, there are downsides to this beam alignment, which are tied to controlling the accelerator voltage with the high-energy slit system. Since the beam is also off-centre at these slits, they need to be adjusted accordingly. As already mentioned before, the quadrupole at the end of the accelerator will shift the beam with varying voltage, therefore, the slit positions need to be adapted after changes of the quadrupole. In addition to that, readjustment of the slits

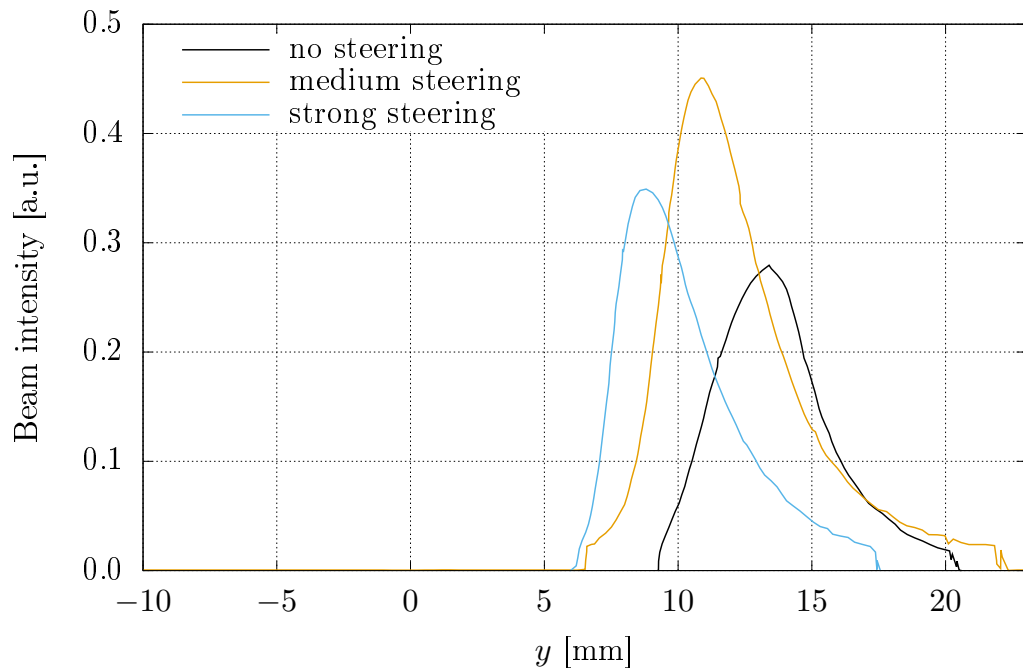


Figure 4.2.2: Vertical position of the beam on BPM5 before adjusting the height of the HE magnet. The beam is far too high without using the vertical steerer (black line), with medium steering voltage (orange line) the intensity and position improves until it only shifts negligible and beam intensity decreases again, when the beam is steered into the beamline at high steering voltages (blue line).

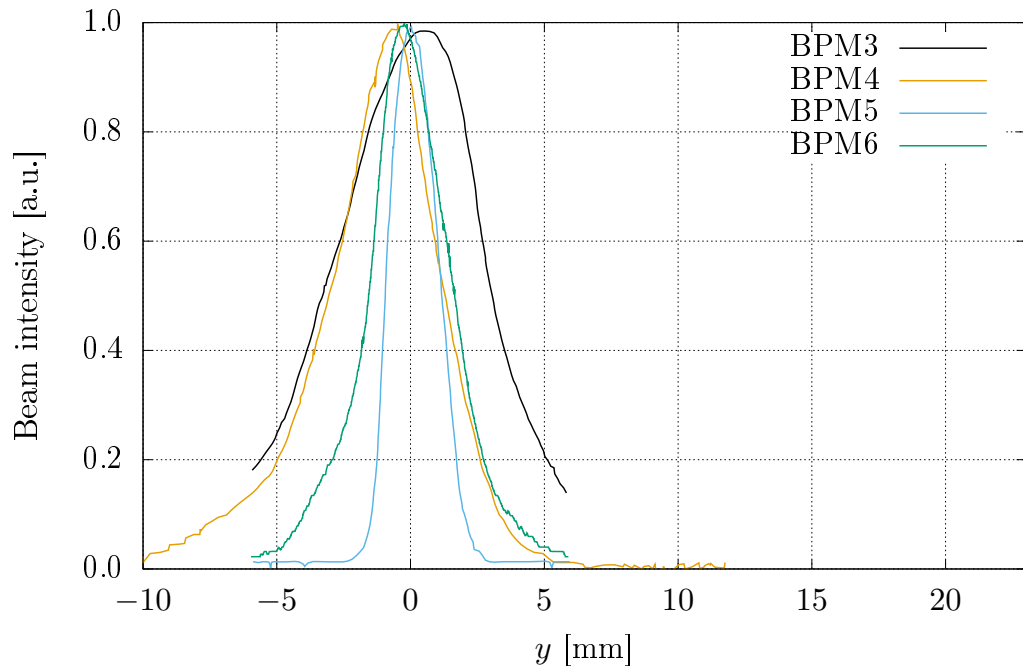


Figure 4.2.3: Vertical position of the beam on the BPMs of the HE beamline. On all positions the beam deviates only by under 2 mm from the centre.

is necessary after switching to another charge state of the beam due to the different focusing strength of the quadrupole and when switching between the internal and external ion sources. In principle one could use the GVM mode, which is sensitive to the beam current shot into the accelerator. So, as the ion source provides less and less current over time, the stabilisation system was not able to hold a constant terminal voltage in GVM mode and the terminal voltage increased by a few kV. This is especially a problem for unobserved operation of the accelerator, where the slit mode is preferred, since it ensures constant beam energy.

Another disadvantage is, that the suboptimal beam alignment leads to the beam hitting the copper tube in front of the target even though it is shielded by the collimator. This tube serves as a cold trap and will gas out, should the beam heat it up.

There are several options to address this alignment issue. The first would be to try to adjust the beamline inside the accelerator and with it the quadrupole, which is also the most time-consuming option.

Another possibility would be to install a remotely controlled step motor to insert and extract the high-energy slits to the appropriate position for the current setup, instead of having to adjust it manually. In addition, the collimator would need to have a smaller opening hole to protect the copper tube behind it, leading to higher current loss.

A third way could be to install additional horizontal steerers in front of the high-energy magnet. This was tested after the experiment, described in chapter 5 took place, by installing a magnetic x -steerer 1.74 m behind the accelerator. The result is shown in fig. 4.2.5. With this the charge states line up again and the beam is centred on the BPMs after the HE-magnet.

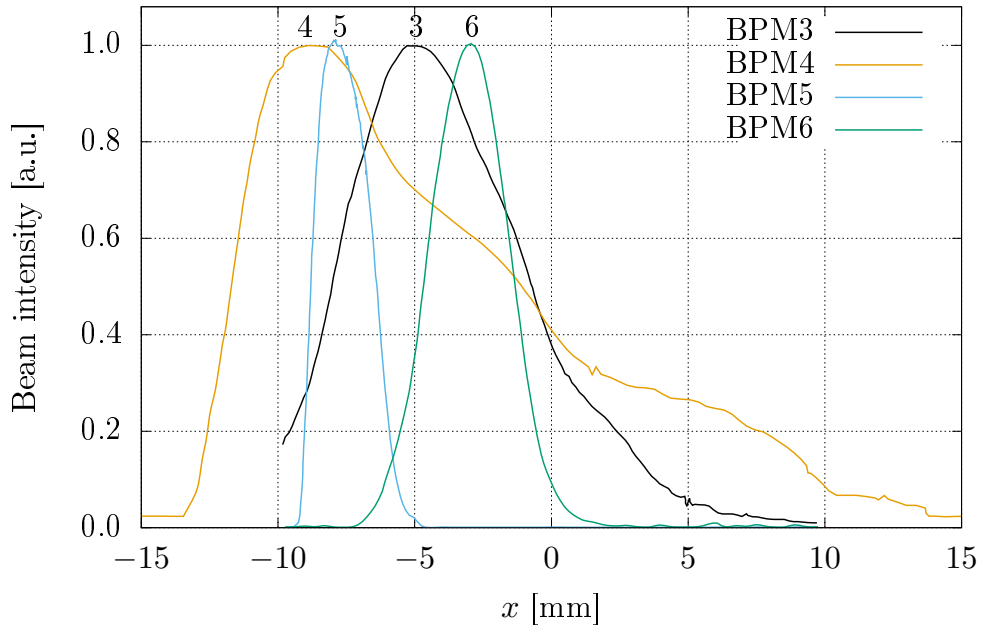


Figure 4.2.4: Horizontal beam alignment as measured by the four BPMs. Before the analysing magnet (BPM3 and 4) four overlapping peaks are visible, corresponding to the positive charge states 1+ to 4+. With the analysing magnet the 3+ state is selected and bent in a way, that current on the target is maximized, leading to a deviation of the beam to the left of about 7 mm at BPM5.

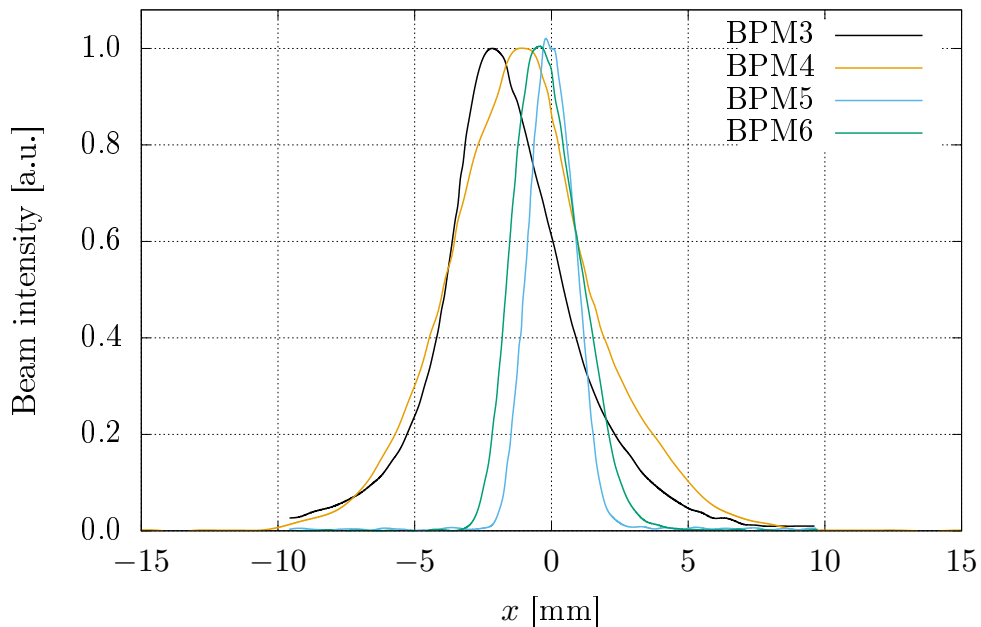


Figure 4.2.5: Horizontal beam alignment as measured by the four BPMs after installing an additional magnetic x -steerer behind FC3. With the analysing magnet the 2+ state is selected and could be centred on BPM5 and 6.

4.3 Stripper gas pressure

If the external ion source is used, the accelerator is operated in tandem mode. This means, that negative ions are shot into the accelerator and accelerated a second time after some electrons were stripped off in the gas inside the stripper tube on the terminal of the accelerator. The stripper medium, its areal density and the energy of the beam determine the charge state distribution of the ion beam at the end of the accelerator.

4.3.1 Fundamental interactions in the stripper

There are two processes, which determine the charge state of an ion after passing through the stripper medium: capturing an electron with the cross section σ_c or losing an electron with σ_l . Unfortunately, these cross sections can not be calculated analytically. First approximations following a classical approach were derived by Bohr in the 1940s and 50s for ions in a ground state with high Z and the exchange of only one electron per interaction [Bet72]:

$$\sigma_l \sim 4\pi a_0^2 Z^{1/3} Z_T^2 (v_T/v)^3 \quad \text{and} \quad \sigma_c \sim 4\pi a_0^2 Z^{1/3} Z_T^5 (v_T/v)^6, \quad (4.3.1)$$

with a_0 the Bohr radius, Z the atomic number of the ion, Z_T the atomic number of the target atoms and (v_T/v) the velocity of the target electron divided by the velocity of the ion.

However, experiments showed, that the exchange of more than one electron is not negligible and that excited electrons play a major role for heavy ions in dense strippers [Bet72]. Fig. 4.3.1 shows a comparison between these theoretical calculations and experiments. Electron capture is more likely for higher positive charge states and lower ion energy. Electron loss has a higher probability for negative charge state or neutral ions and remains nearly constant with the ion energy. The theoretical estimate differs substantially in the low-energy region for electron loss at high positive charge states, because the model by Bohr and Lindhard, that was used in the calculations, does not include shell effects. Furthermore, the exchange of two electrons is only one order of magnitude smaller compared to one electron exchanges [Nik+94].

Today, there are two options to calculate these interactions, either codes, that use more sophisticated models, like ERCS08 [Hor09] and ETACHA [Lam+15], or by solving the differential equations by using tabulated experimental data [Sut+18].

The charge state distribution at the exit of the accelerator can be approximated by a Gaussian distribution with the mean ion charge \bar{q} , the width σ_q and the skewness s_q , which indicates the asymmetry of the distribution. These parameters are dependent on the areal density of the stripper and the ion energy.

For low areal densities few interactions will take place. Therefore, the simple negatively charged ions will only be able to reach low positive charge states and a part of them will be neutral. With increasing density the distribution will shift to higher \bar{q} , until electron loss and capture

are balanced, the equilibrium density.

Two types of strippers are realised in accelerators: gaseous and solid ones. The first have the advantage of being able to control the pressure inside the stripper tube by a valve and therefore the areal density, which then fluctuates slightly. Solid stripper foils have a constant areal density, but will be destroyed after some time. In this case, the accelerator has to be opened and the foil exchanged.

In principle, one would expect, that both types of stripper yield similar results for equal areal densities, though this is not the case. For foil strippers higher \bar{q} are observed than for gas strippers. This is due to a density effect, that has two possible explanations: The time between interactions in foil strippers is low, so that excited electrons of the ions will not de-excite before the next interaction and are more likely to be lost, which leads to higher positive charge states. The second possibility is, that gas and foil stripper yield the same charge distribution, but for the solid more electrons are in an excited state. These then de-excite after the stripper by sending out Auger electrons. Experimental data favours the first explanation [Sch10]. In Felsenkeller only a gas stripper is installed, so this effect should be negligible for the present case.

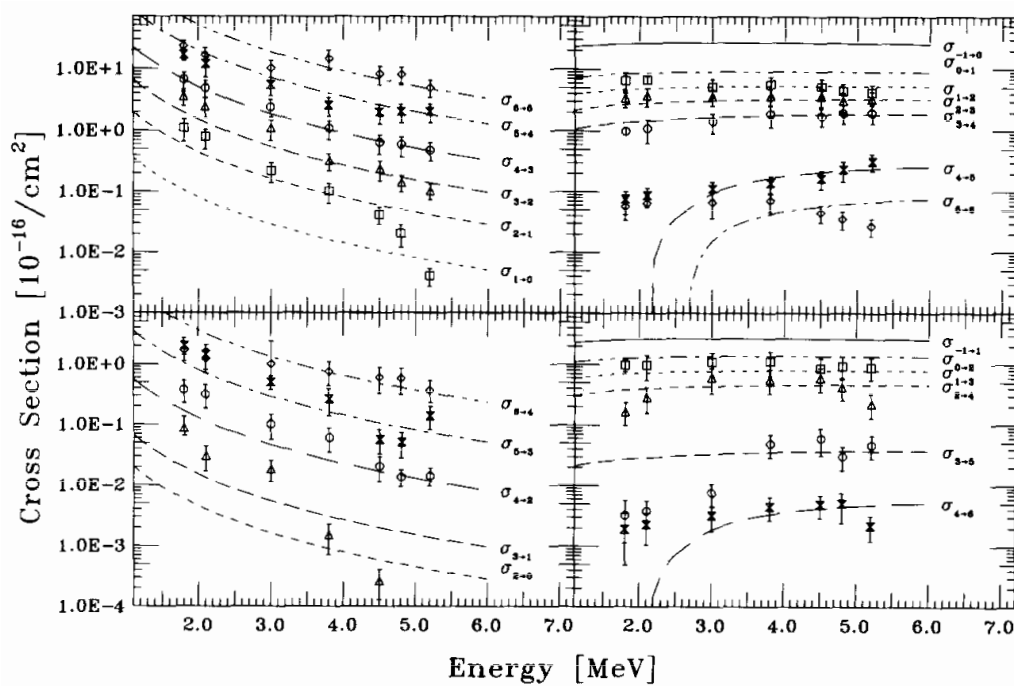


Figure 4.3.1: Cross sections for electron capture (left) and loss of electrons (right) for one (top) and two (bottom) electrons. The lines are the scaled model distributions. Taken from [Nik+94].

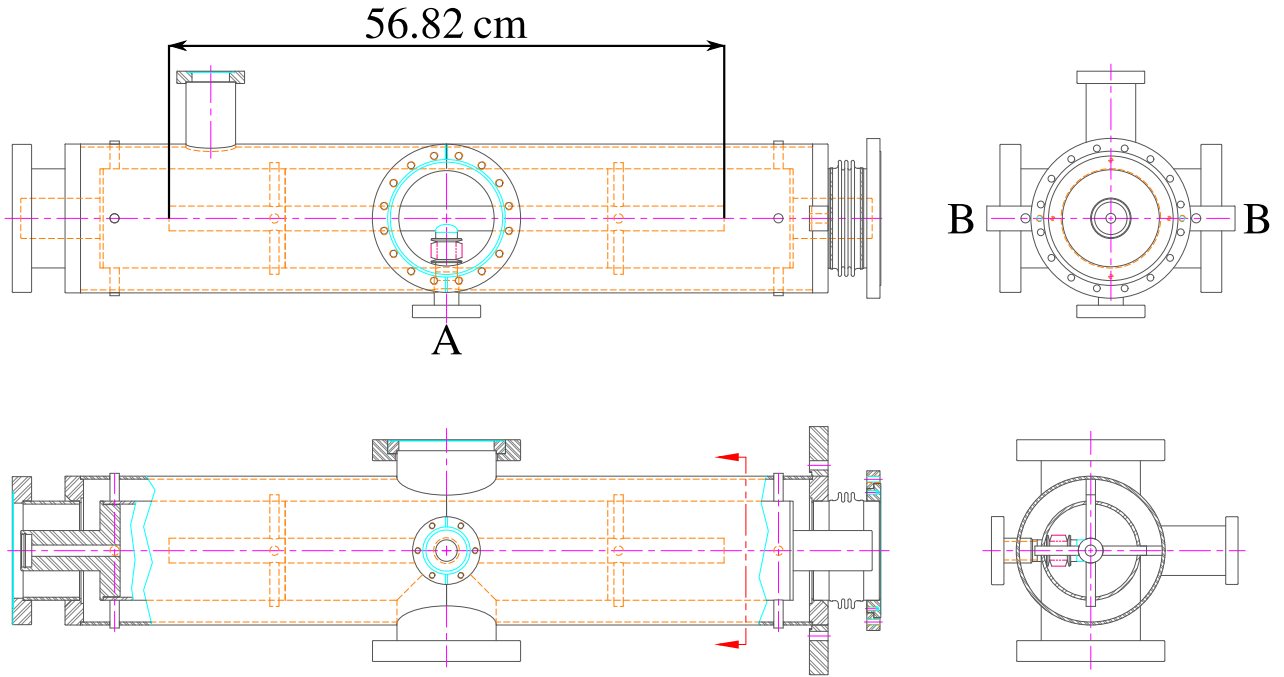


Figure 4.3.2: Technical drawing of the stripper tube installed at the terminal of the accelerator. The tube itself is 56.82 cm long. At A the valve for the stripper gas is located, while B denotes the position of the two turbo pumps, where one is connected to the inner and one to the outer tube.

4.3.2 Stripper setup at Felsenkeller

The terminal of the accelerator at Felsenkeller was remodelled to host the internal ion source. For that matter, the foil stripper, that was used in York, was removed. The gas stripper tube was exchanged by a shortened one of 56.82 cm length and 2.54 cm diameter, that is shown in fig. 4.3.2. It is fed with nitrogen by a controllable valve in the centre of the tube and encased by a second tube. Two turbo pumps, one connected to the inner, the other to the outer tube, recirculate the nitrogen to the valve. These pumps and a small opening of the stripper tube to the low-energy column ensure, that the vacuum of the beamline is not disturbed. The opening to the high-energy side is larger, because the beam is widened after the scattering processes in the stripper gas.

The areal density of the nitrogen gas can be calculated as follows:

$$x = \frac{N_A m_{N_2} L p}{k_B T}, \quad (4.3.2)$$

with the Avogadro constant N_A , the molecule mass of nitrogen m_{N_2} , the length of the stripper L , the Boltzmann constant k_B and the gas temperature T .

Unfortunately, the gas temperature could not be measured directly inside the stripper and could be subjected to heating by the beam. This beam heating effect was measured in [LUN+14] with the resonance scan method and far higher densities and beam currents. For a

proton beam in nitrogen, the difference in density could be calculated as follows:

$$\frac{n}{n_0} = 1 - \alpha \frac{dW}{dx} \left[\frac{\text{mW}}{\text{cm}} \right] = 1 - \alpha \frac{dE}{dnx} \frac{n}{L} I, \quad (4.3.3)$$

with n being the target density, n_0 the target density without beam at temperature T , the beam heating parameter α , $\frac{dE}{dnx}$ the energy loss by carbon in nitrogen and I the beam current. To gain an upper limit on the magnitude of this effect, a 50 μA carbon beam of 4 MeV was assumed. $\frac{dE}{dnx}$ was taken from SRIM [ZZB10]. α , with the value of $0.5 \cdot 10^{-3}$ for protons in nitrogen [LUN+14], was assumed to be $1 \cdot 10^{-2}$. With this conservative approach the relative beam heating effect is in the order of 10^{-12} and negligible compared to the density fluctuations caused by the gas recirculating process during the measurements.

4.3.3 Experimental method

In order to empirically determine the influence of the stripper pressure on the charge state distribution and the transmission, several combinations of terminal voltage and stripper pressure were measured. For this, a $^{12}\text{C}^-$ beam of nearly constant current of below 10 μA was shot into the accelerator. To avoid beam losses caused by a wide beam, the beam was restricted by slits in front of FC2 to a width of 2 mm.

After that, for one given terminal voltage and stripper pressure, the current on FC3 was measured. Meanwhile the high-energy magnet was tuned to the desired charge state. After retracting FC3 from the beamline, the beam was focused on FC4 and, if necessary, the quadrupole, the magnet and the y -steerer adapted to maximize current on FC4. All slits on the HE side were retracted completely and the BPMs turned off for the current measurements to minimize unwanted beam losses. After two minutes on FC4, FC3 was inserted again and the magnet current set to the next charge state. This procedure was done for the first four charge states of ^{12}C , since the current of $^{12}\text{C}^{5+}$ was in all cases too low to be measured with the current setup. In some cases, especially for low beam current on FC4, it proved challenging to perfectly maximize the beam transmission, so that in these cases the measured charge state distribution might deviate due to beam losses.

For a given target thickness, the beam current on FC3 varied by less than 5%. Only for the lowest beam energy of 1.14 MeV and low target thicknesses deviations on FC3 were higher with under 10%. This might be caused by beam losses in the accelerator, because the terminal voltage is too low to ensure optimal focusing through the acceleration columns.

For each of a total of five terminal voltages six stripper pressures were set. The lowest two pressures correspond to the maximum current of $^{12}\text{C}^+$ and $^{12}\text{C}^{2+}$ on FC4, respectively. The maxima of $^{12}\text{C}^{3+}$ and $^{12}\text{C}^{4+}$ are reached in the equilibrium, so that four other pressures were used to examine this region of pressure. These measurements were taken for the Bachelor's thesis of Tommy Meier [Mei20] under my supervision.

During the measurements, the beam current shot into the accelerator varied. Therefore the charge fraction F_q at FC4 was taken to compare different measurements, which is defined as follows:

$$F_q = \frac{I_{p,q}}{\sum_q I_{p,q}}, \quad (4.3.4)$$

with $I_{p,q}$ the particle current of charge state q .

Since beam losses in the HE beamline were observed (see subsec. 4.3.6), the charge state distribution at FC4 might differ, if the relative loss of beam is dependent on the charge state. Unfortunately, this is likely because of the horizontal steering effect of the quadrupole at the end of the accelerator. Due to this, higher charge states will be further off-centre at the entrance of the magnet, where a portion of the beam could be lost. Therefore, the results are to be understood as the charge state distributions at FC4 with the current setup. At FC3, directly behind the accelerator, the distribution might be different due to beam losses in the HE beamline.

4.3.4 Charge state distribution for different stripper pressures

As previously mentioned, for low stripper pressures low charge states will be populated, because only few interactions between the beam and the stripper gas will take place. If the pressure increases, so will the average charge state, until an equilibrium is reached, where capturing and losing electrons balance. This can be seen in fig. 4.3.3 for an incident ion energy of 1.14 MeV. C^+ is the most prominent charge state with 55% at low stripper pressure, but declines quickly to below 40%, when pressure rises. The C^{2+} and C^{3+} charge states increase in importance with higher areal density of the gas and C^{2+} becomes the dominant charge state with a fraction of 58%. C^{4+} contributes only 0.4% for the highest stripper pressure at this low terminal voltage. Beyond $0.6 \mu\text{g}/\text{cm}^2$ the fractions change considerably less with increasing thickness, signalling that equilibrium is reached. The right-hand side plot of fig. 4.3.3 shows a comparable measurement by Sarkar [Sar+12] at an ion energy of 1.04 MeV. In this measurement the C^+ fraction is lower by around 10% and the C^{3+} higher by the same amount. C^{2+} and C^{4+} show comparable fractions for both measurements.

The measurements for higher terminal voltages can be found in the appendix (A.2.1). The same behaviour is apparent, but shifted to higher charge states: C^{3+} becomes the prominent charge state starting at 2.545 MV and C^+ the lowest one at high stripper pressure. However, for low gas pressure C^+ remains the dominant charge state throughout all beam energies, but the one for 2.5 MeV, where C^{2+} is slightly higher.

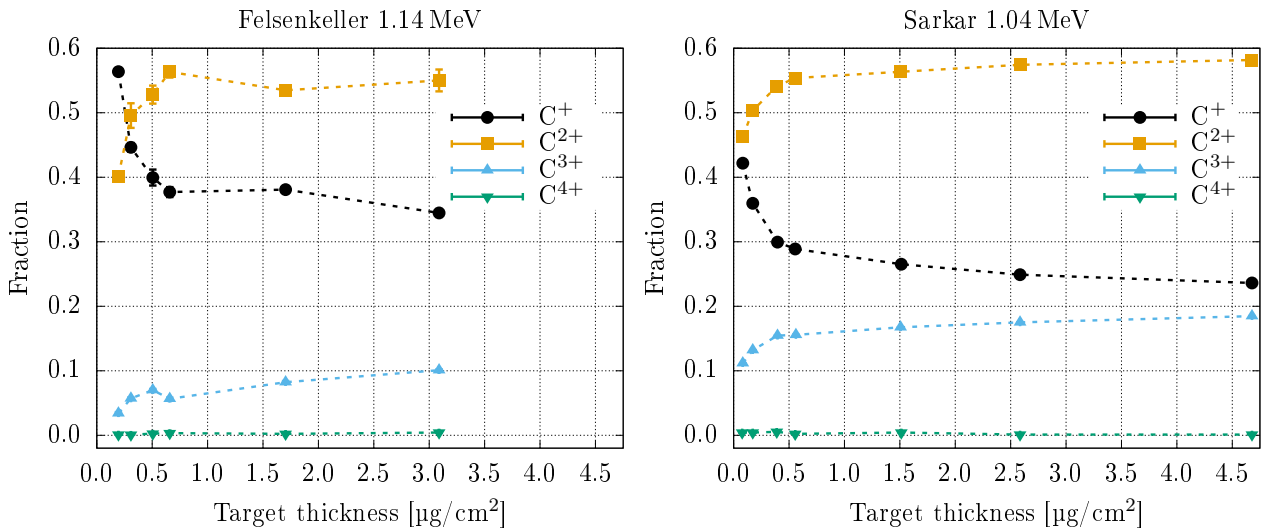


Figure 4.3.3: Charge fractions for different stripper pressures at 1.14 MeV beam energy for the Felsenkeller data (left) and 1.04 MeV for measurements by Sarkar (right) [Sar+12]. Lines were included to guide the eye.

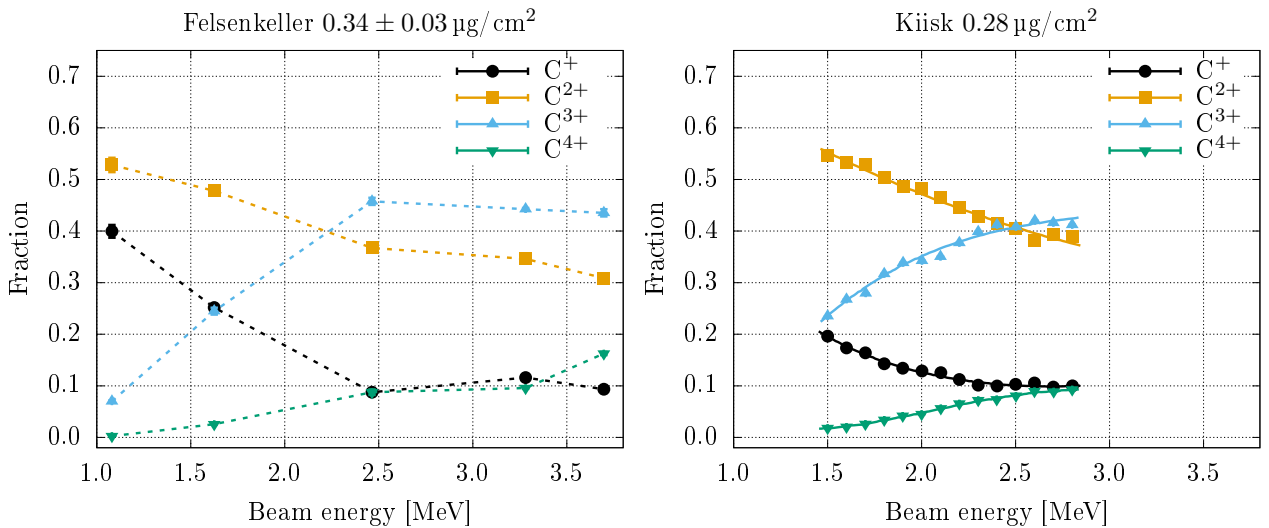


Figure 4.3.4: Charge fractions for different beam energies at a non-equilibrium areal nitrogen density of $0.34 \mu\text{g}/\text{cm}^2$ for Felsenkeller (left) and $0.28 \mu\text{g}/\text{cm}^2$ for Lund with a ^{13}C beam (right).

4.3.5 Charge state distribution for different terminal voltages

In order to examine the dependence of the charge state distribution on the terminal voltage, and therefore the energy of the beam particles, one has to keep the stripper pressure close to constant for the different voltages. This proved to be difficult, because the control of the stripper pressure is done by a remotely controlled valve. Every change in the valve will have a delayed influence on the stripper pressure and an equilibrium is only reached after around half an hour. Furthermore, the beam current influences the pressure in the stripper as well. Therefore, the stripper pressure varied by 9% for different terminal voltages for the plot shown in fig. 4.3.4, 2% for fig. 4.3.5 and from 2% to 5% for the ones shown in the appendix (fig. A.2.2). This is negligible for stripper pressures beyond the equilibrium pressure, where the charge fractions vary only slightly with the target thickness. Though, it might influence the charge states below the equilibrium target thickness.

The behaviour of the charge distribution with terminal voltage is similar to increasing the stripper pressure. This is shown for a non-equilibrium pressure in fig. 4.3.4. At a low terminal voltage the two lowest charge states are in the majority with over 90%. Then they decline, while the 3+ and 4+ states increase. 3+ becomes the prominent one with 36% at the highest beam energy of 3.7 MeV. 4+ increases over the whole energy range from below 1% to 10%. The measurement at Lund [Kii+02] was done at a similar areal density of $0.28 \mu\text{g}/\text{cm}^2$, but with a ^{13}C beam. Further, they showed, that the charge distributions of ^{12}C and ^{13}C do not differ, as expected. Nevertheless the two data points at 1.6 MeV and 2.45 MeV, that overlap in these two measurements, deviate between Felsenkeller and Lund. While for 1.6 MeV C^+ and C^{4+} are equal, C^{2+} is higher by 7%, C^{3+} is lower by the same amount in the Felsenkeller measurements. For 2.45 MeV C^+ is higher by 9%, C^{2+} equal and C^{3+} and C^{4+} lower by 7% and 2% respectively at Felsenkeller.

In the equilibrium state (see fig. 4.3.5) it is visible, that the 3+ charge state has a peak and declines to lower and higher energies. The same can be said for the 2+ and 4+, where the peaks are just outside the measured energy range. Charge state 1+ indicates a similar behaviour with a peak at even lower energies than the 2+ one. This trend agrees with measurements and calculations by Suter *et al.* [Sut+18], where the peaks for the charge states are shifted to lower energies, because argon was used as a stripping gas instead of nitrogen.

This behaviour is caused by the slightly increasing cross section for capturing an electron with increasing beam energy, while the chance of losing an electron decreases noticeably (see fig. 4.3.1). Therefore, higher charge states will get more and more populated on the cost of the lower charge states. Implications of this on future experiment will be discussed in subsec. 4.3.7.

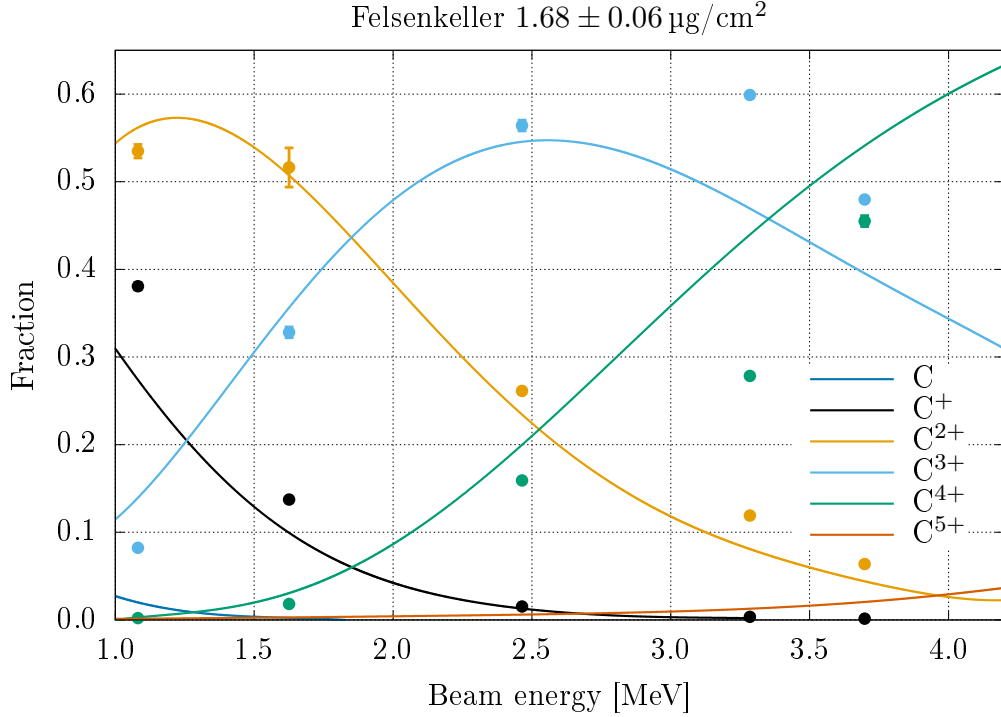


Figure 4.3.5: Charge fractions for different beam energies at an equilibrium areal gas density of $0.52 \mu\text{g}/\text{cm}^2$ for Felsenkeller. Solid lines are scaled calculations based on experimental determined cross sections and charge distributions by Suter *et al.* [Sut+18] for argon as a stripping gas.

4.3.6 Transmission

From these measurements and the number of ions shot into the accelerator given by FC2, the transmission through the accelerator to FC4 can be calculated. This is an interesting property to check, if the focus and positioning of the beam on the low-energy side of the accelerator is sufficient for transmission through the accelerator. Additionally, it is possible to investigate, if and where parts of the beam are lost. For the planned experiments the fraction of the beam reaching FC4 with a given energy is of interest and will be examined below.

The total transmission from FC2 in front of the accelerator to FC4 behind the high-energy magnet is shown in fig. 4.3.6. The overall transmission is best for the 2524 keV beam, where 90% are reached. For the low energy beams the overall transmission ranges from 30% to 50%, while it is between 65% to 88% for the two highest beam energies. For low stripper pressures transmission is low, because of losses in the accelerator due to bad focusing and beam atoms in the neutral charge state, while for high ones, beam is lost, because the beam emittance is increased by the higher number of scattering processes inside the stripper medium.

For the approximation, that the mean charge is the same at FC3 and FC4, this can be split up into two parts: the transmission through the accelerator and the HE beamline. However, since the transmission of different charge states is highly dependent on the quadrupole, this assumption might not hold for bad transmission through the HE beamline. On FC3 only the

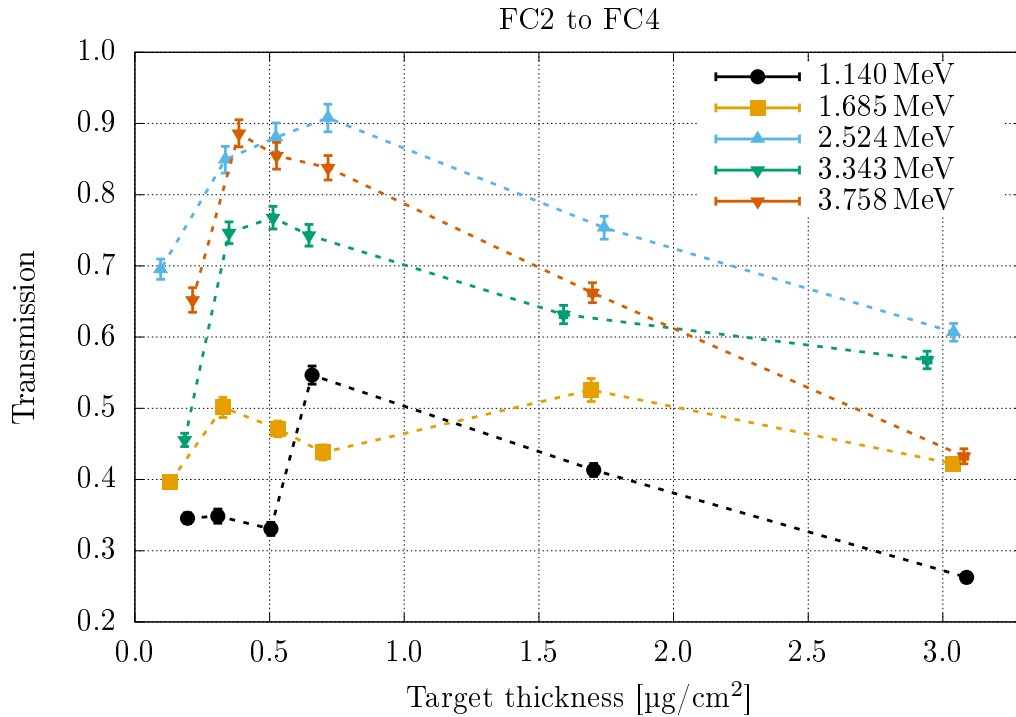


Figure 4.3.6: Transmission from FC2 to FC4. Lines are included to guide the eye.

sum of all charge states can be measured, so that the mean charge at this position and with this the particle current, is not clear. This property can only be determined on FC4, where parts of the different charge states might already be lost. With the assumption that losses are more heavily for the higher charge states, the measured mean charge at FC4 will be lower than the one on FC3, but was taken to calculate the particle current on FC3 anyway. This results in a higher particle current at FC3 and a lower transmission than approximated. This effect is taken into consideration in the uncertainties, where the maximum corresponds to only C^+ and the minimum to only C^{4+} getting lost in the HE beamline.

Both cases, transmission through the accelerator and the HE beamline, are displayed in fig. 4.3.7. The above described trend for total transmission holds true for these cases as well. Low terminal voltages have the lowest transmission through the accelerator, because the column electrodes and therefore the focus is optimized for higher voltages. In these cases shorting rods can be inserted to improve the focus for lower beam energies, which was not done, because of time constraints.

In general, transmission through the accelerator increases with higher beam energies with the exception of 3343 keV. In this case, transmission is lower, probably because the einzel lens or the beam position on the LE beamline was not optimal.

For transmission through the HE beamline, a similar behaviour can be seen. It is best for low stripper pressures and then declines steadily, with exceptions for the first four stripper pressures at a beam energy of 1685 keV. Here the quadrupole was only optimized for the first charge state by mistake, leading to losses for higher charge states.

A reason for beam losses in the HE beamline could be other ions than carbon in the beam. In order to investigate this, the HE magnet was increased from 0 A to 300 A while the terminal voltage was at 3.3 MeV, the target thickness at $3\mu\text{g}/\text{cm}^2$ and the beam current on FC3 at $26\mu\text{A}$. Apart from the first four carbon charge states, only negligible currents of below $0.04\mu\text{A}$ could be observed, apart from C^{5+} , which contributed $0.18\mu\text{A}$.

4.3.7 Lessons for experiments

While subsecs. 4.3.4 and 4.3.5 focused only on the fractions of different charge states and subsec. 4.3.6 on the transmission of all charge states, an experimentalist desires an intense ion beam of a given energy, which can be calculated with eq. 4.1.1.

The best charge state is determined by a combination of the charge state distribution and the transmission. While the charge fraction might be high at the equilibrium target thickness, the transmission already has declined at this point. A lower charge state at higher terminal voltage, where the fraction is at a maximum at lower target density, might be more favourable then.

So the data described above was evaluated, to determine, which charge state is suited the best for an experiment at several laboratory energies between 3 and 10 MeV. It is to be noted, that no energy calibration of the accelerator was available and therefore the terminal voltages for each charge state with the same resulting beam energy might deviate slightly. Additionally, it was not clear, whether the set terminal voltage or the read-back by the GVM could be trusted, both differ by around 1.5%. For the calculated beam energies the latter was used.

The results are shown in tab. 4.3.1. In order to achieve high particle currents on FC4 for low to medium energies the 2+ charge state seems to be favourable, where roughly 30% of the ions shot into the accelerator reach FC4. Only at the highest energy 3+ outperforms the 2+ state, where almost 50% are detected behind the magnet.

Considering the terminal voltage stability (see subsec. 4.1.2), lower voltages might be better for shooting onto the target, because of the smaller energy spread, which is negligible for shooting onto the cups, but has an influence when focusing on the target.

E_{beam} [keV]	$I_{\text{FC4,q}}/I_{\text{FC2}}$		
	1+	2+	3+
3304	0.246 ± 0.010	0.308 ± 0.013	-
4950	0.269 ± 0.011	0.303 ± 0.013	0.138 ± 0.011
6600	0.221 ± 0.009	0.35 ± 0.06	0.173 ± 0.008
7455	0.268 ± 0.011	0.323 ± 0.014	0.313 ± 0.018
9900	-	0.295 ± 0.012	0.470 ± 0.020

Table 4.3.1: Comparison of particle current of different charge states for various beam energies. Black entries are from the stripper pressure measurements, while numbers in grey were measured later on.

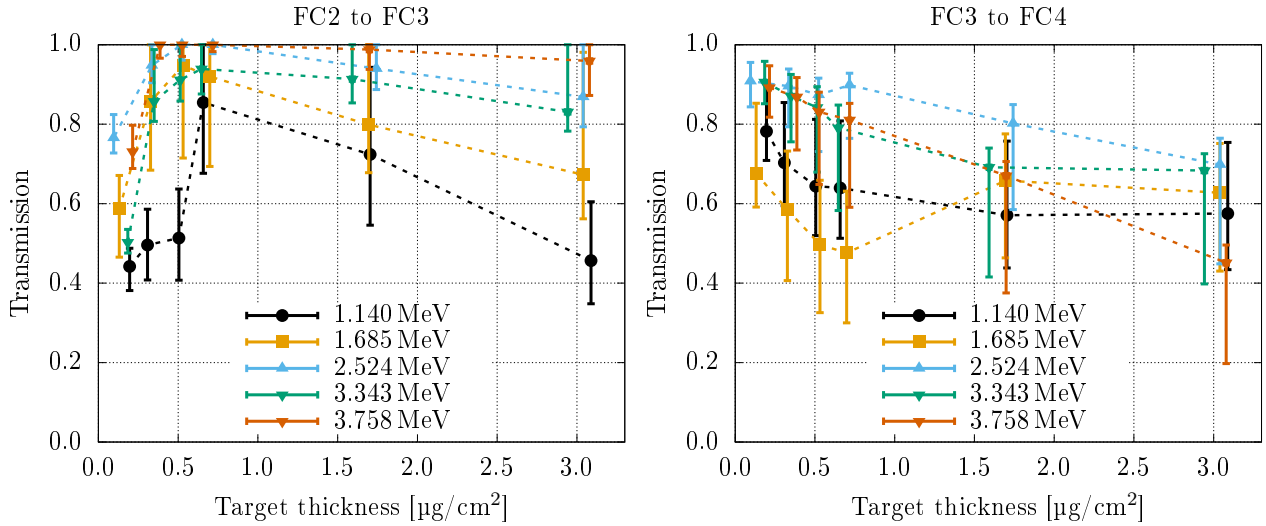


Figure 4.3.7: Transmission through the accelerator (left) and the HE beamline (right). Lines are included to guide the eye. Uncertainties take into account, that the beam losses might change the mean charge of the beam at FC4 compared to FC3. See text for more details.

Another option to increase particle beam current for a given laboratory energy is to use $^{12}\text{C}_2^-$. The ion source provides a third to a half of the $^{12}\text{C}^-$ current for this ion (see sec. 3.5). Since it will split up in the stripper, a similar charge state distribution at the exit of the accelerator is to be expected. Because of the lower current shot into the accelerator, stress on the terminal potential stabilizer will be reduced. However, higher terminal voltage will be necessary. Still, there could be an advantage by using this ion in terms of the terminal voltage stability, since it seems to be impacted more by the beam current than by higher voltage (see fig. 4.1.3). Unfortunately, this could not be tested in the scope of this thesis.

In order to increase overall current the transmission through the HE beamline needs to be improved. Possible solutions for this problem were already discussed earlier in subsec. 4.2.2.

5 Towards a measurement of the $^{12}\text{C}(\alpha,\gamma)^{16}\text{O}$ reaction at Felsenkeller

$^{12}\text{C}(\alpha,\gamma)^{16}\text{O}$ is one of the key reactions to be measured at the Felsenkeller laboratory. First tests were done in inverse kinematics with a carbon-12 beam on a helium-4 implanted solid target. The solid target will be replaced by a ^4He gas-jet target and an extended gas target later. With the higher target density of this setup, measurements down to a centre-of-mass energy of 0.6 MeV are in principle possible.

This chapter will present Monte-Carlo simulations of the detectors and target chambers used for the experiment. After that, a first test measurement will be described in detail. The last section will report on the optimization of the setup for a second measurement.

5.1 Monte Carlo simulations

There are multiple reasons why a simulation-based geometrical model of the detectors and the experimental setup can be helpful during the planning as well as the analysis stage of an experiment. For the high-energy region the well-known $^{27}\text{Al}(p,\gamma)$ reaction is often used to determine the efficiency of high-purity germanium (HPGe) detectors [Ili08]. Unfortunately, the proton beam by the internal ion source was not available for this thesis.

Therefore, extrapolation has to be performed from the low energy region, where the efficiency can be measured using radioactive calibration sources, leading to significant uncertainty in the high-energy region. In order to avoid this, Monte Carlo simulations, verified with the already mentioned calibration sources in the low-energy region, can be employed to obtain the high-energy efficiency. This is especially important for the determination of physical quantities like the cross section from experiments, but also impacts the planning of experiments. With the accurate detector efficiency, the feasibility of the experiment for different setups can be derived, for example, whether less detectors at a close distance perform better than more detectors, which are placed further away.

The implementation of the setup was done in two ways: a direct GEANT4 implementation using the classes and functions provided by the toolkit and the import of GDML files. GDML is a XML-based language to describe geometries for GEANT4. CAD drawings can be exported as step files, which approximate the geometry by tessellation with triangles. These step files

can then be converted to GDML files and imported into GEANT4.

The physics list "Shielding2.1 EMZ" was used with GEANT4 version 10.4.p02. See subsection 2.4.2 for more details. Since all necessary physics processes are included, it is suitable for this application as well.

This section reports on the setup of a GEANT4 simulation for two types of detectors: the Miniball Triple Cluster detector and the Euroball Septuple Cluster, the verification of the setup and derived quantities of the simulation.

5.1.1 Cluster detectors

Two types of Cluster detectors are present at Felsenkeller: the Miniball Triple Cluster, that hosts three encapsulated HPGe crystals, with 60% relative efficiency each, in one cryostat and the Euroball Septuple Cluster with seven such crystals. The GEANT4 implementation of both are displayed in fig. 5.1.1. Originally, the Clusters were part of a larger setup containing several of these clusters in a honeycomb structure, for example the EUROBALL configuration for the Septuple Clusters [Ebe+92], in order to achieve a large covering of the solid angle around the target chamber.

5.1.2 The encapsulated HPGe Crystal

The crystal geometry, which is shown in fig. 5.1.2, is adapted to their use in these clusters: In the front they are shaped hexagonally with a distance of 61.35 mm from flat to flat, while in the back they are cylindrical with a diameter of 75 mm tapered with an angle of 4.125° . The length of each crystal is 78 mm. The anode of the crystal is a lithium-diffused cylindrical core drilling of 10 mm diameter and 63 mm length at the back of the crystal. With this geometry they are best suited for a position at a distance of 43.6 cm to the target [Ebe+92].

The capsule containing the HPGe crystal and the preamplifier were implemented by using a GDML-file created from a CAD drawing by Toni Kögler (HZDR). This capsule was then positioned three times for the Triple Cluster and seven times for the Septuple Cluster at the corresponding positions inside the frame of the respective detector housing. However, there are no dead layers for the crystal implemented in the source file. Therefore these are created from the GDML solid by using the G4IntersectionSolid class for the dead layers and the G4SubtractionSolid class for the remaining active crystal. With this procedure two dead layers with adjustable thicknesses were implemented in the crystal: a disk on the front of the crystal with thickness $d_F \approx 0.3$ mm and a cone at the rear with height $h_C \approx 25$ mm. The latter is necessary, because of space charges, that distort the electrical field in the rear of the crystal [Li+18], where about 10% (corresponds to $h_C \approx 20$ mm) of the germanium was covered by the cone. Introducing these dead layers reduced the deviations of simulation and experiment tremendously. The resulting crystal in the simulation is shown in fig. 5.1.2.

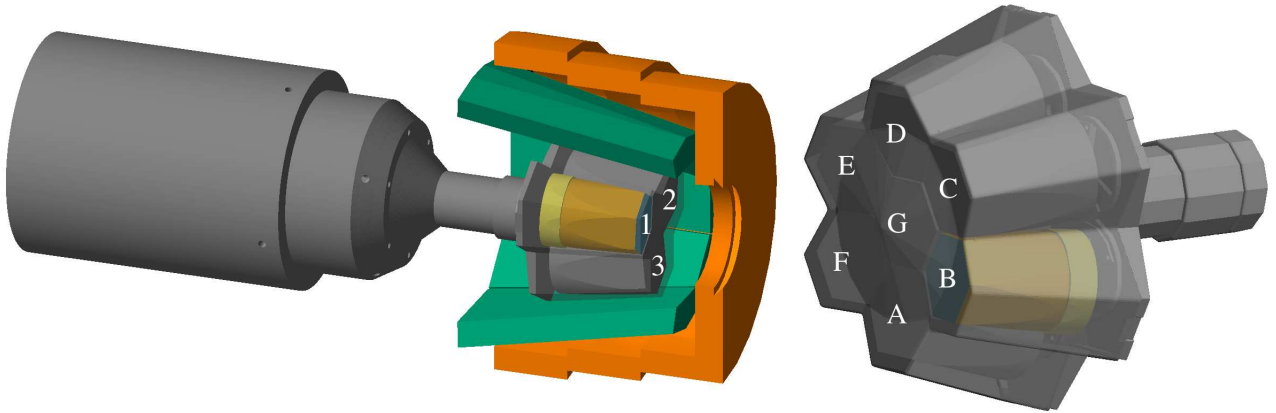


Figure 5.1.1: Implementation of the Triple Detector (left) and the Septuple Detector (right) in the simulation. The lead shielding is displayed in orange, the BGO crystals in bluish-green, the dead layers in blue, the active crystal in orange and the preamplifier in yellow. For both detectors one capsule and the housing was set transparent for clarity. The names of the crystals are indicated as well.

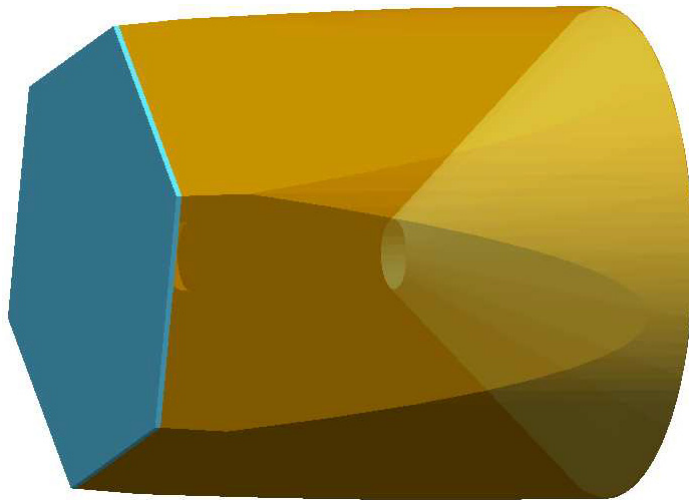


Figure 5.1.2: GEANT4 implementation of the encapsulated HPGe Crystal. Two dead layers (blue) are assumed: a flat area at the front of the crystal and a cone in the back. The active crystal is displayed in orange.

5.1.3 General approach for the verification of the simulation

The verification was done in two stages: verification of the detector and of the target chamber. The first includes a measurement, where the radioactive source is not shielded by additional material from the detector. For this, four different calibration sources were placed at a distance of 25 cm for the Triple Cluster Miniball (MB1) and 16.7 cm for the Septuple Cluster Euroball (EB17), between source and front cap of the detector. The used calibration sources are listed in tab. 5.1.1. The Miniball measurement was performed by Max Müller on 25.10.2019 as part of his Bachelor's thesis [Mül20] under my supervision. The measurement with the 55° target chamber and the calibration sources mounted at the target position took place on 23.03.2020 and the bare Septuple one on 20.05.2020.

The same setup was simulated by placing a number of radioactive nuclides at the same distance as in the experiment, mimicking a perfect point source. The number of nuclides was calculated from the activity of the source and the date and the duration of the measurement. These then decay following the G4RadioactiveDecay class. The deposited energy is saved in histograms for each individual crystal. Additionally, a fourth histogram is filled with the sum of the deposited energy in all three crystals for one decaying atom, called the addback.

In the following, the results of the simulations are compared to the experiment. For this, the measurement is analysed by two scripts, that create an energy-calibrated histogram of the measurement, that is comparable to the simulation after a background spectrum scaled to the measurement time was added to the simulation data.

All further analyses were done with the same script for both simulation and experiment. For the calculation of the peak entries, first the centre of the peak was determined by a fit to the following equation:

$$N(E) = p_0 \cdot \exp(-0.5((E - p_1)/p_2)^2) + p_3 \cdot E + p_4, \quad (5.1.1)$$

with the fit parameters p_i with $i = 0$ to 4. The area under the peak N_{ROI} , including the background, was then calculated by summing up the bin entries in the interval $[p_1 - 5p_2, p_1 + 5p_2]$. Furthermore the Gaussian fit serves as a possibility to cross-check the results.

The background is estimated by two areas in the same distance below and above the peak

Isotope	Activity at reference date [kBq]	Date of reference	Half-life [d]
^{57}Co	28.96(14)	01.06.19	271.74
^{60}Co	260.7(9)	01.01.05	1925.28
^{133}Ba	13.96(7)	01.06.19	3853.75
^{137}Cs	11.309(6)	01.01.05	10 986.7

Table 5.1.1: Activity of the gamma sources of different isotopes as taken from the data sheet.

with the same width. The counts in the background are then:

$$N_{\text{BG}} = \frac{1}{2} \frac{d_{\text{Peak}}}{d_{\text{BG}}} (N_{\text{IBG}} + N_{\text{rBG}}), \quad (5.1.2)$$

with d_{Peak} the width of the peak, d_{BG} the width of the background area and N_{IBG} and N_{rBG} the counts in the left and right area, respectively. Width and position of the two areas were adapted for each calibration source to account for local structures in the background. The procedure is shown in fig. 5.1.3. Subtracting the estimated background counts from the entries in the region of interest (ROI), gives the number of peak entries.

With that, the efficiency is calculated as follows:

$$\varepsilon = \frac{N_{\text{ROI}} - N_{\text{BG}}}{\eta \cdot N_{\text{total}}}, \quad (5.1.3)$$

with the number of summed up entries in the ROI $[p_1 - 5p_2, p_1 + 5p_2]$ N_{ROI} , the number of entries in the background N_{BG} , the total number of decayed atoms N_{total} and the emission probability η of the gamma line for the isotope.

In principle, summing effects could occur for closely positioned intense sources, where either photons of the decay of two different nuclei reach the detector in coincidence or two gammas of a cascade transition are detected. While the second effect is implemented in the simulation by the G4RadioactiveDecay class, the first is not taken into account, because one simulated event only consists of one decaying nucleus. However, summing peaks could only be observed for the ^{133}Ba source in the case of the Triple Cluster close to the target chamber. There, this peak could be reproduced by the simulation, as can be seen in fig. 5.1.4, indicating, that two photons of the same decay reach the detector.

The analysis was done for all used isotopes and detector crystals. Dividing the resulting efficiency of the simulation by those of the experiment, one derives an easy tool to determine how to adjust the simulation to accurately describe the experiment, by slightly adjusting the distance of the source and the dead layers of the crystals.

If all points of the simulation are above or below the experiment, this can be remedied by changing the distance of the detector following the inverse-square law or the active volume of the detector. Since it proved difficult to accurately determine the exact location of the detector during the measurements and all crystals will be affected in the same manner, changing their distance was preferred. Low-energy gammas will be affected mostly by a dead layer in the front of the crystal, because they are scattered or absorbed, before they will reach the end of the crystals. Photons with higher energies can pass through a thin layer in the front nearly unobstructed and reach deep into the crystal. Therefore, the dead layer in the rear will impact these more. Photons with energies in-between these, are only slightly affected by the introduced dead layers and serve as a double check for the positioning of the detector.

Since the distance of the detector to the source affects all crystals and all photon energies, it

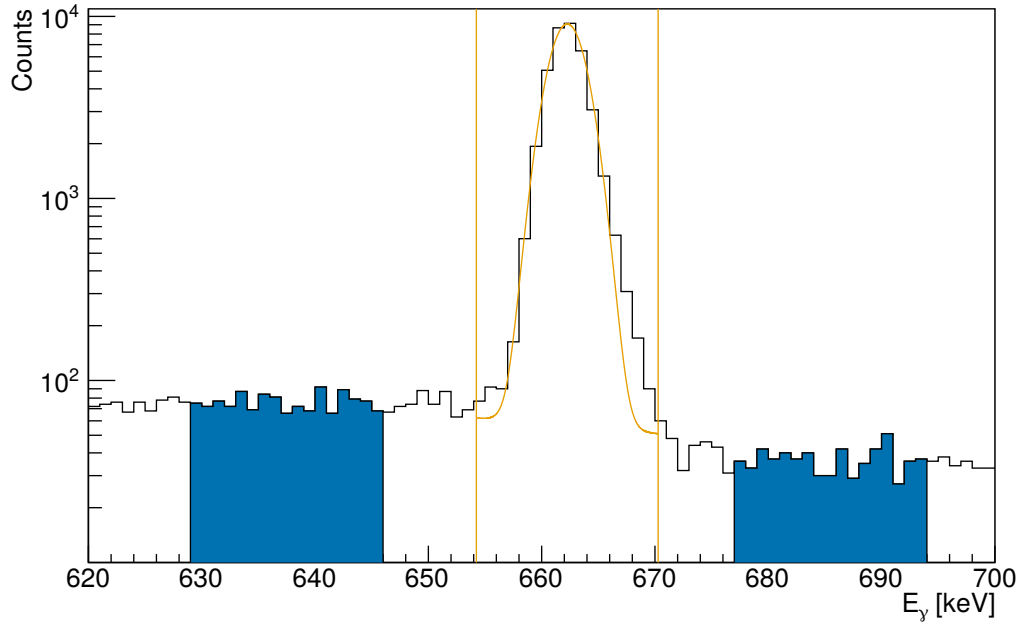


Figure 5.1.3: Procedure to determine the entries in a peak for the ^{137}Cs measurement in 25 cm distance of the Miniball detector in addback mode. First the peak is fit with eq. 5.1.3 (orange). Then the area, in which the entries of the histogram are added, is determined by 5σ around the peak. Afterwards two areas (blue) to the left and the right of the peak are used to determine the background in the peak area. See text for more details.

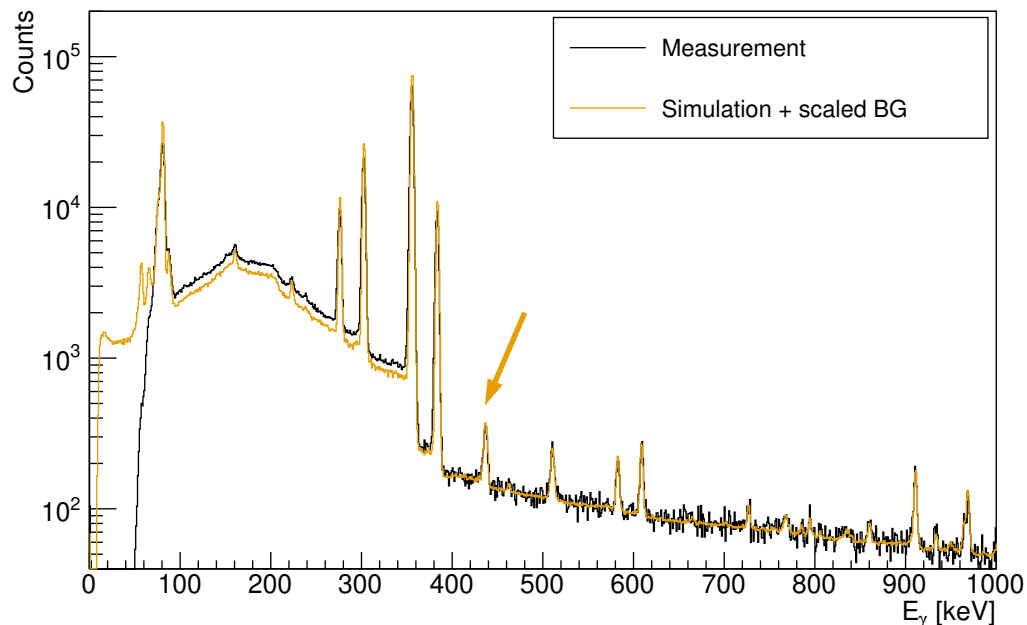


Figure 5.1.4: Comparison of the simulation with added scaled background (orange) to the measurement (black) for the ^{133}Ba source mounted on the 55° target chamber and MB1 in a distance of 12.3 cm. The simulation fits the measurement data very well. The summing peak of the 80.5 keV and the 356.01 keV line, indicated by the orange arrow, is reproduced by the simulation as well.

was adjusted first and afterwards the dead layers of the individual crystals.

In the second stage the target chamber setup has to be verified. For this the detector is placed on the position, where it would be in the upcoming experiment, and the calibration sources are mounted at the target position. Instead of the implanted targets used for the main experiment, a tantalum disk was mounted as a backing for the radioactive source. Furthermore, the water cooling cycle was started, but the chamber was not evacuated. However air instead of vacuum inside the target chamber has a very small effect on the resulting efficiencies with about 0.03% at 0.2 MeV and less than 0.01% at 10 MeV [Ber+10].

5.1.4 The simulation of the Miniball

The Miniball detector consists of three parts: the detector itself, an aluminium frame with a BGO scintillator inside and a lead shielding consisting of three rings and a collimator. The BGO is used as a veto detector to filter muons passing through the HPGe crystals and photons scattered out of them, while the lead shields against the natural radioactivity. The detector itself was included from the already mentioned CAD drawing by Toni Kögler via GDML. The crystals were then modified with dead layers by the method described in subsec. 5.1.2. The aluminium frame was implemented from a CAD drawing provided by Andreas Hartmann (HZDR) and the eight BGO crystals placed inside the frame with GEANT4 solids by Louis Wagner (HZDR). The lead shielding is built in this way as well and provides the ability to adapt the collimator in thickness and opening angle. The implementation of the Miniball in GEANT4 can be seen in the left panel of fig. 5.1.1.

For the Miniball MB1 four different radioactive calibration sources (see tab. 5.1.1) were placed at a distance of 25 cm to the front cap of the detector. Adjusting the simulation to reproduce the experiment best, the resulting dead layers are listed in tab. 5.1.2.

Fig. 5.1.5 illustrates the difference between simulation and experiment after the adjustments for the addback of the Triple Cluster. The results of the single crystals can be found in the appendix. The efficiency resulting from the simulation now represents the one from the experiment closely over a wide energy range.

5.1.5 The simulation of the Euroball

The Septuple Cluster EB17 is based on a GDML file by Guang-Shun Li [Li+18]. It contains the housing, the seven crystals with only a dead layer at the rear, the preamplifiers and the connection to the dewar. Furthermore there were BGO back catcher included, that were not used in our experiment, so these were excluded. The crystals were switched with the ones described in subsec. 5.1.2. In the case of the Euroball the whole geometry is based on a GDML import and can be seen in fig. 5.1.1.

To verify the detector, this time only three calibration sources were placed in a distance of

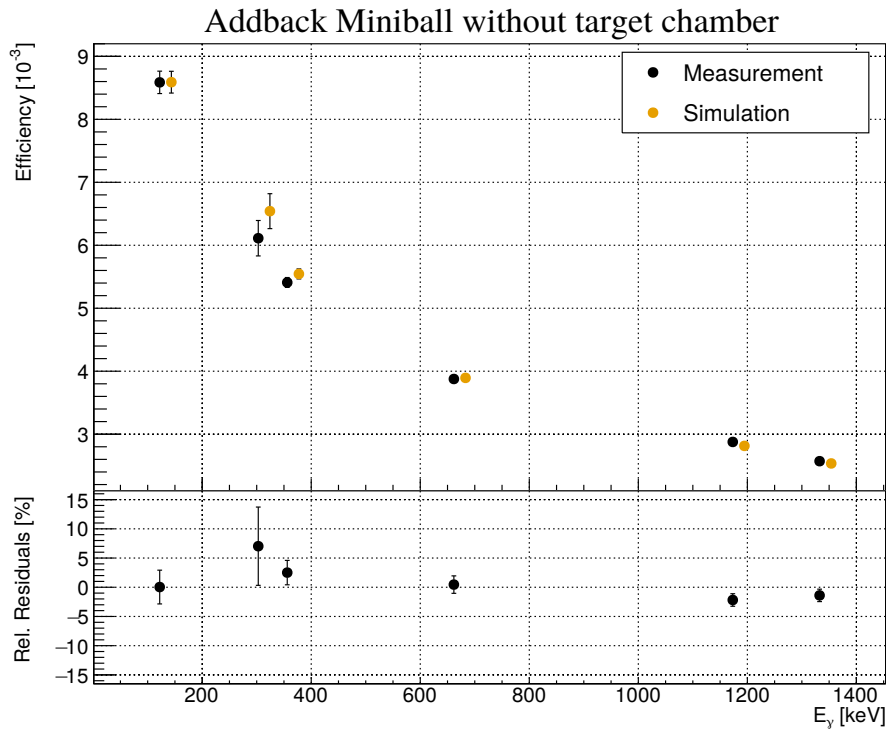


Figure 5.1.5: Comparison between the efficiency of the addback Miniball for experiment and simulation. The source was placed at a distance of 25 cm to the frontcap of the detector. The residuals are below 10% for all energies. The simulation data was moved to the right for better visibility.

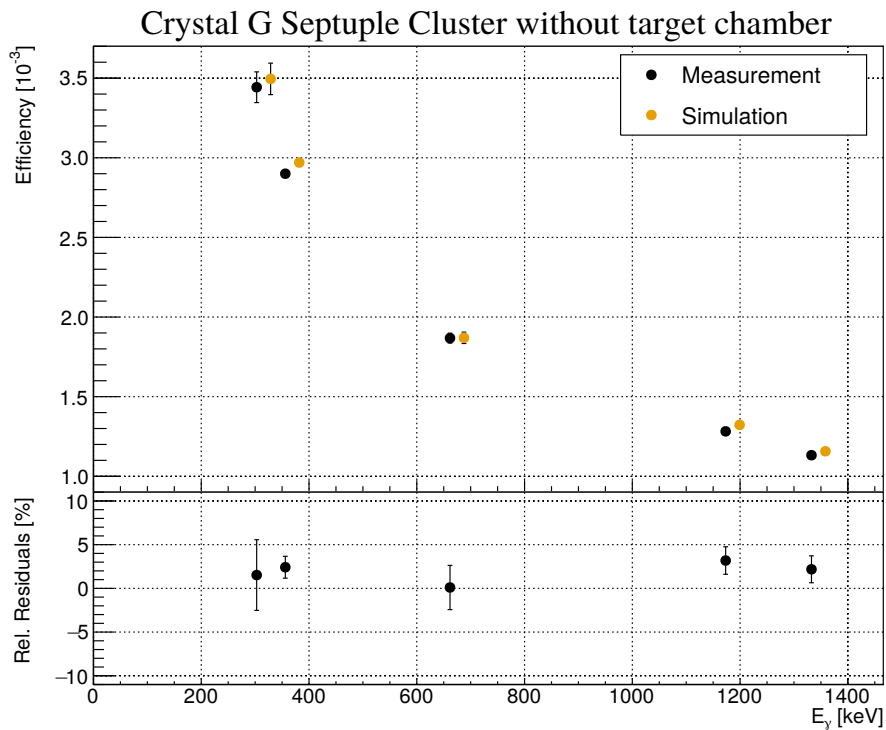


Figure 5.1.6: Comparison between the efficiency of crystal G of the Septuple Cluster for experiment and simulation. The source was placed at a distance of 16.7 cm to the frontcap of the detector. The relative residuals are below 5% for all energies. The simulation data was moved to the right for better visibility.

16.7 cm. ^{57}Co was not used, because for some crystals the two low-energetic lines were already on the falling slope of the efficiency, since the detector setup was optimized for high-energy gammas. In the case of crystal B, this affected the ^{133}Ba lines as well. Therefore, for the Septuple Cluster only the single crystals were compared, because crystal B has an effect on the adback spectrum. Later on, this capsule stopped working completely. It could not be tested in the scope of this thesis, whether the subsequent repair affected the verification of the crystal and if the adapted front dead layer of 0.3 mm is a good value.

For the source measurements without the target chamber, no change of the detector distance was necessary. By adding the dead layers, very good agreement between the experiment and the simulation could be reached. A list of the dead layers can be found in tab. 5.1.2, while a plot of the derived efficiencies for the central crystal G is shown in fig. 5.1.6. The other crystals can be found in the appendix.

	MB1			EB17						
	1	2	3	A	B	C	D	E	F	G
d_F [mm]	0.2	0.3	0.2	0.8	0.3	0.1	0.4	0.35	0.25	0.35
h_C [mm]	21	23	22	32	26	24	26	33	25	23

Table 5.1.2: Dead layers of MB1 and EB17, that were used for the simulation. While the size of the front dead layer d_F is comparatively small, the height of the cone h_C is quite large and takes away 10 to 15% of the active crystal volume, comparable to [Li+18].

5.1.6 Verification of the target chamber

The target chamber in the simulation was directly implemented in GEANT4 by Louis Wagner and improved by Max Müller. It consists of a tube, with an endcap at a 55° angle with respect to the beam. This endcap holds the target, which is water-cooled at the back. The setup modelled in GEANT4 is shown in fig. 5.1.7. The analysis procedure described above applies here as well and the adjustable parameters are the positioning of the detector, the wall thickness of the target chamber and the water cooling reservoir in the back of the target.

The best result for the adback of the Miniball detector is plotted in fig. 5.1.8. The germanium crystals of the Miniball were in a distance of 12.3 cm to the source inside the target chamber. The thickness of the latter was not adapted, since the result was already satisfying with the nominal value. Here, the simulation only differs by a maximum of 4% from the experiment. A plot of the residuals of all other crystals can be found in the appendix.

For the measurement with the target chamber, the Septuple Cluster is with 4.6 cm very close to the source. So slight mispositioning or a tilt of the detector axis will affect the comparison between measurement and simulation. Furthermore the target chamber geometry is more complicated, because it includes the water cooling. Therefore, deviations from the experiment

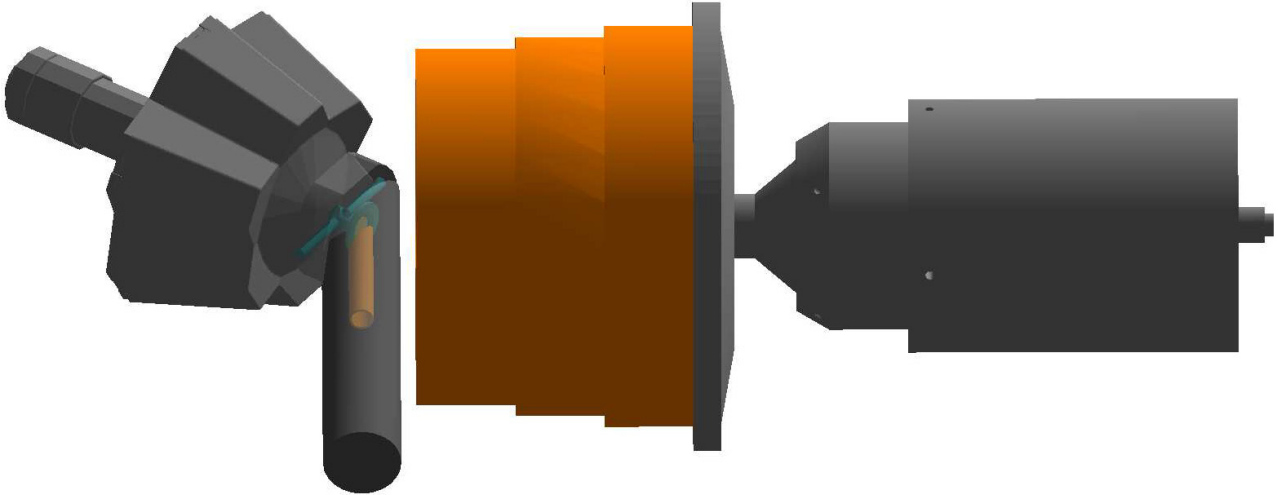


Figure 5.1.7: Setup of the simulation for the efficiency calibration. The Triple Cluster is positioned as close as possible at 90° with respect to the beamline, while the Septuple Cluster is at 55° . The target (yellow) itself is attached by the target holder (bluish green) at 55° as well. Furthermore, the target chamber hosts water cooling (blue) for the target and a copper tube (orange), which serves as a cold trap and as suppression for secondary electrons.

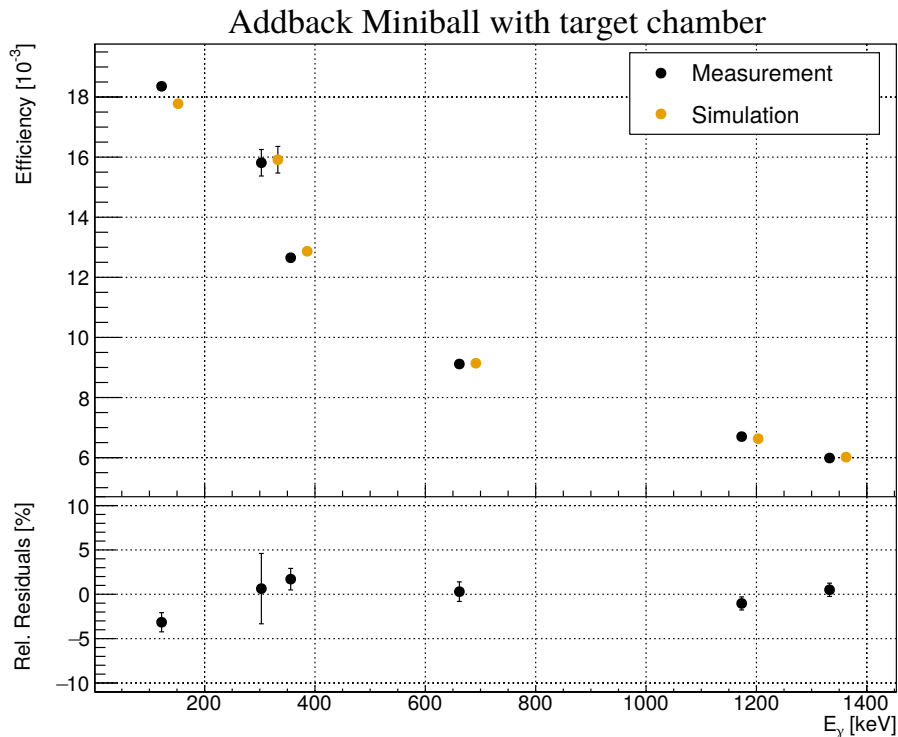


Figure 5.1.8: Comparison between the efficiency of the addback of the Triple Cluster for experiment and simulation. The source was placed on the target position of the 55° target chamber in 12.3 cm distance to the detector. The simulation data was moved to the right for better visibility.

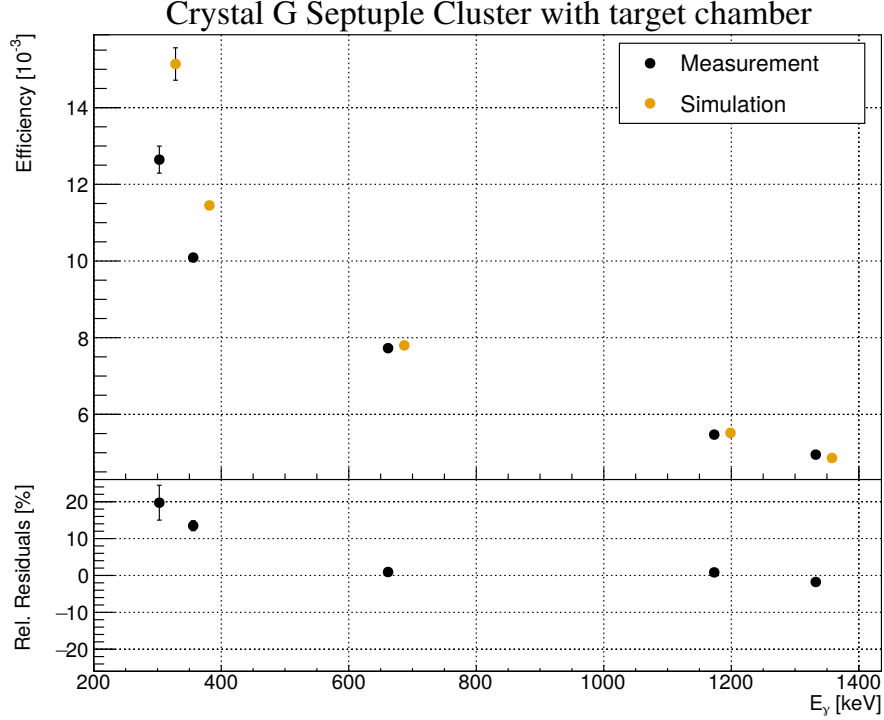


Figure 5.1.9: Comparison between the efficiency of the Septuple Cluster for experiment and simulation for crystal G. The source was placed on the target position of the 55° target chamber in 4.6 cm distance to the detector. The simulation data was moved to the right for better visibility. The high-energy lines are described well, while the simulation overestimates the efficiency of the low-energy lines.

are higher for the Septuple Cluster. The result can be seen in fig. 5.1.9. Since for the present purpose the high-energy lines of crystal G are important and seem to be described well, it was refrained from adjusting the tilt and positioning of the detector to reach better agreement. Plots for the other crystals are in the appendix.

5.1.7 Optimization of the setup

For the experiment, the energy of the gamma is influenced by the Doppler shift and the recoil energy [Ili08]. The resulting gamma energy can be calculated as follows:

$$E_\gamma = Q + E_{\text{CMS}} + E_{\text{Doppler}} - E_{\text{Recoil}}, \quad (5.1.4)$$

$$E_\gamma = 7.162 \text{ MeV} + E_{\text{CMS}} + \frac{v_{\text{B}}}{c} E_\gamma \cos \Theta - \frac{E_\gamma^2}{2m_{\text{B}}c^2}, \quad (5.1.5)$$

with E_{CMS} the energy in the centre-of-mass system, v_{B} the velocity of the bound nucleus, m_{B} the mass of the bound nucleus and Θ the angle of the γ with respect to the incoming particle. The angular distribution is given by [deB+17] and shown in fig. 5.1.10. For the assumption

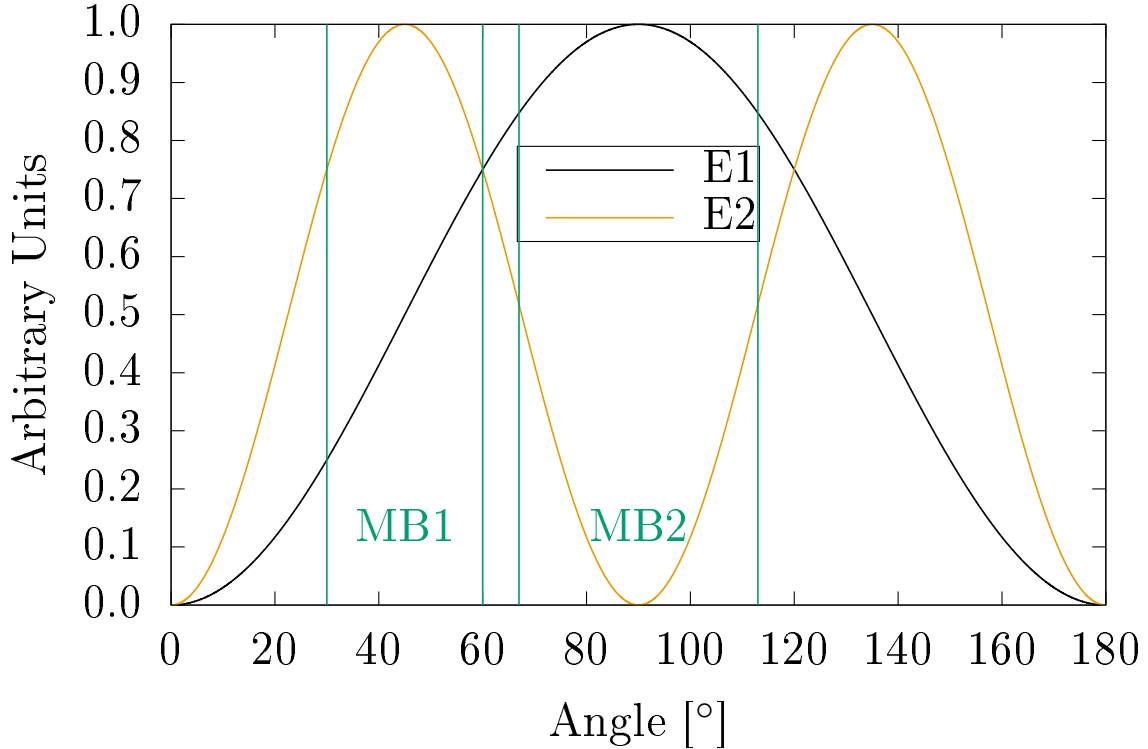


Figure 5.1.10: Angular distributions for the E1 and E2 contributions of the reaction $^{12}\text{C}(\alpha,\gamma)^{16}\text{O}$ according to deBoer [deB+17]. The area covered by the two detectors during the first test is marked in bluish-green.

of a pure E2 transitions, which is reasonable in the case of this relatively narrow, strong resonance, the simulated spectra for the setup used in the first test (see next section) are shown in fig. 5.1.11. Note, that the energy resolution of the detectors was only verified for low-energy gammas and might differ from the experiment at 10 MeV and that the here used target chamber was not verified yet. For MB1 the full-energy, the single-escape and, with less counts, the double-escape peak are clearly visible. MB2, which is positioned at 90° , exhibits two full-energy peaks, that are caused by the angular distribution, where only the edges of the outer crystals detect the Doppler-shifted gammas and two single-escape peaks. As a result of this simulation, for the first test the full-energy and the single-escape peak are expected in MB1, while MB2 might show no peaks, because the intensity is reduced strongly. Because of beam time restrictions the setup could not be changed during the experiment. Still, MB2 is useful to rule out E1 contributions and ease the identification of background lines.

When the simulation is run with this setup and a gamma source sending out $5 \cdot 10^6$ gammas with an energy of 9.842 MeV, which photons from the E2 resonance at $E_{\text{CMS}} = 2.68$ MeV of the $^{12}\text{C}(\alpha,\gamma)^{16}\text{O}$ would have, the detector efficiency is $\varepsilon = (5.84 \pm 0.11) \cdot 10^{-4}$ for crystal G in the centre of the Septuple Cluster. Crystals F and C are directly above and below crystal G and therefore have a comparable Doppler shift of 100 to 220 keV. Each of those has an efficiency of around $2 \cdot 10^{-4}$, so the total efficiency would be $(9.87 \pm 0.14) \cdot 10^{-4}$ plus an addback factor, that

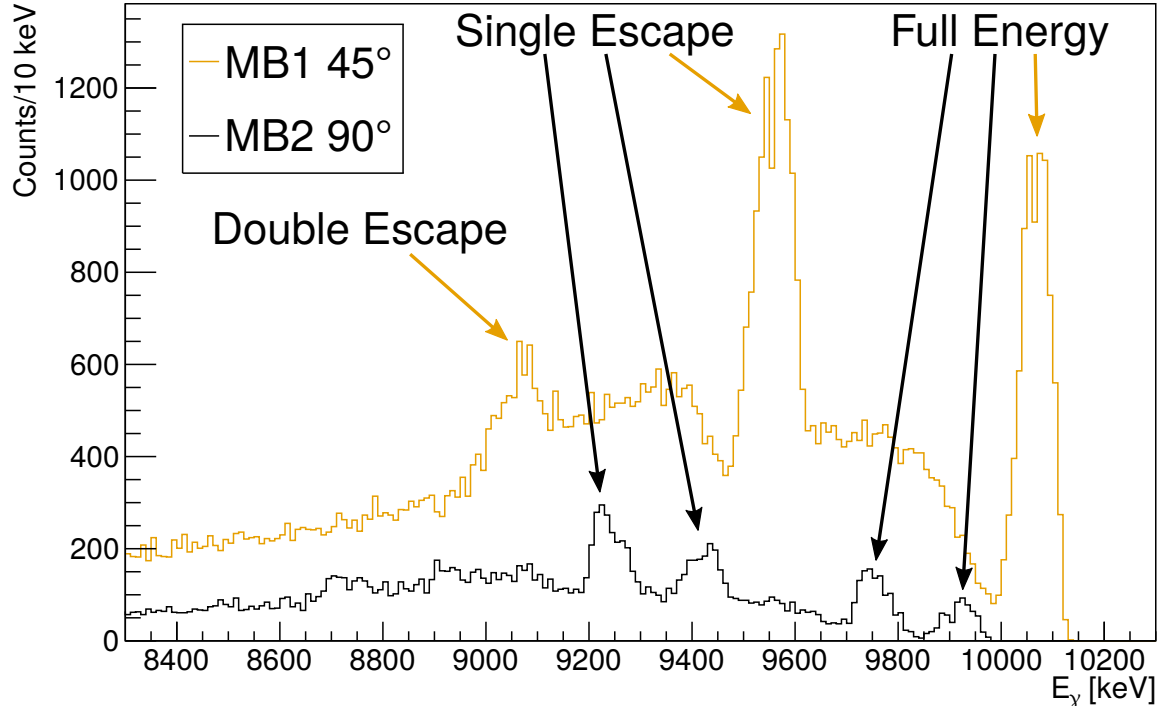


Figure 5.1.11: Simulated addback spectra for 10^6 started gammas of energy 9842 keV for detectors MB1 and MB2. Theoretical angular distribution of a pure E2 transition, Doppler shift and recoil energy are implemented for the gammas.

was not calculated in the simulation. The other crystals could be used as veto in this setup, because due to the large Doppler shift at this close distance with -20 to 80 keV for crystals A and B and 220 to 320 keV for E and D, they barely overlap. Another option would be, to correct the single spectra of all crystals for the Doppler shift and then calculate the addback spectra, like it was done in [Vaj+15] with the DALI2 array.

The Septuple Cluster could be moved further away, the BGO veto installed around it and then the Compton-suppressed addback spectrum used. However, already at 8 cm distance, compared to 4.6 cm before, the efficiency with addback is comparable with $(10.68 \pm 0.15) \cdot 10^{-4}$, while a correction of the Doppler shift would still be necessary.

As a comparison, the first test setup with the Y-shaped target chamber and the Compton-suppressed Triple Cluster at 18.5 cm distance at 45° (see next section) had an efficiency of $(4.77 \pm 0.09) \cdot 10^{-4}$ according to the simulation.

5.2 First test measurements at Felsenkeller

The first test to measure the reaction at Felsenkeller was conducted in inverse kinematics with a solid target. The aim of the test was to gather experience in operating the accelerator non-stop for an extended period of time and seeing a first signal of the reaction and possible background reactions. For this reason, two resonances were aimed for during the experiment:

a broad E1 resonance at $E_{\text{CMS}} = 2.35$ MeV and the E2 resonance at 2.68 MeV with the highest S-factor for a ground state transition in the low-energy region.

5.2.1 The experimental setup

The high-energy beamline was already described in detail in sec. 4.2. This part is followed by the target chamber. For the first test it consisted of a cold trap with a copper tube of 1.7 cm radius, that served as secondary electron suppression (SES) as well. The cold trap was not filled with liquid nitrogen during the experiment.

Usually, a collimator would be installed in front of the copper tube, however, since at the point of the experiment both beam focus and positioning were not well, as described in the previous chapter, it was decided to do without one in order to maximize current on the target. Due to last-minute changes of the setup, the copper tube was too short and had a gap of several centimetres to the target itself. This resulted in inaccurate current information, since no electron suppression was present and the beam might be able to hit the target holder instead of the target itself. The prior could be verified by experimental data, that the target current was higher with a voltage on the SES of 800 V than the current on FC4.

The target chamber installed, was a Y-shaped tube, that was designed for another experiment. The target was inserted from the end of the beamline perpendicular to the beam. Furthermore, it was water cooled from the back. High vacuum in the order of 10^{-6} mbar was ensured by a turbo pump, which was positioned at the cold trap. The cold trap itself was not filled with liquid nitrogen during this measurement campaign.

The target chamber is shown in fig. 5.2.1, while a photo of the detector setup can be seen in fig. 5.2.2.

5.2.2 Targets

The targets were produced at the Ion Beam Centre at the Helmholtz-Zentrum Dresden-Rossendorf by implanting helium-4 into tantalum backings. The tantalum plates with a diameter of 27 mm and 0.2 mm thickness were cleaned prior to implantation with an ultrasonic bath and propanol.

For the implantation, it was aimed for a flat profile of helium with a thickness of 100 nm. Building on the experience of helium-3 implanted targets for another experiment by Steffen Turkat (TUD), SRIM was employed to simulate the implantation process and determine the implantation energies as well as the fluences to reach a nominal target thickness of $5.55 \cdot 10^{17}$ at/cm², which corresponds to one helium atom for every tantalum atom in the 100 nm thick layer.

The best result was achieved with a fluence of $6.9 \cdot 10^{17}$ cm⁻² at an implantation energy of 15 keV, followed by 3 keV with $3.8 \cdot 10^{16}$ cm⁻². The resulting helium profile as calculated by

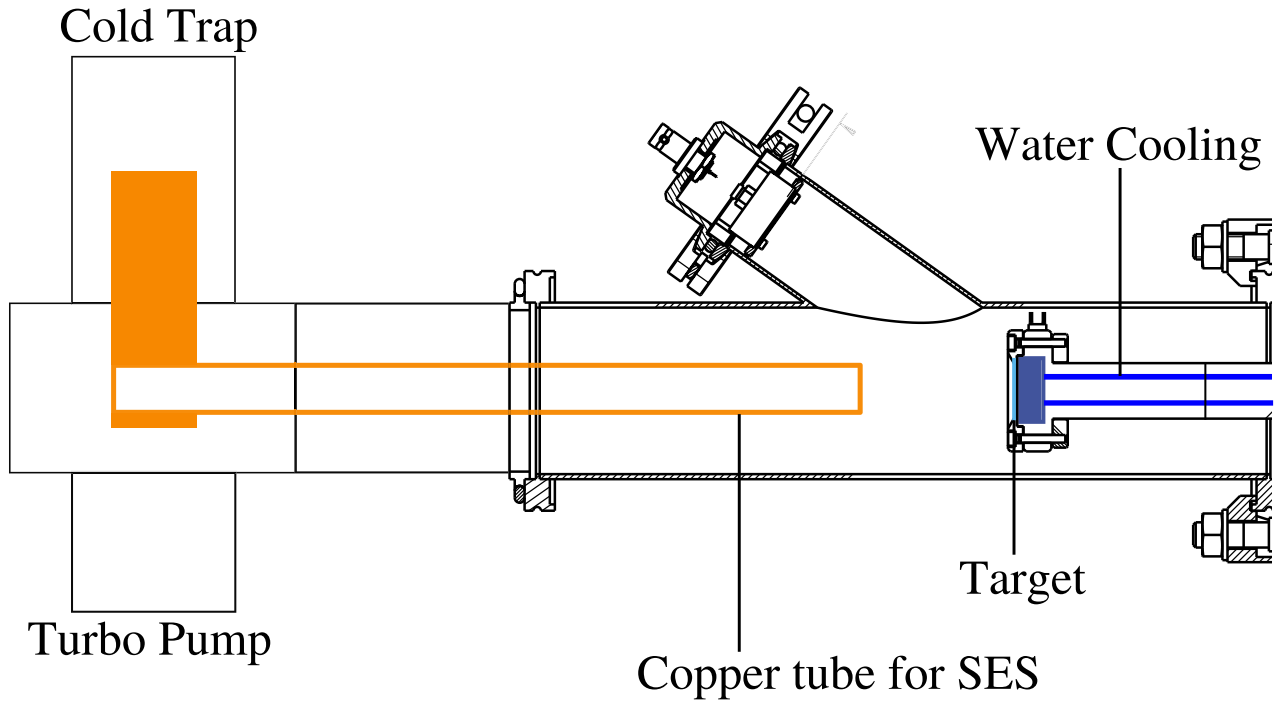


Figure 5.2.1: Schematic view of the target chamber for the first test measurement. The beam enters from the left, passes through the copper tube of the cold trap (orange, not filled) and reaches the water-cooled target.

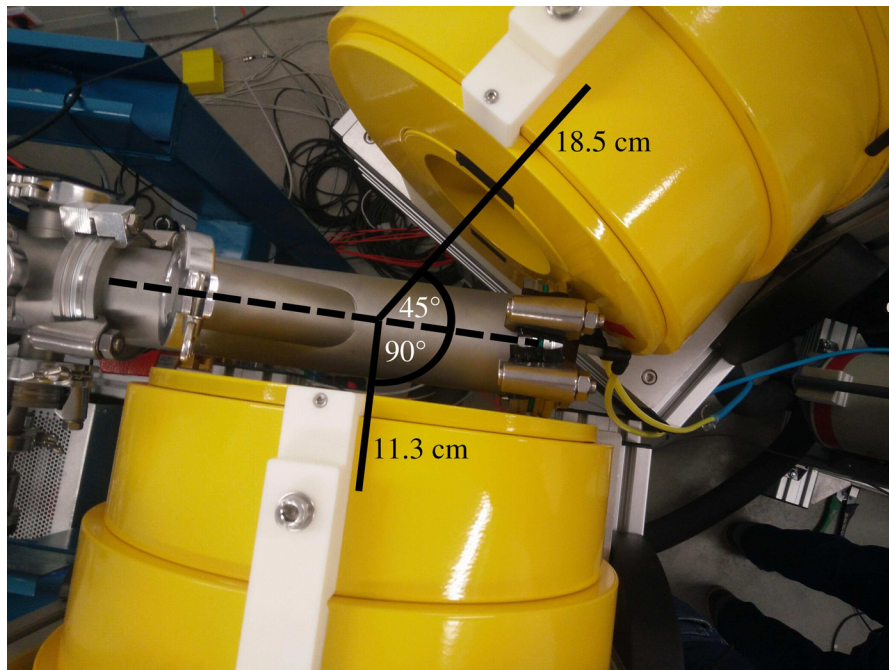


Figure 5.2.2: Detector setup for the first test measurement. Two Miniball detectors are positioned at 90° and 45° with respect to the beamline. Both are shielded by lead and BGO. The particle detector tube is at the top and did not host a silicon detector during the experiment. The cold trap is positioned to the left.

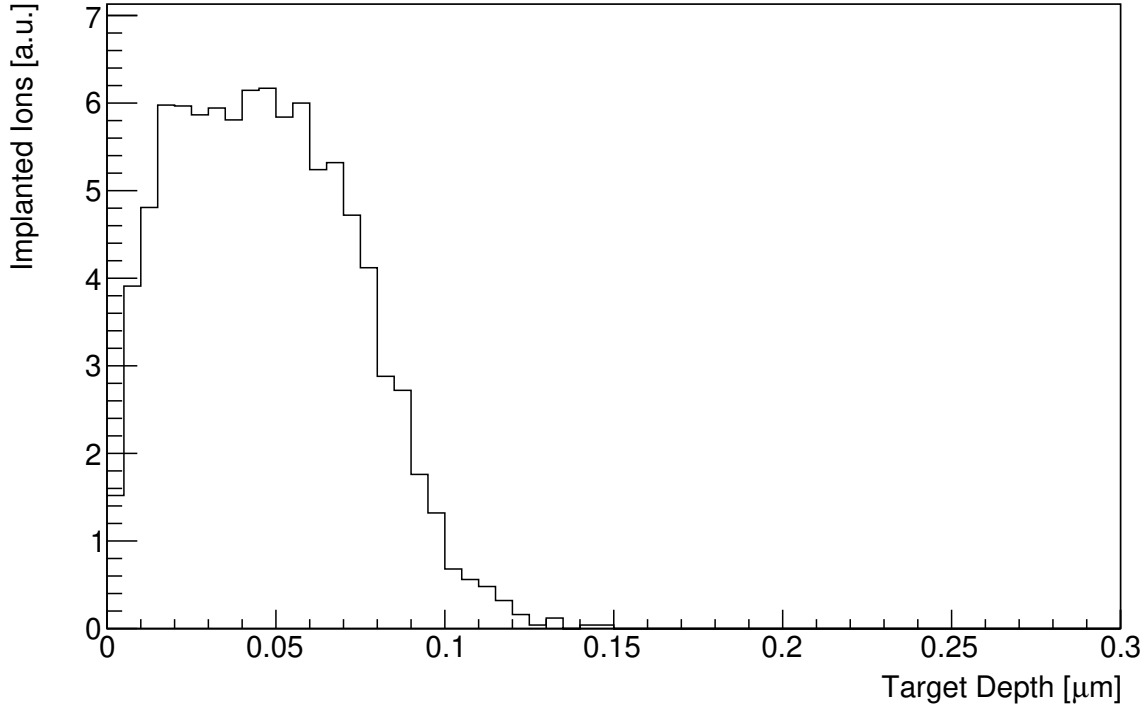


Figure 5.2.3: Target depth profile calculated with SRIM for a target density of $5.55 \cdot 10^{17}$ at/cm² with a thickness of 100 nm.

SRIM is shown in fig. 5.2.3. During the implantation at the 40 kV implanter of the HZDR Ion Beam Centre, the targets were cooled with liquid nitrogen and the whole target area was implanted.

In total, three targets were used during the irradiation at Felsenkeller, called FL1, FL3 and FL5. All were implanted with the above described procedure. Target FL1 was evaporated with an additional tantalum layer of 82 nm prior to implantation at the magnetron sputter facility at the magnetism department of HZDR.

After irradiation, the targets were analysed by Elastic Recoil Detection Analysis (ERDA) at the HZDR 6 MV Tandetron. For this, they were irradiated with a 43 MeV Cl^{7+} beam at an angle of 70° in an area of $2 \times 2 \text{ mm}^2$. Heavy elements were detected at a scattering angle of 30° in a Bragg Ionisation Chamber. For helium and hydrogen, a solid state detector protected by a $25 \mu\text{m}$ kapton foil was placed at 40° with respect to the beamline. In total, five points were analysed: one on the beam spot and one off the beam spot for targets FL1 and FL5, respectively and one on FL4, that was not irradiated. FL3 was not analyzed.

Evaluating the unused target FL4, it becomes apparent that roughly 50% of the aimed for helium content is present in the target. Furthermore, impurities of $1.18 \cdot 10^{17}$ at/cm² oxygen, mostly on top of the target and carbon with $0.75 \cdot 10^{17}$ at/cm² were found. Hydrogen is distributed throughout the target with $0.96 \cdot 10^{17}$ at/cm².

The irradiated targets show lower hydrogen and oxygen content both on and off-spot. However, carbon build-up on top of all used targets is apparent, with a maximum of $5.19 \cdot 10^{17}$ at/cm²

Target	Areal density [$10^{17}\text{at}/\text{cm}^2$]			
	He	H	C	O
FL1 spot	1.23(1)	0.250(5)	5.19(22)	0.76(6)
FL1 off	1.850(1)	0.49(1)	3.08(17)	0.41(3)
FL5 spot	0.90(1)	0.120(3)	1.39(11)	0.97(8)
FL5 off	2.18(1)	0.68(1)	1.59(12)	0.73(7)
FL4	2.46(1)	0.96(1)	0.75(9)	1.18(10)

Table 5.2.1: Results of the ERDA analysis for two irradiated targets (FL1, FL5) and one not irradiated (FL4). Spot refers to the beam spot, while off denotes a location outside the beam spot.

of carbon on the beam spot of FL1. The helium content is lowered compared to FL4 by 11% and 25% outside the beam spot and by 50% and 36% in the beam spot for targets FL1 and FL5 respectively. A depth profile of the beam spot of FL5 is shown in fig. 5.2.4, while all areal densities are listed in tab. 5.2.1.

The amount of hydrogen, oxygen and helium is lowered in the irradiated targets. This can be explained by the beam heating the target, which causes outgassing of the targets. This might be reduced in future experiments by a broader beam or an improved cooling of the target, for example with liquid nitrogen instead of water. Only the carbon content increases with the irradiation, especially on top of the targets. Here, residual carbohydrates in the vacuum build-up on the target surface [Sug+79], which could be reduced by improving the vacuum by filling the cold trap with LN_2 . Additionally, shooting with a carbon beam on the target, will lead to more carbon present in the target chamber, so it remains to be seen, how much the cold trap can lower this effect.

5.2.3 The detectors

The γ -ray detectors employed for the first test are described in detail in sec. 5.1. Two Miniball Triple Clusters, MB1 and MB2, with BGO and lead shielding around them were used. The voltages applied to the crystals can be found in tab. 5.2.2.

Since the two multipolarities of the reaction have different angular distributions (see fig. 5.1.10), the detectors were positioned in a way, that the maximum of the respective multipole is covered: MB1 at 45° with respect to the beam at 18.5 cm distance for the E1 and MB2 at 90° 11.3 cm

Cluster	MB1			MB2		
Crystal	1	2	3	4	5	6
V_{det} [kV]	3.5	4.0	4.5	4.5	4.5	4.0

Table 5.2.2: High voltages for the individual crystals of MB1 and MB2 during the experiment.

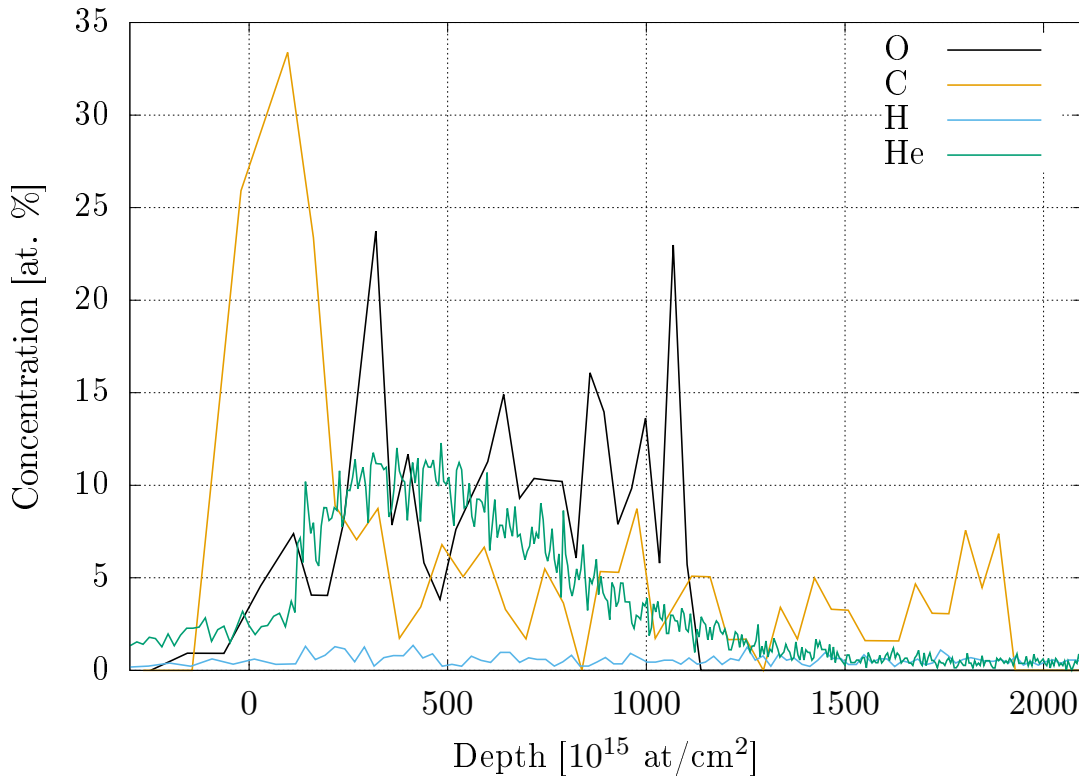


Figure 5.2.4: Target depth profile of the beam spot on FL5 by ERDA. The lines for C and O have been smoothed.

away for the E2 component. In order to achieve the highest possible efficiency, only a 3 cm lead collimator was used at the front and the detectors were positioned as close to the beamline as possible.

The energy calibration of the detectors was performed during the offline data analysis by fitting the background lines of ^{40}K and ^{208}Tl with 1460.82 keV and 2614.53 keV, respectively. Because in some of the runs the 2614.53 keV line is dominated by an in-beam background peak, this was done for four runs spanning the time of the experiment. For the following analysis, a mean of the energy calibrations of these four runs was taken, which differed only slightly.

5.2.4 Data acquisition

For the data acquisition the program "MC²" by CAEN was used. The analogue signal from the preamplifier of the detectors is connected to a digitiser of type V1725 by CAEN, where the timestamp and the deposited energy are derived from the signal. Each detector crystal of the two Miniballs has its own channel in the digitiser, while all BGO crystals for one Miniball are combined and occupy another channel in the digitiser.

The digitiser is connected with the "VME-USB2.0 Bridge V1718" by CAEN, from where the data is read out via USB by a laptop with the program "MC² v1.0.30.0". The trapezoid reconstruction algorithm is called DPP-PHA v.1.9.1 and the parameters for it are listed in

tab. 5.2.3, where t_{R} is the rise and the fall time and t_{FT} the duration of the flat top of the trapezoid. The height of the trapezoid is proportional to the deposited energy. All information is saved as binary list mode files, which are analysed offline later on. In the offline analysis the addback and the muon veto and escape-suppression is realized. The first by coincidence between individual crystals of the same cluster and the latter two by anti-coincidence between the BGO and the crystals.

Information on the deposited charge on the target is also read out by this system. Here, the current is converted to a digital signal by the "Digital Current Integrator 439" by ORTEC. Since the CAEN digitiser needs an analogue signal, the output is converted by a self-made digital-to-analogue converter with $R = 10\text{ k}\Omega$ and $C = 1\text{ nF}$, before it is connected to another channel of the digitiser.

5.2.5 Beam-induced background

Due to beam time constraints, no dedicated beam-induced background runs with a not-implanted tantalum plate were undertaken. Instead all the runs on the E1 and the E2 resonance were analysed for beam-induced background. A vast majority of the peaks is observable in both data at the two different beam energies.

The peak identification was done for the MB2 data. After that, the Doppler shifted peaks in MB1 were checked for consistency, with the help of the kinematics calculator of LISE++[TB04]. Since the energy calibration of the detectors could only be done for the low-energy area, peak locations in the high-energy area deviate by up to 30 keV. Unfortunately, CAEN gives no non-linearity factors for their digitizers. In future experiments a high-energy calibration line would help ensuring the identification of the peaks.

Most background peaks could be attributed to reactions of the ^{12}C beam with impurities in the target, mainly ^{12}C and ^{16}O . For both reactions, p and α production are the most probable exit channels, leading to excited states of ^{20}Ne and ^{23}Na for ^{12}C and ^{24}Mg and ^{27}Al for the reaction with ^{16}O . The nuclear reactions and their Q-values are listed in tab. 5.2.4.

Another option would be reactions of ^{12}C with ^{13}C . Here, the n -channel leads to ^{24}Mg , while the p -channel results in ^{24}Na , that then decays to ^{24}Mg . Both could contribute to the found ^{24}Mg peaks. On the other hand, no clear signature of other de-excitation gammas and of ^{21}Ne , created by the α -channel, could be found. This suggests, that the carbon deposited on the

Cluster	MB1			MB2		
Crystal	1	2	3	4	5	6
t_{R} [μs]	3.0	3.5	3.0	3.0	3.5	3.0
t_{FT} [μs]	1.0	1.2	1.0	1.0	1.5	1.0

Table 5.2.3: Parameters t_{R} and t_{FT} for the trapezoid reconstruction for each individual crystal.

targets during the irradiation is mostly ^{12}C .

The high-energy area (see lower panel of fig. 5.2.5) is dominated by de-excitation lines of ^{24}Mg . There are some unidentified peaks above 9.9 MeV, that might stem from ^{24}Mg as well. Beginning at 10 MeV, ^{24}Mg has many levels, that de-excite by γ emission in this energy range. With the uncertain energy calibration at hand, an exact identification of these peaks was not possible.

A work by Fang *et al.* [Fan+17] displays a γ -ray spectrum from 0 to 5 MeV for $^{12}\text{C}+^{16}\text{O}$ at $E_{\text{Lab}} = 11.3$ MeV. The peaks identified in this paper are the same as the ones in this thesis, but the spectrum is only displayed up to $E_{\gamma} = 5$ MeV there.

Since oxygen is already present in the not irradiated samples (see subsec. 5.2.2), it is uncertain, if these background peaks can be reduced in future experiments with solid targets (see subsec. 5.3). Unfortunately, they are close to or in the area of interest for both the E1 and the E2 resonance.

The low-energy background features mostly peaks of ^{23}Na , as is displayed in the upper panel of fig. 5.2.5. The gamma spectrum is comparable to an experiment by Kettner *et al.* [KLR80] at a similar laboratory energy of 11.2 MeV.

Tab. 5.2.4 lists the cross sections for the beam-induced reactions as well. While the target densities of carbon, oxygen and helium are comparable, the cross sections for the reactions with the first two are higher by several orders of magnitude. Carbon has the highest target densities and cross sections and therefore, the $^{12}\text{C}+^{12}\text{C}$ are the most prominent in the spectrum.

5.2.6 Problems during the first test

The BPMs showed, that the mean of the beam exited the accelerator with 1 mm offset to the left and angled 0.06° to the left. At the entrance of the high-energy magnet, the beam is about 7 mm off. After the HE magnet, it exits at 9 mm to the left and is angled by 0.1° to the right in order to hit the target in the centre.

Therefore, prior tests of shooting at the target yielded only currents of less than 1 μA and the majority of the beam was absorbed by the collimator. As a consequence, no collimator was installed in front of the cold trap in the experiment to achieve higher currents.

Furthermore, it can not be ruled out, that parts of the beam hit the target holder as well,

Reaction	$^{12}\text{C} (^{12}\text{C},p)^{23}\text{Na}$	$^{12}\text{C} (^{12}\text{C},\alpha)^{20}\text{Ne}$	$^{12}\text{C} (^{16}\text{O},p)^{27}\text{Al}$	$^{12}\text{C} (^{16}\text{O},\alpha)^{24}\text{Mg}$
Q value [keV]	2241	4617	5171	6772
E_{CMS} [keV]	5500	5500	6286	6286
$\sigma(E_{\text{CMS}})$ [mb]	6.14	15.3	1.10	1.28

Table 5.2.4: Q values for possible background reactions and the respective centre-of-mass energies and the cross sections for the higher beam energy of 11 MeV. The latter are taken from [Agu+06] for $^{12}\text{C}+^{12}\text{C}$ and from [Pat+71] for $^{12}\text{C}+^{16}\text{O}$.

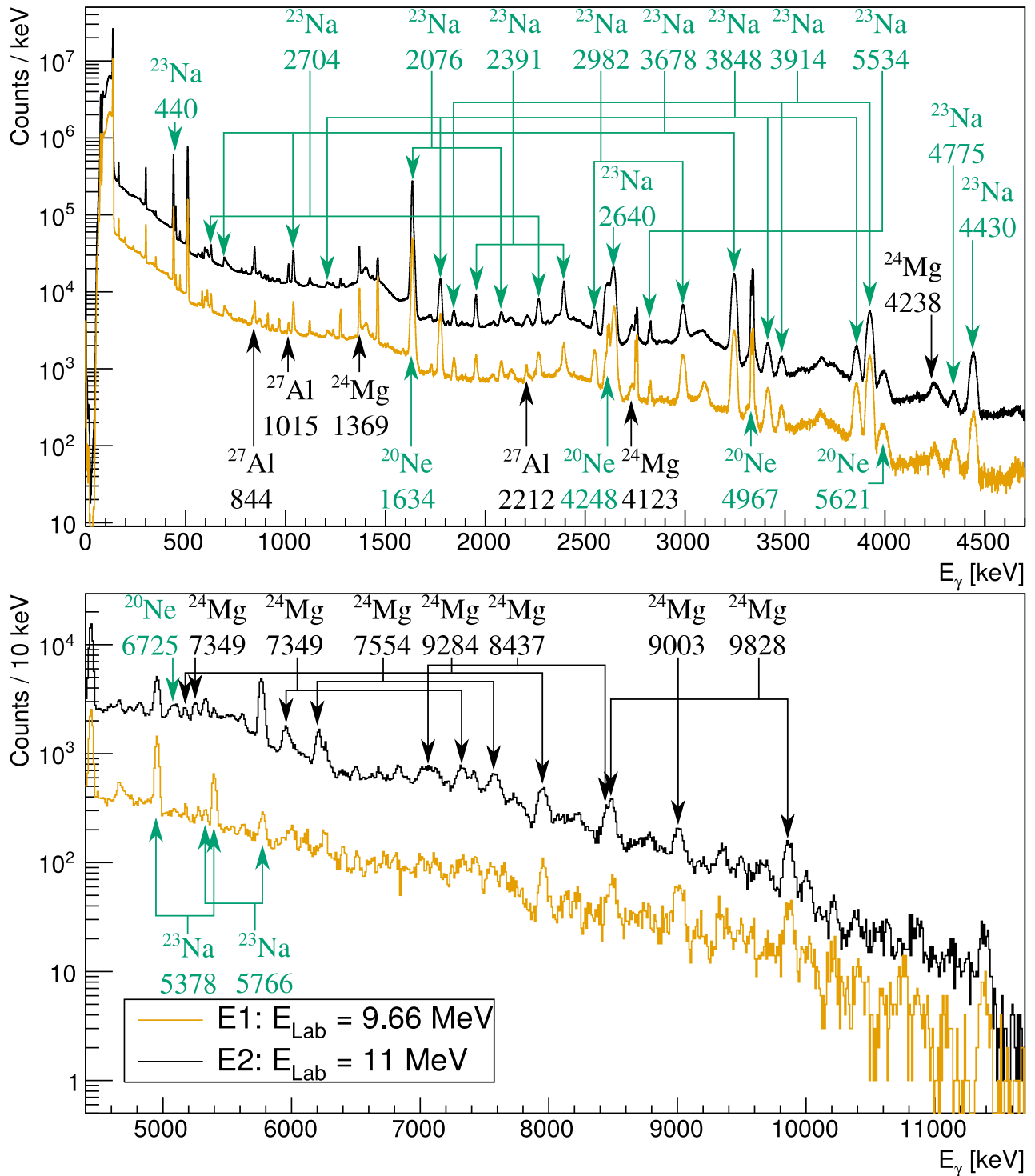


Figure 5.2.5: Spectrum of the E1 and E2 runs for MB2. Background peaks resulting from reactions of carbon with carbon are marked in bluish-green, with oxygen in black. For each peak the nucleus and the initial excitation level in keV is stated. Peaks above 10 MeV could not be clearly identified, see text for details. Note that the spectra are not normalized to each other.

because of the aforementioned beam alignment problems. However, visual inspection of the targets showed, that the beam spot is fully on the target (see fig. 5.2.6).

Another problem was the missing energy calibration of the accelerator. This could not be done beforehand, because the internal source, providing the proton beam for typical calibration reactions like $^{27}\text{Al}(p,\gamma)$, was not yet operable. Therefore, the necessary terminal voltages for the right laboratory energy could not be determined accurately, which, in case of the sharp E2 resonance at $E_{\text{CMS}} = 2.68 \text{ MeV}$, might have led to missing the resonance. The energetic target thickness calculated by SRIM was planned to be about 77.5 keV in CMS. The ERDA data shows a higher target thickness in CMS of about 120 keV. For a beam with charge state 3+, the accelerator voltage could have been 50 kV above the set value and the resonance would still have been inside the helium target. The same is true for an accelerator voltage, that is 70 keV below the set value.

The bottleneck for intense carbon beams was the stability of the accelerator. As shown in fig. 4.1.3, the terminal voltage gets unstable, if high beam currents are injected. This leads to a high beam energy spread and a wandering of the beam for several millimetres after the high-energy magnet and parts of the beam being absorbed instead of hitting the target. Exact quantities could unfortunately not be measured, because FC4 broke during the experiment and the target current was not electron suppressed. This problem was already improved while the internal ion source was running (see subsec. 4.1.2).

As proven by the ERDA analysis of the targets, carbon build-up is visible on the targets used and they contain impurities of hydrogen and oxygen. This leads to high-energetic background in the detectors by reactions of ^{12}C with ^{12}C and ^{16}O with ^{12}C . Especially the latter reaction resulted in background in the region of interest. Unfortunately, the oxygen is present in the unused target FL4 with 10 to 20% atomic concentration as well, so that these peaks will disturb future runs with solid targets.

Additionally, two beam times were scheduled for the experiment: Three weeks in December 2019 and January 2020 for the first and March and April 2020 for the second. Only one week of this time could be used for the experiment, because of necessary repairs. These are listed in tab. 5.2.5.



Figure 5.2.6: Target FL5 after two days of irradiation. The oval beam spot is clearly visible.

Week	Tasks
16.12.-20.12.19	Vacuum leak on the HE beamline, Conditioning
06.01.-10.01.20	Beam Alignment, Clean up after damage to a ^{22}Na calibration source
13.01.-17.01.20	$^{12}\text{C}(\alpha,\gamma)^{16}\text{O}$
02.03.-06.03.20	Conditioning
09.03.-13.03.20	Stripper gas measurements (see sec. 4.3)
16.03.-20.03.20	defect of rotating shaft motor: no terminal voltage possible

Table 5.2.5: Scheduled beam time for the experiment and defects on important parts, that caused a delay of the schedule.

5.2.7 Achievements of the first test

During the beam time, that spanned over four days, the accelerator was running continuously without major problems. Furthermore, the external ion source provided steady currents of 20 to 30 μA of ^{12}C in a low current setup for around 24 h until the sputter target got changed. During this time only minor adaptations in the beam optics had to be undertaken, paving the way to unsupervised operation at night. About 5 to 20 $\text{p}\mu\text{A}$ of not secondary electron suppressed carbon current reached the target during the whole time, as can be seen in fig. 5.2.7. The long-term test of the facility was quite successful.

Even though beam optics were not optimal, beam current could be steered onto the target for the duration of the experiment, resulting in visible beam spots on the target and in-beam background peaks. A test run on a hydrated titanium target resulted in a clear signature of the $^{12}\text{C}(p,\gamma)$ reaction. The spectrum for this run is shown in fig. 5.2.8 for MB2. The peak is at 2358 keV, the Q value of the reaction is 1943.5 keV and the beam energy in the centre-of-mass system was $E_{\text{CMS}} = 451.5$ keV. Since this is close to the broad resonance at $E_{\text{CMS}} = 421$ keV, the peak shape could be dominated by the shape of the resonance. Solely with this information at hand, it is hard to accurately determine a correction factor for the accelerator voltage. Though, since the maximum of the observed peak is even below $E_{\gamma,\text{R}} = 2364.5$ keV, the energy a γ from the resonance would have, it can be safely assumed, that the real accelerator voltage is lower than the set one.

Additionally, the implantation of helium into the targets worked and the water cooled targets withstood the irradiation. Target FL1 lost $\approx 50\%$ of its helium content after one and a half days of irradiation with 2.2 C (not secondary electron suppressed) $^{12}\text{C}^{2+}$ and FL5 36% after two days with 6.3 C (not secondary electron suppressed) $^{12}\text{C}^{3+}$.

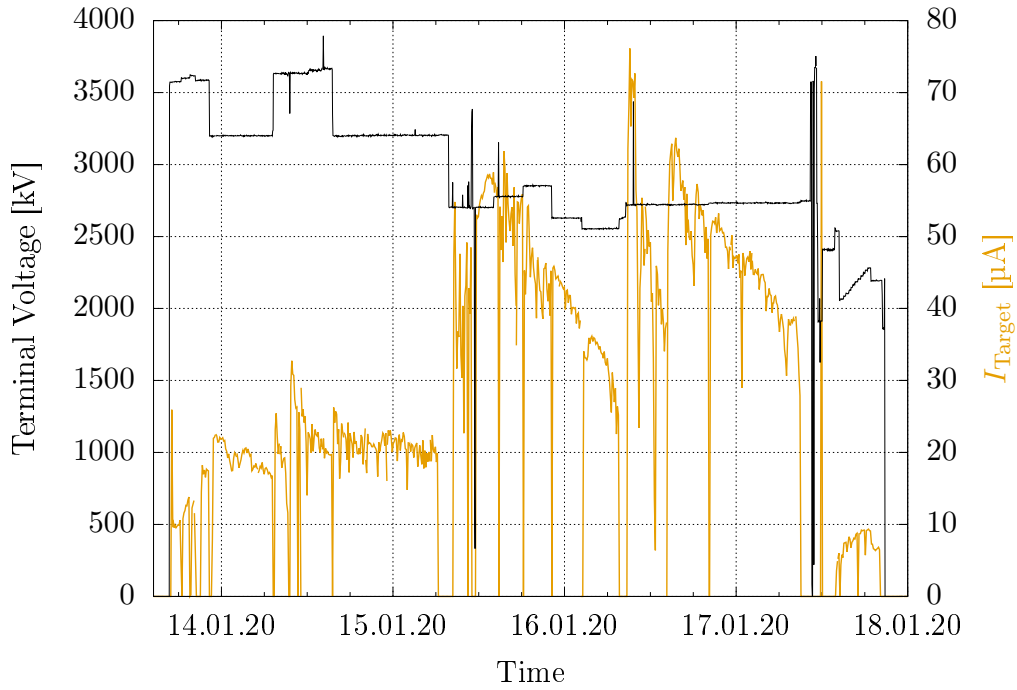


Figure 5.2.7: Accelerator voltage and target current throughout the beam time. The target current was not suppressed for secondary electrons and denotes the $^{12}\text{C}^{2+}$ current on target until the 15th January 7am and $^{12}\text{C}^{3+}$ afterwards.

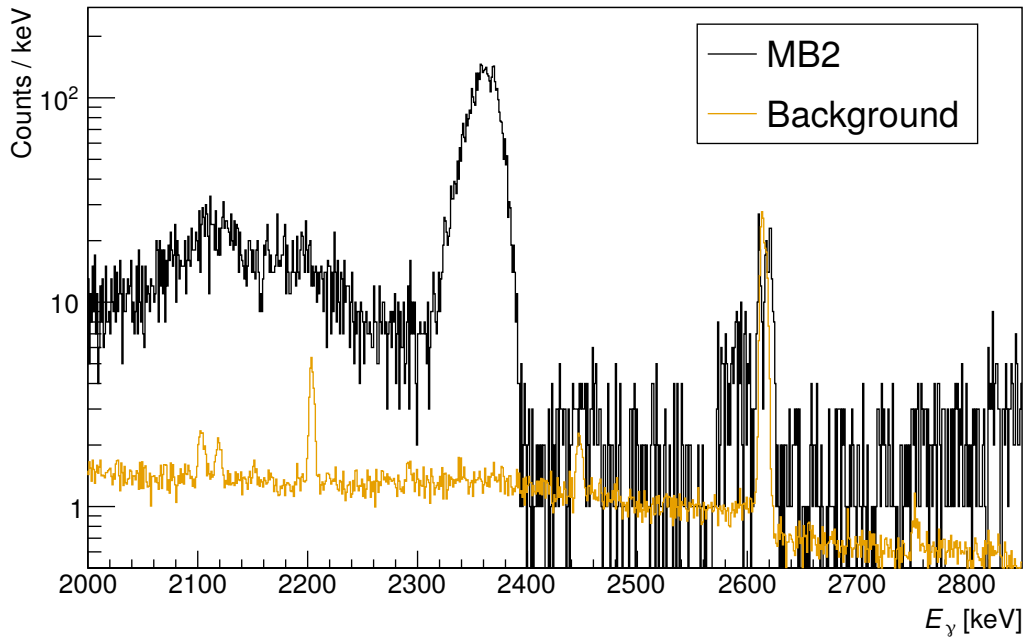


Figure 5.2.8: Anti-Compton suppressed addback spectrum for MB2 for the $^{12}\text{C}(p,\gamma)$ reaction. The beam energy was 5.86 MeV. A clear peak is visible at 2360 keV. A background run scaled to the measurement time is shown in orange.

5.2.8 Runs on the E1 resonance

The E1 resonance is a broad resonance with the peak at $E_{\text{CMS}} = 2.35$ MeV, according to the deBoer *et al.* fit [deB+17]. Therefore, a laboratory energy of 9.4 MeV ^{12}C is necessary to hit it. Due to the lack of an energy calibration of the accelerator and the energy loss of the beam inside the target, a higher beam energy of $E_{\text{Lab}} = 9.66$ MeV was used, that corresponds to $E_{\text{CMS}} = 2.45$ MeV, where the resonance is inside the target. For this calculation the read-back value of the terminal voltage was taken. The Hall probe at the HE magnet read 0.42876 T, which suggests a lower beam energy than set.

At this energy eleven runs with target FL1 took place for a total of 21 h with a $^{12}\text{C}^{2+}$ beam. With not secondary electron suppressed currents ranging from 10 to 25 μA , 1.33 C were shot onto the target. The spectra in fig. 5.2.9 show the Compton-suppressed addbacks of the two Miniball detectors.

The full-energy peak is expected at $E_{\gamma} = 9.61$ MeV in MB2 and 9.82 MeV in MB1 for $E_{\text{CMS}} = 2.45$ MeV. Every peak in this spectrum is visible in the spectrum on the E2 resonance as well (see fig. 5.2.5), so that it is unlikely, that one was caused by the $^{12}\text{C}(\alpha,\gamma)^{16}\text{O}$ reaction.

5.2.9 Runs on the E2 resonance

For the E2 resonance at 2.68 MeV first a resonance scan was attempted with the target FL2 and $^{12}\text{C}^{2+}$. Each run took ≈ 30 min with energy steps of 13 keV in the centre-of-mass system, starting at 2.7 MeV. After no signal could be observed the measurement time per energy was increased to ≈ 2 h for the three energies 2.742 MeV, 2.753 MeV and 2.763 MeV. Here, no clear signal could be observed either.

After this the target was exchanged with FL5 and the ^{12}C charge state increased to 3+, so that a lower and therefore more stable accelerator voltage could be used. The target was irradiated at five energies from 2.65 MeV to 2.875 MeV for ≈ 4 h for each run. Still no clear signal could be seen. A preliminary yield-analysis on the addback spectra, where the counts in the region of interest from 9975 keV to 10175 keV were compared, showed a peak in the yield-curve at 2.75 MeV. However, since the current information was not electron-suppressed as mentioned before, this analysis is subject to large uncertainties.

Therefore, the energy was set to 2.747 MeV for a long run spanning 25 h with the Hall probe at the HE magnet reading 0.41954 T. Here, the unsuppressed beam currents ranged from 35 to 50 μA of $^{12}\text{C}^{3+}$ and the charge was 3.7 C. The spectrum for both detectors is shown in fig. 5.2.10. For MB2 there is a peak visible at the expected energy. Unfortunately, it is exactly at the energy, where there was a background peak in the E1 runs. Since MB1 also has a peak at the same energy in these, it is likely, that beam-induced background is the cause of this signal. A small structure right next to the background peak in MB1 is visible at the expected gamma energy. For beam time reasons no run on a tantalum plate without implanted helium

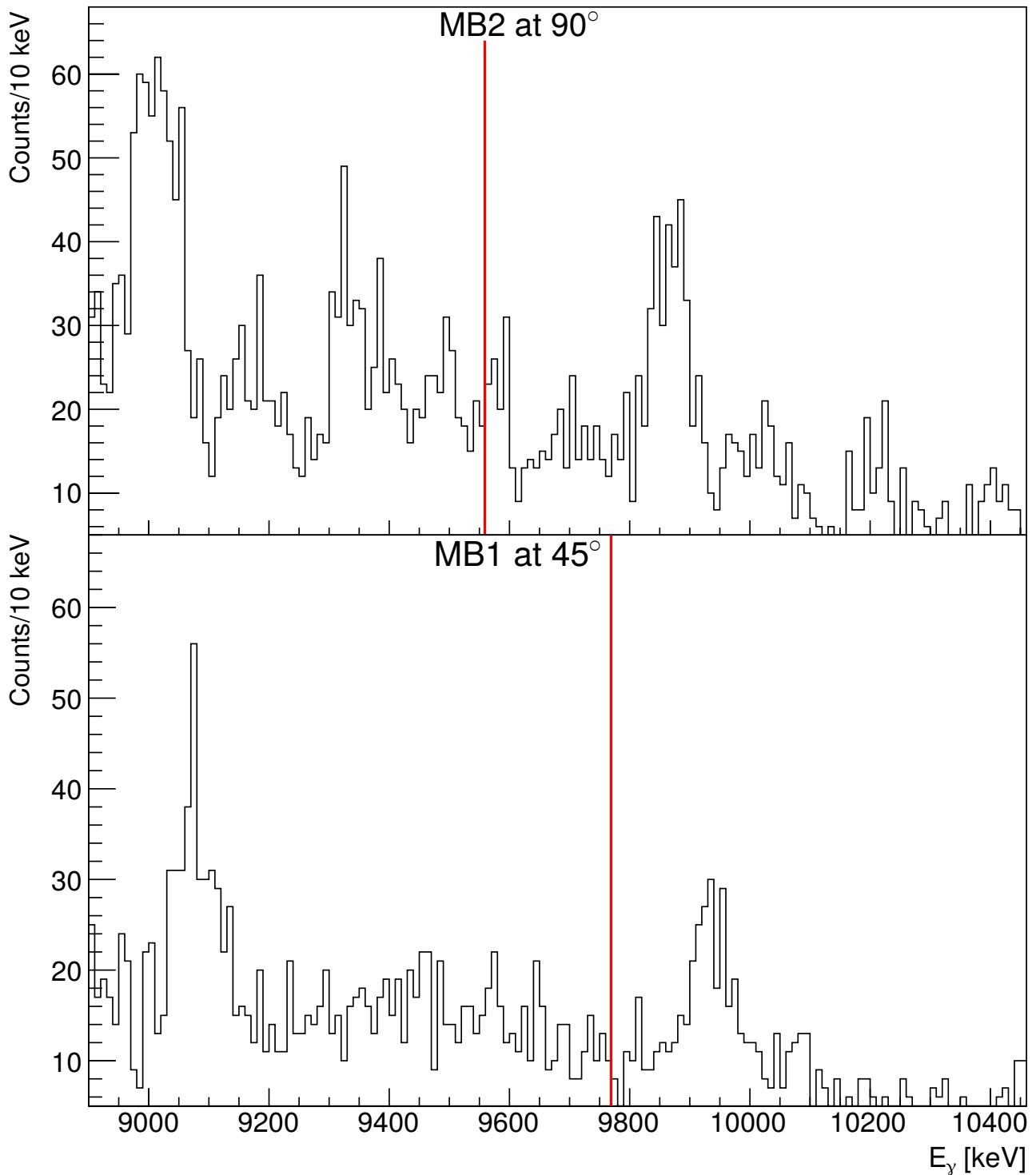


Figure 5.2.9: Compton-suppressed sum of the spectra of the single crystals at $E_{\text{CMS}} \approx 2.45$ MeV for MB1 at 45° and MB2 at 90° . Red lines are the expected gamma energy. No clear signal from the reaction is visible.

could be done in this first test. Hence, it is unclear, if this small structure can be attributed to $^{12}\text{C}(\alpha,\gamma)^{16}\text{O}$. Since the same structure of a large peak, followed by a smaller one is visible at 90° , another background peak is more likely. ^{24}Mg has several de-excitation gammas at higher excitation energies, that could attribute to this peak.

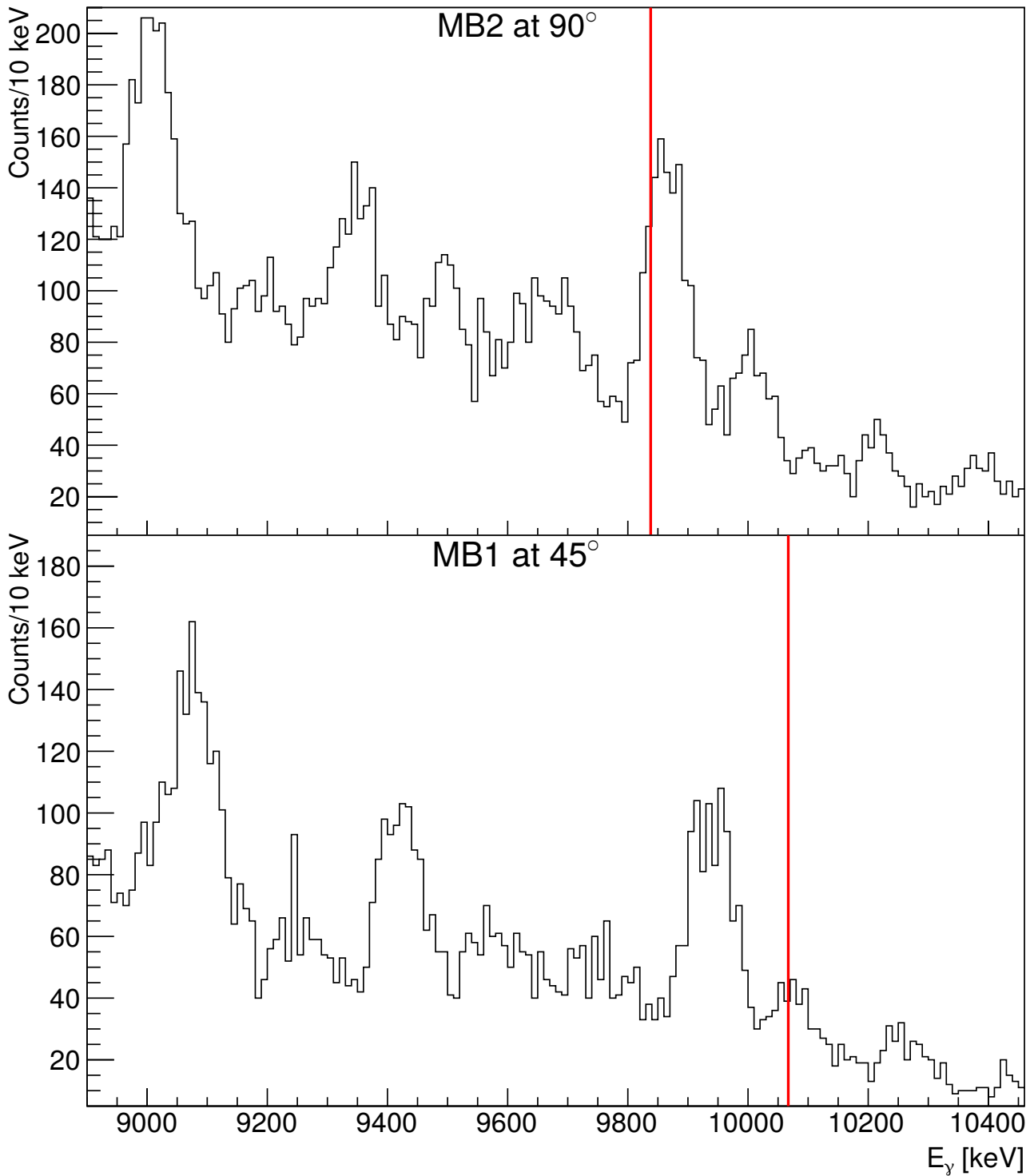


Figure 5.2.10: Compton-suppressed sum of the spectra of the single crystals at $E_{\text{CMS}} = 2.68$ MeV for MB1 at 45° and MB2 at 90° . Red lines are the expected gamma energy. In MB1 a small peak is visible, while MB2 shows a large peak, that is attributed to in-beam background.

5.3 Preparations for a future irradiation

Some improvements for a future irradiation were already undertaken as part of this thesis. A major problem was the beam alignment in the high-energy beamline. As already described in subsec. 4.2.2, this could be improved by placing a magnetic x -steerer consisting of two copper coils 1.74 m after the exit of the accelerator. Currents of less than 1 A through the magnet coils proved enough to bend the beam back to the centre and to reduce the spread of different charge states significantly.

In order to avoid beam current on the copper tube of the cold trap, which will be negatively biased for the electron suppression, several collimators with different opening diameters were produced and tested. 10 mm and 7 mm proved to be too large, since current could still be measured on the tube. However, the beam, with improved alignment, could be focused completely through it with only negligible current on the collimator of below $0.5\ \mu\text{A}$ through the opening. After some tests with smaller collimators of 3 mm and 4 mm diameter, a permanent magnet (see fig. 5.3.1) was installed together with the 10 mm collimator, which eliminated the current on the copper tube.

The limiting factor on the beam current was the stability of the accelerator voltage (see subsec. 4.1.2). In order to fix this problem, a recalibration of the Terminal Potential Stabilizer following the manual by NEC [Cor09b] was attempted. Afterwards the stability was tested at an accelerator voltage of 2.7 MV, where a helium beam was extracted from the internal ion source. Fig. 5.3.2 shows the results of these measurements. The stability could be improved a lot and is now comparable to the value of $< 1\ \text{kV}$ at 5 MV, that is given by NEC for this accelerator type [Cor98].

For the future irradiation new targets were prepared at the Ion Beam Centre at Helmholtz-Zentrum Dresden-Rossendorf. This time, the aimed for target thickness was increased by a factor of 4 to $2 \times 10^{18}\ \text{at}/\text{cm}^2$. With more helium present in the target and the increased thickness, the probability of hitting the sharp E2 resonance increases, even without a precise knowledge of the beam energy.

For the future, several modifications have been developed here. Instead of the Y-shaped target chamber, one with the endcap at a 55° angle could be used, see fig. 5.3.3, which was simulated in the previous section. Therefore, the detector, a Septuple Cluster instead of the Triple

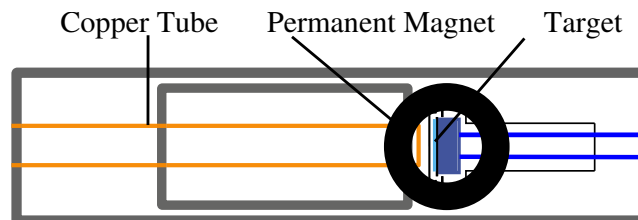


Figure 5.3.1: Schematic top view of the Y-shaped target chamber. The permanent magnet on top of the target reduces beam current on the copper tube.

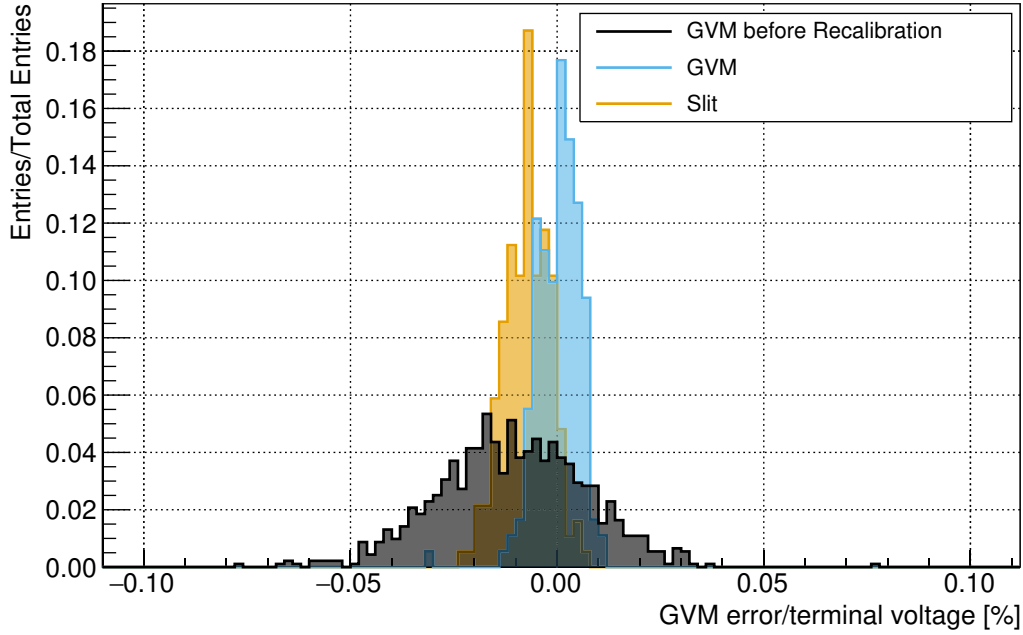


Figure 5.3.2: Terminal stability before and after recalibration. Both slit and GVM mode stability improved a lot after the recalibration.

Cluster, can be positioned much closer to the target at this angle. This increases the efficiency by a factor of about 2, if only the three central crystals of the Septuple Cluster are used. With all crystals it would be a factor of about 4, but here a Doppler correction would be necessary. A second detector shall be placed at 90° with respect to the beamline. If a satisfying signal of the E2 resonance can be picked up, a switch to the E1 resonance is possible. Furthermore beam-induced background can be investigated in more detail, due to the different Doppler shifts in the two detectors. Background peaks are less shifted, due to the higher masses of the compound nuclei.

Additionally, runs without a helium implanted target on just the tantalum backing and an energy calibration of the detectors with $^{27}\text{Al}(p,\gamma)$ are advised for this future irradiation in order to get a better understanding on beam-induced background and the expected energy of the gamma of $^{12}\text{C}(\alpha,\gamma)$.

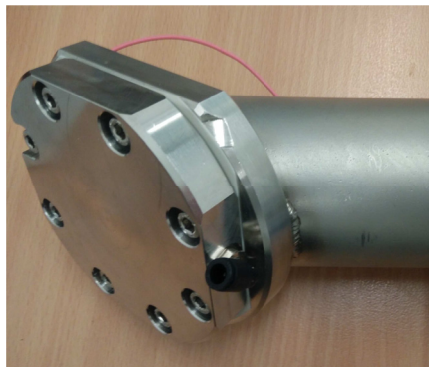


Figure 5.3.3: Photo of the 55° target chamber.

6 Summary and Outlook

$^{12}\text{C}(\alpha,\gamma)^{16}\text{O}$ has puzzled researchers for decades. Because of its low cross section in the order of nb in the astrophysically important range, no experiment to date could reach down to these low energies. While no signal of the reaction could be observed in this thesis, the foundations for future experiments with the Felsenkeller accelerator were laid down. With that, data points for this reaction at low energies could be provided in principle in coming experiments.

Muons, the main background components of low statistics experiments in shallow-underground laboratories, were investigated in the first part of the thesis. Measurements were done at four locations in the tunnels VIII and IX, four locations in tunnel IV and in the underground laboratory CAVE in Monaco. At position 3 in Felsenkeller the measured data were compared to a calculation of the muon intensity and two simulations, all of which showed good agreement. In the shallow-underground laboratory Felsenkeller, the muon intensity is suppressed by a factor of 30 to 40 compared to the surface.

This step was crucial in order to understand the background in the HPGe detectors. Based on these measurements, an active muon veto could be designed for the low-activity γ -counting setup in Felsenkeller.

After the muon measurements were taken, construction of the laboratory inside the tunnels took place. The impact of these can be approximated in a conservative approach to be below 2%.

The external ion source was put into operation, first on a test stand at the HZDR campus, later on in the new Felsenkeller laboratory. The source parameters were improved for high $^{12}\text{C}^-$ current and up to $172\mu\text{A}$ could be measured at the Faraday cup in front of the accelerator. Stable operation of the source yielded around $100\mu\text{A}$ for six hours.

The design of the sample holders of the ion source was investigated: a 2 mm core drilling in a aluminium sample holder yielded the best results. The copper holders had longer burn-in times, but achieved higher currents afterwards, which is less suited for experiments.

An analysis of the extracted ions showed mono-atomic carbon, molecules of carbon and caesium with carbon. Contaminations of hydrogen, possibly oxygen and the sample holder materials aluminium and copper could be observed in the beam as well.

After that, the accelerator was brought to high voltage. During the conditioning process several discharges of the high-voltage could be observed. Starting at 4 MV these became so frequent, that the voltage could not be increased further.

However, at lower terminal voltages stable operation with beam transmission was possible. With high injected beam currents or high voltages above 3 MV, the stability decreased and deviations of the desired voltage increased to $\sigma = 0.13\%$ for $40\mu\text{A}$ of $^{12}\text{C}^-$ transmitted at 2 MV terminal voltage, compared to 0.03% without beam. The Terminal Potential Stabilizer was already recalibrated for the GVM and slit mode, which resulted in an improvement of the terminal stability. This is now comparable to the value in the data sheet of the accelerator. The new calibration was tested with a helium beam from the internal source. The positive results shall be verified with a carbon beam from the external ion source in the future.

With a restricted beam of 2 mm width in x -direction the influence of different stripper pressures at various terminal voltages for the charge state distribution was investigated. The results were comparable to the literature and optimal parameters for experiments with carbon beam were developed. Furthermore, these measurements yielded insights into transmission through the accelerator and the high-energy beamline, where 90% could be reached for a terminal voltage of 2.5 MV, while for low terminal voltages it went down to a minimum of 30%. Most of the beam loss seems to happen in the high-energy beamline. Steps to improve this have been undertaken by installing additional steerers, though the improvement still needs to be verified by repeating these transmission measurements.

Another result of these measurements was, that the 2+ charge state of ^{12}C gives the highest particle beam currents at the Faraday cup after the high-energy magnet. Up to 35% of the ions shot into the accelerator reached FC4 in this charge state. Only at the highest measured beam energy of 9.9 MeV, $^{12}\text{C}^{3+}$ is better suited for experiments with 47% transmitted ions compared to the 30% of the 2+ charge state.

An energy calibration of the accelerator could not be done in the scope of this thesis, since the internal source providing a hydrogen beam, was not working. This is of utmost importance for future experiments and should be done as soon as possible.

Further, one Triple and one Septuple Cluster were simulated in GEANT4. The simulation showed good agreement to measurements with radioactive calibration sources with deviations of below 10%. Only crystal B of the Septuple Cluster could not be verified in the low-energy region. Therefore, for the Septuple Cluster only the single crystal spectra were analysed, not the addback spectra. The simulated setup with the 55° target chamber resulted in good agreement with the Triple Cluster, while for the Septuple Cluster deviations were quite large for the outer crystals due to the close geometry of the detector. The simulation was then used to determine the efficiency of the detectors for gammas of the $^{12}\text{C}(\alpha,\gamma)^{16}\text{O}$ reaction and the effect of the angular distribution and the Doppler shift.

In the future, simulations and measurements of the addback spectrum of the Septuple Cluster, as well as the second Triple and Septuple Cluster need to be conducted. A measurement with the Septuple Cluster in a larger distance to the target could rule out, that a misplacement in the experiment is the source of the deviations to the simulation. Furthermore, the Y-shaped

target chamber, that was used during the first test measurement, needs to be verified as well. A first test with a carbon beam on helium-implanted tantalum targets was conducted. Two energies, where one covers a broad E1 and the other a narrow E2 resonance, were investigated. No clear signal of $^{12}\text{C}(\alpha,\gamma)^{16}\text{O}$ could be observed. But the operation of the facility worked well and beam could be shot onto the target. Problems, like the low beam current, could be identified and steps to improve these were already undertaken, by improving the beam alignment and the terminal stability. One was to install additional x -steerer at the beginning of the HE beamline, that improved the x -alignment of the beam in a way, that it was centred on both BPMs after the HE magnet.

The used targets were contaminated with carbon and oxygen, which led to beam-induced background in the region of interest. For a future irradiation, implanted targets with higher helium areal density were prepared. It remains to be seen, if these will show the same contaminations and whether the areal density remains constant in the targets.

All these before mentioned steps had the aim to improve the signal of the reaction in the detectors. With the muon measurements, the source of the background could be better understood and the placement of muon-vetos is possible. The improvements of the external ion source, the terminal stability and the transmission through the accelerator and the beamline were aiming for improved carbon beam intensity on the target, which will lead to higher statistics in future experiments. The first test irradiation has proven the capability of the facility to run 24 h a day and identified remaining problems. Some of these could be resolved in the scope of the thesis, while for others recommendations were developed.

With that, the way for future experiments with carbon beam is paved. For this a gas-jet and an extended gas target shall be installed to further investigate the $^{12}\text{C}(\alpha,\gamma)^{16}\text{O}$ reaction. With the first one, measurements down to $E_{\text{CMS}} = 1$ MeV are planned, expecting results on both the E1 and E2 component. The extended gas target shall be surrounded by a BGO detector, enabling investigation of the total cross section of the reaction down to 0.6 MeV. It is stressed, that these measurements have the potential to improve our understanding of this process happening during the helium burning in stars and with this extend the knowledge on nucleosynthesis in the universe.

Danksagung

Allen voran gilt mein Dank Daniel und Kai, die es mir überhaupt erst ermöglicht haben, meine Doktorarbeit anzufertigen.

Weiterhin möchte ich mich bei allen bedanken, die mich bei der Inbetriebnahme des Beschleunigers und nachfolgend beim Aufbau und der Durchführung des Experiments unterstützt haben:

Unsere Techniker Maik, Toralf und Bernd, die sich um die Ausrichtung und den Aufbau des Beschleunigers gekümmert haben.

Maik, der zusätzlich die Steuerung des Beschleunigers geschrieben hat und sämtliche Probleme mit dieser zeitnah gelöst hat.

Tamás, der mich bei der Inbetriebnahme des Beschleunigers tatkräftig unterstützt hat und mir viele Fragen beantworten konnte.

Steffen, der sich super um die Detektoren gekümmert hat und mir auch sonst bei sämtlichen anderen Problemen mit Rat und Tat zur Seite stand.

Julia und Tommy, die mich im Rahmen ihrer Bachelorarbeiten hilfreich bei der Bedienung der Ionenquelle im Felsenkeller und des Beschleunigers unterstützt haben.

Andreas für die Hilfe beim Aufbau der Detektoren und bei Vakuump Problemen.

Allen, die sich bereit erklärt haben Schichten während der Strahlzeit zu übernehmen: Conrad, Jonas, Konrad, Max, Roland, Simon, Steffen, Thomas, Tommy, Franziska und Marcel.

Shavkat möchte ich danken für seine Unterstützung bei der Inbetriebnahme der Sputterquelle und des Beschleunigers.

Weiterhin gilt mein Dank den Kollegen am Ionenstrahlzentrum für die Herstellung der Heliumtargets.

Schlussendlich möchte ich noch meinen Freunden und Kollegen am HZDR und am IKTP danken, die mir die ganze Zeit über mit Rat und Tat zur Seite standen: Steffen, Andi, Conrad, Heinrich, Simon und Sebastian.

A Appendix

A.1 List of abbreviations

- BGO** Bismuth germanium oxide
- BPM** Beam profile monitor
- CAVE** Counting laboratory for environmental radionuclides
- CMS** centre-of-mass system
- CPO** Capacitor pick-off plate
- dof** Degrees of freedom
- EB** Euroball
- EL** Einzel lens
- ERDA** Elastic recoil detection analysis
- ESA** Electrostatic analyzer
- FC** Faraday cup
- GDML** Geometry description markup language
- GVM** Generating voltmeter
- HE** high-energy
- HPGe** High-purity germanium
- HZDR** Helmholtz-Zentrum Dresden-Rossendorf
- IAEA** International Atomic Energy Agency
- m.a.s.l.** Metres above sea level
- LE** low-energy

MB Miniball

MC-SNICS multi-cathode source of negative ions by caesium sputtering

MK Messkammer

MQ Magnetic quadrupole

m.w.e. Metres water equivalent

NEC National Electrostatics Corporation

REGARD RMKI-ELTE collaboration on gaseous detector, research and development

ROI Region of interest

SES Secondary electron suppression

SLS Slit system

SRIM Stopping and range of ions in matter

WS Workshop

XS Horizontal steerer

YS Vertical steerer

A.2 Stripper charge distribution

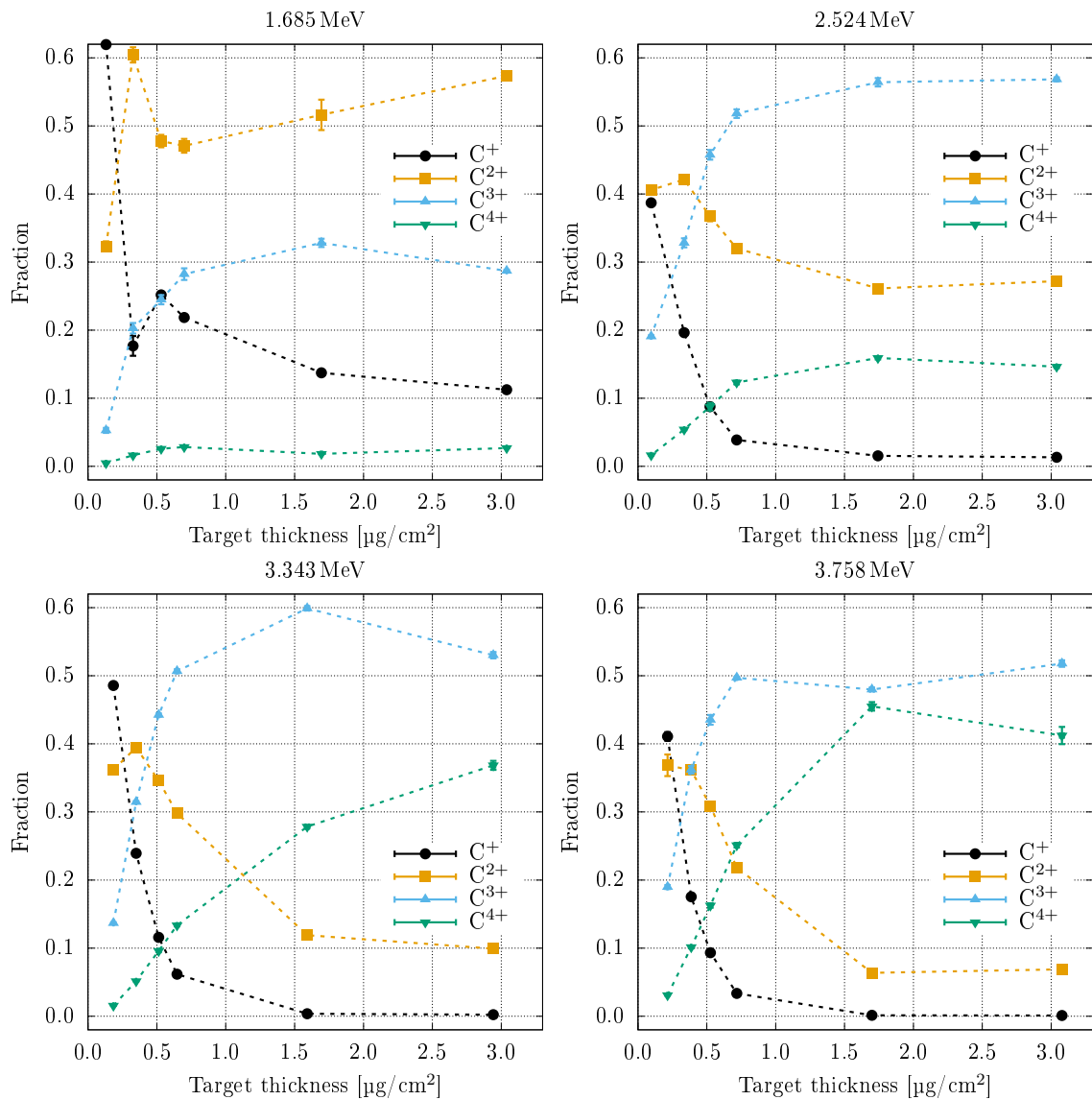


Figure A.2.1: Charge fractions for different stripper pressures at various beam energies for the Felsenkeller accelerator. For 1.685 MeV the quadrupole was not adapted for each charge state by mistake for target thicknesses below $1 \mu\text{g}/\text{cm}^2$, so that the real distribution might differ from the measured one.

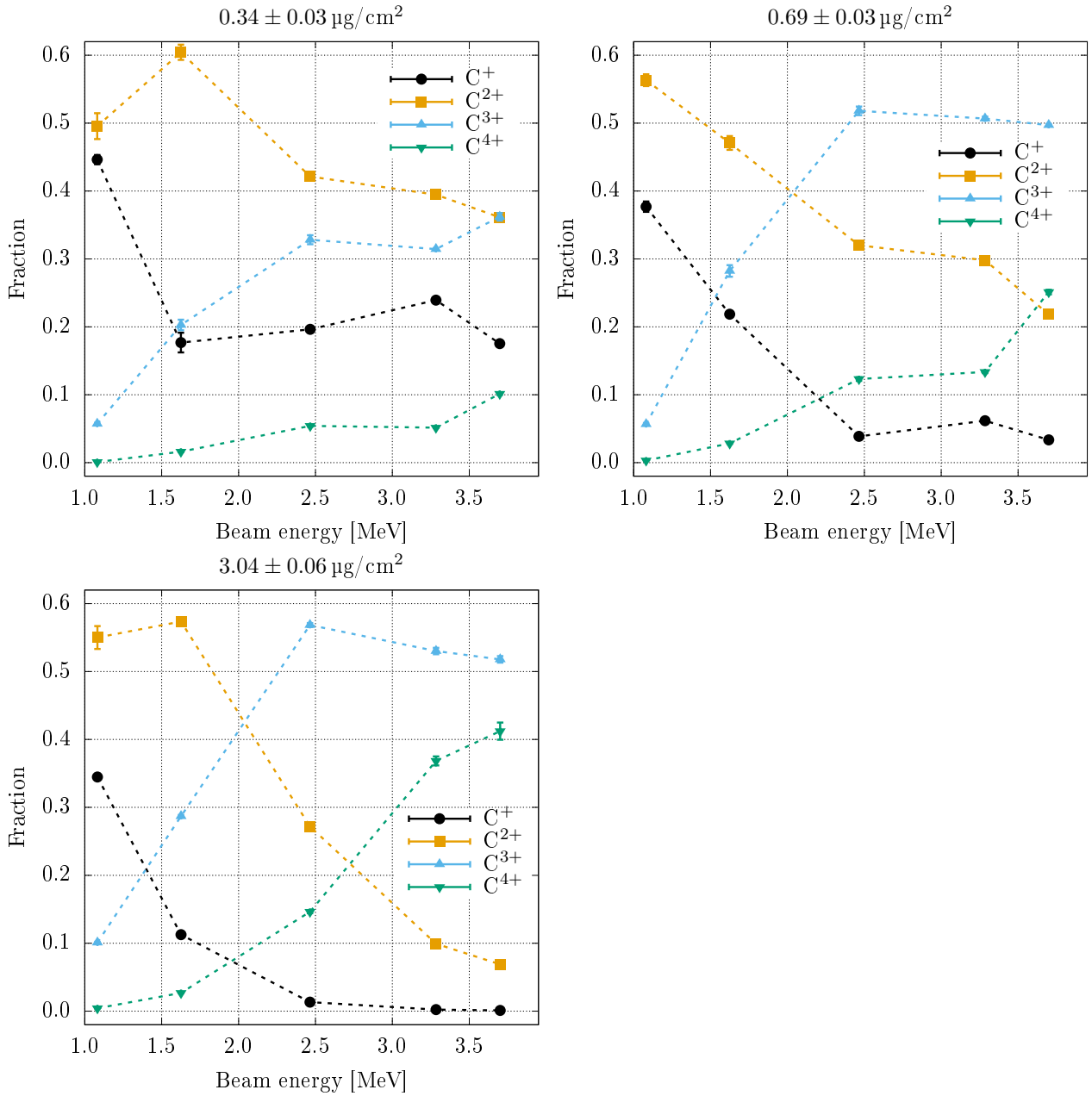


Figure A.2.2: Charge fractions for different beam energies at various stripper gas areal densities for the Felsenkeller accelerator. For the data points at 1.685 MeV the quadrupole was not adapted for each charge state by mistake in the upper plots, so that the real distribution might differ from the measured one.

A.3 Simulation results

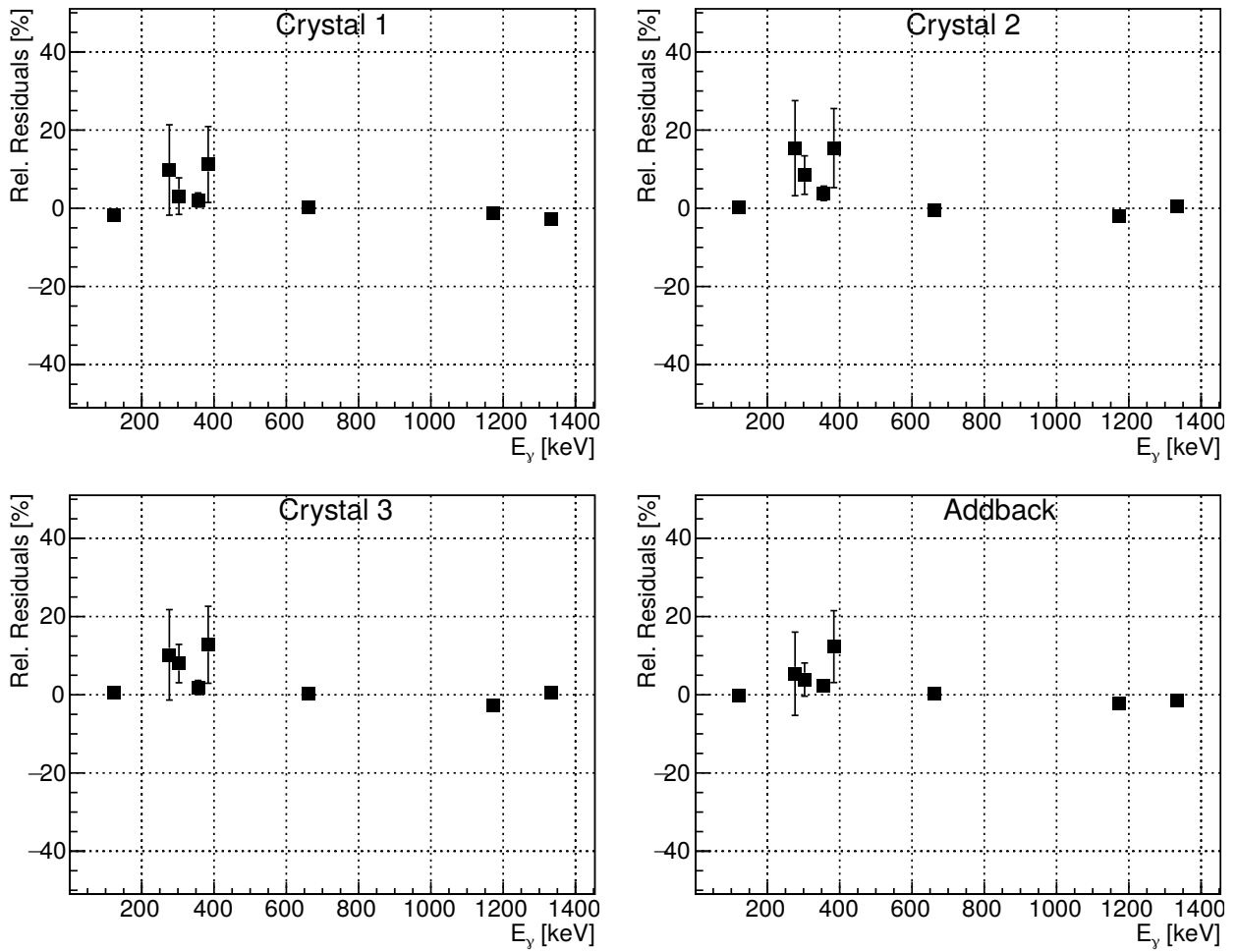


Figure A.3.1: Residuals of the efficiency simulation compared to the measurement for Triple Cluster MB1 without target chamber.

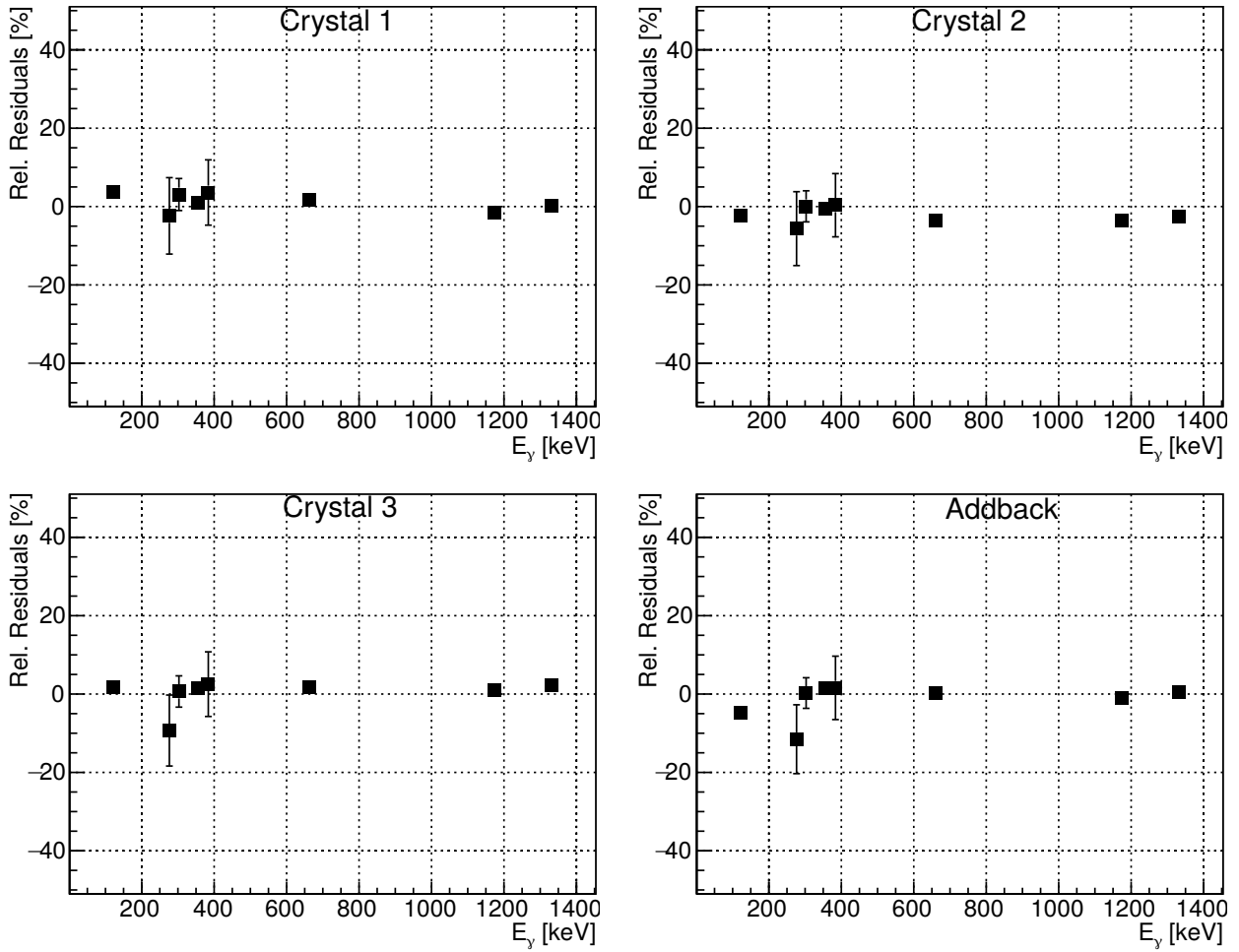


Figure A.3.2: Residuals of the efficiency simulation compared to the measurement for Triple Cluster MB1 with the 55° target chamber.

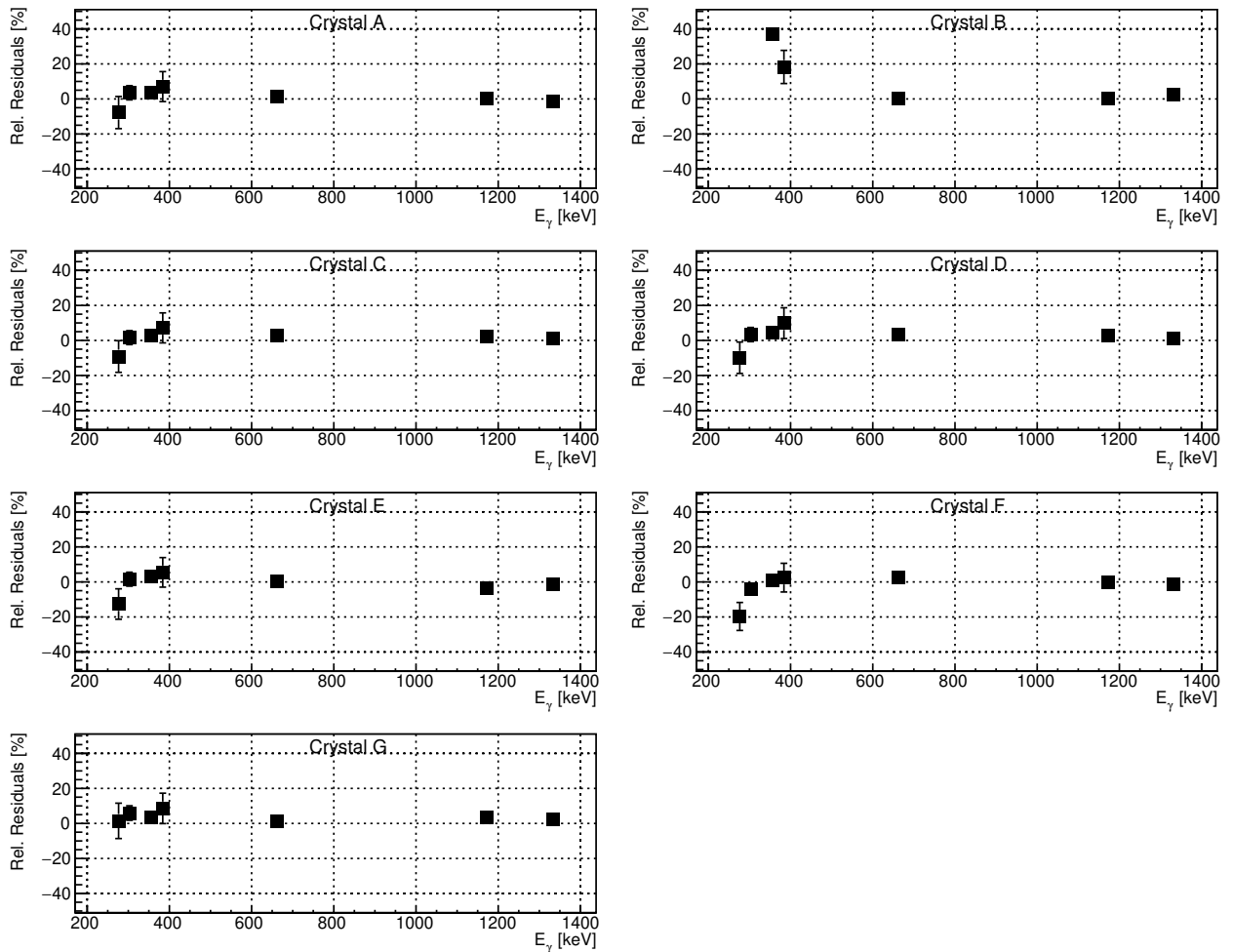


Figure A.3.3: Residuals of the efficiency simulation compared to the measurement for Septuple Cluster EB17 without target chamber.

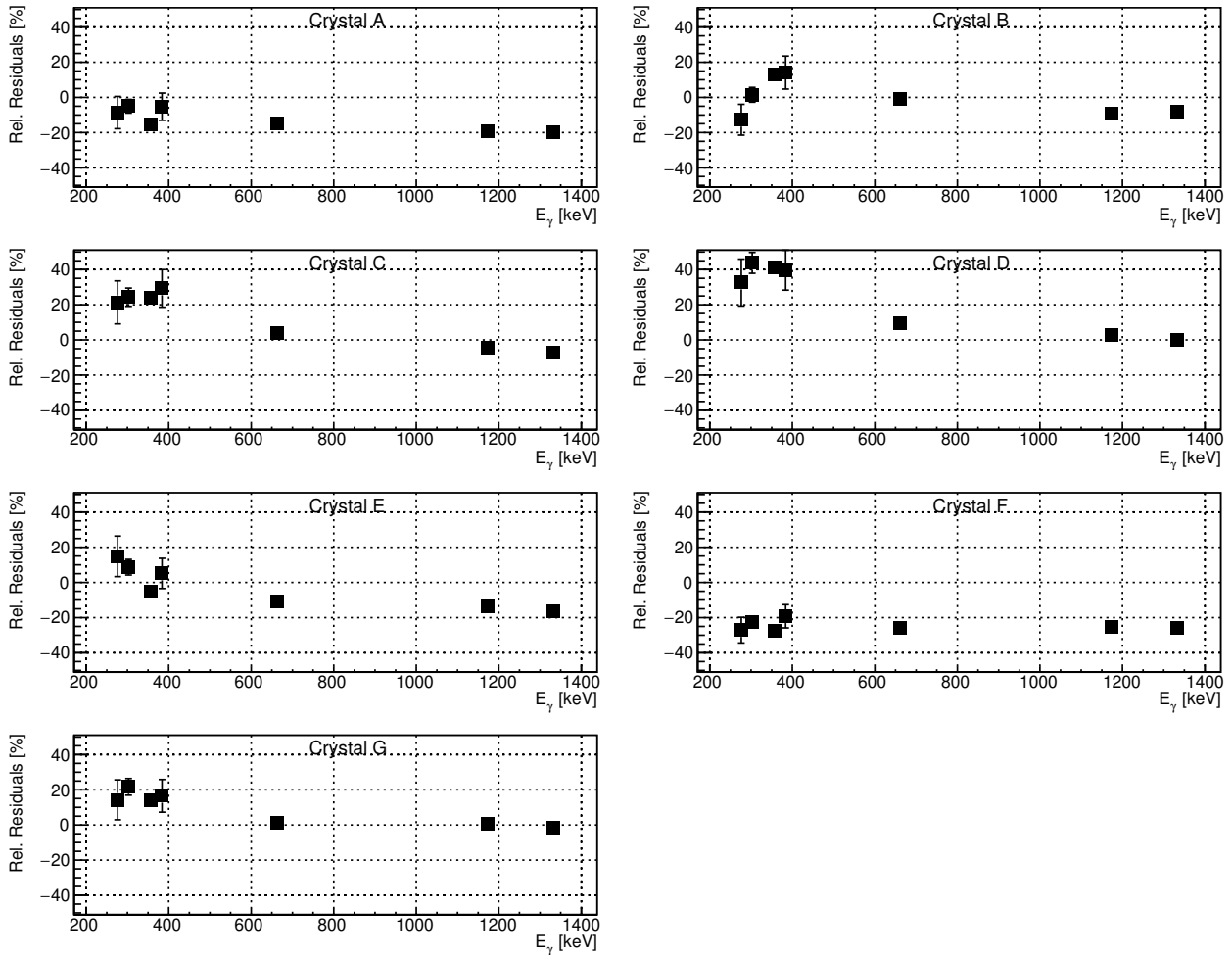


Figure A.3.4: Residuals of the efficiency simulation compared to the measurement for Septuple Cluster EB17 with the 55° target chamber.

Bibliography

- [Ada+10] P. Adamson et al. “Observation of muon intensity variations by season with the MINOS far detector”. In: *Phys. Rev. D* 81 (1 Jan. 2010), p. 012001. DOI: 10.1103/PhysRevD.81.012001.
- [Agu+06] E. F. Aguilera et al. “New γ -ray measurements for $^{12}\text{C}+^{12}\text{C}$ sub-Coulomb fusion: Toward data unification”. In: *Phys. Rev. C* 73 (6 June 2006), p. 064601. DOI: 10.1103/PhysRevC.73.064601.
- [AJP84] T. Aitken, T. Joy, and H. Price. “Initial operating experience with beams at the Daresbury tandem”. In: *Nuclear Instruments and Methods in Physics Research* 220.1 (1984), pp. 149–153. DOI: 10.1016/0167-5087(84)90426-5.
- [An+15] Z.-D. An et al. “Astrophysical S factor of the $^{12}\text{C}(\alpha,\gamma)^{16}\text{O}$ reaction calculated with reduced R -matrix theory”. In: *Phys. Rev. C* 92 (4 Oct. 2015), p. 045802. DOI: 10.1103/PhysRevC.92.045802.
- [An+18] F. An et al. “Seasonal variation of the underground cosmic muon flux observed at Daya Bay”. In: *Journal of Cosmology and Astroparticle Physics* 2018.01 (Jan. 2018), pp. 001–001. DOI: 10.1088/1475-7516/2018/01/001.
- [AS55] H. R. Allan and N. Sarma. “A Search for Capture Processes in Alpha-Particle and Deuteron Bombardments”. In: *Proceedings of the Physical Society. Section A* 68.6 (June 1955), pp. 535–538. DOI: 10.1088/0370-1298/68/6/410.
- [Ass+06] M. Assunção et al. “ $E1$ and $E2$ S factors of $^{12}\text{C}(\alpha,\gamma_0)^{16}\text{O}$ from γ -ray angular distributions with a 4 π -detector array”. In: *Phys. Rev. C* 73 (5 May 2006), p. 055801. DOI: 10.1103/PhysRevC.73.055801.
- [Bar+12] Barnaföldi et al. “Portable cosmic muon telescope for environmental applications”. In: *Nuclear Instruments and Methods in Physics Research Section A: Accelerators, Spectrometers, Detectors and Associated Equipment* 689 (2012), pp. 60–69. DOI: 10.1016/j.nima.2012.06.015.
- [BB06] L. Buchmann and C. Barnes. “Nuclear reactions in stellar helium burning and later hydrostatic burning stages”. In: *Nuclear Physics A* (2006). Special Issue on Nuclear Astrophysics, pp. 254–290. DOI: 10.1016/j.nuclphysa.2005.01.005.

- [Ber+05] M. Berger et al. *ESTAR, PSTAR, and ASTAR: Computer Programs for Calculating Stopping-Power and Range Tables for Electrons, Protons, and Helium Ions (version 1.2.3)*. [Online; accessed 25-November-2020]. 2005. URL: <https://physics.nist.gov/PhysRefData/Star/Text/ESTAR.html>.
- [Ber+10] M. Berger et al. *XCOM: Photon Cross Section Database (version 1.5)*. [Online; accessed 25-November-2020]. 2010. URL: <http://physics.nist.gov/xcom>.
- [Bet72] H.-D. Betz. “Charge States and Charge-Changing Cross Sections of Fast Heavy Ions Penetrating Through Gaseous and Solid Media”. In: *Rev. Mod. Phys.* 44 (3 July 1972), pp. 465–539. DOI: 10.1103/RevModPhys.44.465.
- [BR83] A. I. Barbouti and B. C. Rastin. “A study of the absolute intensity of muons at sea level and under various thicknesses of absorber”. In: *Journal of Physics G: Nuclear Physics* 9.12 (1983), p. 1577.
- [Bro+73] Brochard, F. et al. “Étude des désexcitations électromagnétiques des niveaux 1- situés à 12,44 et 13,09 MeV dans le noyau ^{16}O ”. In: *J. Phys. France* 34.5-6 (1973), pp. 363–367. DOI: 10.1051/jphys:01973003405-6036300.
- [BS13] C. R. Brune and D. B. Sayre. “Energy deconvolution of cross-section measurements with an application to the $^{12}\text{C}(\alpha,\gamma)^{16}\text{O}$ reaction”. In: *Nuclear Instruments and Methods in Physics Research Section A: Accelerators, Spectrometers, Detectors and Associated Equipment* 698 (2013), pp. 49–59. DOI: 10.1016/j.nima.2012.09.023.
- [BTW57] S. D. Bloom, B. J. Toppel, and D. H. Wilkinson. “Isotopic spin selection rules IX: The 9.58 MeV state of ^{16}O ”. In: *The Philosophical Magazine: A Journal of Theoretical Experimental and Applied Physics* 2.13 (1957), pp. 57–60. DOI: 10.1080/14786435708231722.
- [Cas+65] C. Castagnoli et al. “Measurements on the cosmic radiation intensity in the mont blanc tunnel”. In: *Il Nuovo Cimento (1955-1965)* 35.4 (Feb. 1965), pp. 969–976. DOI: 10.1007/BF02735517.
- [Cha82] K. Chapman. “Some aids to the voltage conditioning of an electrostatic accelerator”. In: *Nuclear Instruments and Methods in Physics Research* 197.2 (1982), pp. 265–266. DOI: 10.1016/0167-5087(82)90315-5.
- [Cor09a] N. E. Corporation. *Corona probe model 5820*. 2009.
- [Cor09b] N. E. Corporation. *Terminal Potential Stabilizer Controller Model TPS6.0*. 2009.
- [Cor17] N. E. Corporation. *Multi - Cathode Source of Negative Ions by Cesium Sputtering (MC - SNICS)*. [Online; accessed 25-November-2020]. 2017. URL: <https://www.pelletron.com/wp-content/uploads/2017/02/MC-SNICS-v1.pdf>.

- [Cor98] N. E. Corporation. *15SDH-2 Data Sheet*. 1998.
- [Cos+10] H. Costantini et al. “ $^{16}\text{O}(\alpha,\gamma)^{20}\text{Ne}$ S factor: Measurements and R-matrix analysis”. In: *Physical Review C* (Sept. 2010), p. 035802. DOI: 10.1103/PhysRevC.82.035802.
- [DB74] P. Dyer and C. Barnes. “The $^{12}\text{C}(\alpha,\gamma)^{16}\text{O}$ reaction and stellar helium burning”. In: *Nuclear Physics A* 233.2 (1974), pp. 495–520. DOI: 10.1016/0375-9474(74)90470-9.
- [deB+17] R. J. deBoer et al. “The $^{12}(\alpha,\gamma)^{16}\text{O}$ reaction and its implications for stellar helium burning”. In: *Rev. Mod. Phys.* 89 (3 Sept. 2017), p. 035007. DOI: 10.1103/RevModPhys.89.035007.
- [Ebe+92] J. Eberth et al. “Development of a composite Ge detector for EUROBALL”. In: *Progress in Particle and Nuclear Physics* 28 (1992), pp. 495–504. DOI: 10.1016/0146-6410(92)90051-3.
- [Fan+17] X. Fang et al. “Experimental measurement of $^{12}\text{C}+^{16}\text{O}$ fusion at stellar energies”. In: *Phys. Rev. C* (4 Oct. 2017), p. 045804. DOI: 10.1103/PhysRevC.96.045804.
- [Fey04] M. Fey. “Im Brennpunkt der Nuklearen Astrophysik: Die Reaktion $^{12}\text{C}(\alpha,\gamma)^{16}\text{O}$ ”. PhD thesis. Universität Stuttgart, 2004.
- [Fow84] W. A. Fowler. “The Quest for the Origin of the Elements”. In: *Science* 226.4677 (1984), pp. 922–935. DOI: 10.1126/science.226.4677.922.
- [Fyn+05] H. O. U. Fynbo et al. “Revised rates for the stellar triple- α process from measurement of ^{12}C nuclear resonances”. In: *Nature* 7022 (Jan. 2005), pp. 136–139. DOI: 10.1038/nature03219.
- [Gai90] T. Gaisser. *Cosmic Rays and Particle Physics*. Cambridge University Press, 1990.
- [Gia+01] L. Gialanella et al. “The E1 capture amplitude in $^{12}\text{C}(\alpha,\gamma)^{16}\text{O}$ ”. In: *The European Physical Journal A - Hadrons and Nuclei* 11.3 (2001), pp. 357–370. DOI: 10.1007/s100500170075.
- [GMS01] D. E. Groom, N. V. Mokhov, and S. I. Striganov. “Muon stopping power and range tables 10-MeV to 100-TeV”. In: *Atom. Data Nucl. Data Tabl.* 78 (2001), pp. 183–356. DOI: 10.1006/adnd.2001.0861.
- [Gri+20] M. Grieger et al. “Neutron flux and spectrum in the Dresden Felsenkeller underground facility studied by moderated ^3He counters”. In: *Phys. Rev. D* 101 (12 June 2020), p. 123027. DOI: 10.1103/PhysRevD.101.123027.
- [Gri01] P. K. F. Grieder. *Cosmic rays at earth: researcher’s reference manual and data book*. Amsterdam: North-Holland, 2001.

- [Ham+05a] J. Hammer et al. “E1 and E2 capture cross section and astrophysical reaction rate of the key reaction $^{12}\text{C}(\alpha,\gamma)^{16}\text{O}$ ”. In: *Nuclear Physics A* 758 (2005). Nuclei in the Cosmos VIII, pp. 363–366. DOI: 10.1016/j.nuclphysa.2005.05.066.
- [Ham+05b] J. Hammer et al. “New determination of the $^{12}\text{C}(\alpha,\gamma)^{16}\text{O}$ reaction rate from γ -ray angular distribution measurements”. In: *Nuclear Physics A* 752 (2005). Proceedings of the 22nd International Nuclear Physics Conference (Part 2), pp. 514–521. DOI: 10.1016/j.nuclphysa.2005.02.056.
- [Hor09] V. Horvat. “ERCS08: A FORTRAN program equipped with a Windows graphics user interface that calculates ECPSSR cross sections for the removal of atomic electrons”. In: *Computer Physics Communications* 180.6 (2009), pp. 995–1003. DOI: 10.1016/j.cpc.2008.12.034.
- [IAE20] IAEA. *Live Chart of Nuclides*. [Online; accessed 25-November-2020]. 2020. URL: <https://www-nds.iaea.org/relnsd/vcharthtml/VChartHTML.html>.
- [Ike+03] N. Ikeda et al. “Facilities for direct measurement of $^4\text{He}(^{12}\text{C},^{16}\text{O})\gamma$ reaction cross section at KUTL”. In: *Nuclear Physics A* 718 (2003), pp. 558–560. DOI: 10.1016/S0375-9474(03)00845-5.
- [Ili08] C. Iliadis. *Nuclear Physics of Stars*. Physics textbook. Wiley, 2008.
- [Inc] W. R. Inc. *Mathematica, Version 12.2*. Champaign, IL, 2020.
- [JGM70] R. J. Jaszczak, J. H. Gibbons, and R. L. Macklin. “ $^{12}\text{C}(\alpha,\gamma)^{16}\text{O}$ Capture Cross Section Below 3.2 MeV”. In: *Phys. Rev. C* 2 (1 July 1970), pp. 63–69. DOI: 10.1103/PhysRevC.2.63.
- [JM70] R. J. Jaszczak and R. L. Macklin. “ $^{12}\text{C}(\alpha,\gamma)^{16}\text{O}$ Capture Cross Section Below 4.1 MeV”. In: *Phys. Rev. C* 2 (6 Dec. 1970), pp. 2452–2453. DOI: 10.1103/PhysRevC.2.2452.
- [KAM94] F. Khiari, R. Abdel-Aal, and R. Muhammad. “Beam emittance reconstructions at the KFUPM 350 keV ion accelerator”. In: *Nuclear Instruments and Methods in Physics Research Section A: Accelerators, Spectrometers, Detectors and Associated Equipment* 343.2 (1994), pp. 383–389. DOI: 10.1016/0168-9002(94)90215-1.
- [Ket+82] K. U. Kettner et al. “The $^4\text{He}(^{12}\text{C},\gamma)^{16}\text{O}$ reaction at stellar energies”. In: *Zeitschrift für Physik A Atoms and Nuclei* 308.1 (1982), pp. 73–94. DOI: 10.1007/BF01415851.
- [Kii+02] M. Kiisk et al. “The charge state distribution of a carbon beam measured at the lund pelletron accelerator with the newly installed terminal pumping system in use”. In: *Nuclear Instruments and Methods in Physics Research Section A: Accelerators, Spectrometers, Detectors and Associated Equipment* 481.1 (2002), pp. 1–8. DOI: 10.1016/S0168-9002(01)01255-4.

- [Kir+12] O. S. Kirsebom et al. “Improved Limit on Direct α Decay of the Hoyle State”. In: *Phys. Rev. Lett.* (20 May 2012), p. 202501. DOI: 10.1103/PhysRevLett.108.202501.
- [KLR80] K. U. Kettner, H. Lorenz-Wirzba, and C. Rolfs. “The $^{12}\text{C} + ^{12}\text{C}$ reaction at subcoulomb energies (I)”. In: *Zeitschrift für Physik A Atoms and Nuclei* 298.1 (Mar. 1980), pp. 65–75. DOI: 10.1007/BF01416030.
- [KMV71] G. Kernel, W. Mason, and U. Von Wimmersperg. “Angular distributions from the reaction $^{12}\text{C}(\alpha,\gamma)^{16}\text{O}$ in the 13 MeV excitation region of ^{16}O ”. In: *Nuclear Physics A* 167.2 (1971), pp. 352–368. DOI: 10.1016/0375-9474(71)90081-9.
- [Kop17] M. Koppitz. “Charakterisierung der Sputter-Ionenquelle für den Felsenkellerbeschleuniger”. Bachelor’s Thesis. Dresden: Technische Universität Dresden, 2017.
- [Kre+88] R. M. Kremer et al. “Coincidence measurement of the $^{12}\text{C}(\alpha,\gamma)^{16}\text{O}$ cross section at low energies”. In: *Phys. Rev. Lett.* 60 (15 Apr. 1988), pp. 1475–1478. DOI: 10.1103/PhysRevLett.60.1475.
- [Kun+01] R. Kunz et al. “ $^{12}\text{C}(\alpha,\gamma)^{16}\text{O}$: The Key Reaction in Stellar Nucleosynthesis”. In: *Phys. Rev. Lett.* 86 (15 Apr. 2001), pp. 3244–3247. DOI: 10.1103/PhysRevLett.86.3244.
- [Kun02] R. Kunz. “ $^{12}\text{C}(\alpha,\gamma)^{16}\text{O}$ - Die Schlüsselreaktion im Heliumbrennen der Sterne”. PhD thesis. Universität Stuttgart, 2002.
- [Lam+15] E. Lamour et al. “Extension of charge-state-distribution calculations for ion-solid collisions towards low velocities and many-electron ions”. In: *Phys. Rev. A* 92 (4 Oct. 2015), p. 042703. DOI: 10.1103/PhysRevA.92.042703.
- [Li+18] G. Li et al. “Simulated characteristics of the DEGAS γ -detector array”. In: *Nuclear Instruments and Methods in Physics Research Section A: Accelerators, Spectrometers, Detectors and Associated Equipment* 890 (2018), pp. 148–154. DOI: 10.1016/j.nima.2018.02.062.
- [Liu16] W. P. Liu. “Underground Nuclear Astrophysics Experiment JUNA in China”. In: *Proceedings of the 14th International Symposium on Nuclei in the Cosmos (NIC2016)*. 2016. DOI: 10.7566/JPSCP.14.011101.
- [Lob+12] N. Lobanov et al. “Terminal voltage stabilization of pelletron tandem accelerator”. In: *Proceedings of Heavy Ion Accelerator Symposium on Fundamental and Applied Science 2012*. 2012.
- [Log+99] R. L. Loger et al. “ ^{134}MC sample multi-cathode source of negative ions by cesium sputtering (^{134}MC -SNICS)”. In: *AIP Conference Proceedings* 475.1 (1999), pp. 640–643. DOI: 10.1063/1.59205.

- [LS64] J. Larson and R. Spear. “Gamma radiation from the alpha particle bombardment of ^{12}C ”. In: *Nuclear Physics* 56 (1964), pp. 497–511. DOI: 10.1016/0029-5582(64)90498-5.
- [Lud+19] F. Ludwig et al. “The muon intensity in the Felsenkeller shallow underground laboratory”. In: *Astroparticle Physics* 112 (2019), pp. 24–34. DOI: 10.1016/j.astropartphys.2019.04.006.
- [LUN+14] LUNA Collaboration et al. “A new study of the $^{22}\text{Ne}(p, \alpha)$ reaction deep underground: Feasibility, setup and first observation of the 186 keV resonance”. In: *Eur. Phys. J. A* 50.11 (2014), p. 179. DOI: 10.1140/epja/i2014-14179-5.
- [Mak+09] H. Makii et al. “ $E1$ and $E2$ cross sections of the $^{12}\text{C}(\alpha, \gamma_0)^{16}\text{O}$ reaction using pulsed α beams”. In: *Phys. Rev. C* 80 (6 Dec. 2009), p. 065802. DOI: 10.1103/PhysRevC.80.065802.
- [Mat+06] C. Matei et al. “Measurement of the Cascade Transition via the First Excited State of ^{16}O in the $^{12}\text{C}(\alpha, \gamma)^{16}\text{O}$ Reaction, and Its S Factor in Stellar Helium Burning”. In: *Phys. Rev. Lett.* 97 (24 Dec. 2006), p. 242503. DOI: 10.1103/PhysRevLett.97.242503.
- [Mei20] T. Meier. “Transmission und Ladungszahlverteilung des Kohlenstoffstrahls am Felsenkeller-Beschleuniger”. Bachelor’s Thesis. Dresden: Technische Universität Dresden, 2020.
- [Men+16] R. R. S. de Mendonça et al. “Deriving the solar activity cycle modulation on cosmic ray intensity observed by Nagoya muon detector from October 1970 until December 2012”. In: *Proceedings of the International Astronomical Union* 12.S328 (2016), pp. 130–133. DOI: 10.1017/S1743921317003763.
- [Mid77] R. Middleton. “A survey of negative ions from a cesium sputter source”. In: *Nuclear Instruments and Methods* 144.3 (1977), pp. 373–399. DOI: 10.1016/0029-554X(77)90001-5.
- [Mil+16] B. J. Miles et al. “On measuring the metallicity of a type Ia Supernova’s progenitor”. In: *The Astrophysical Journal* 1 (June 2016), p. 59. DOI: 10.3847/0004-637x/824/1/59.
- [MKO68] J. Morris, G. Kerr, and T. Ophel. “Energy levels of ^{16}O in the vicinity of 13 MeV”. In: *Nuclear Physics A* 112.1 (1968), pp. 97–116. DOI: 10.1016/0375-9474(68)90222-4.
- [MO64] I. Mitchell and T. Ophel. “Energy levels of ^{16}O in the vicinity of 13 MeV”. In: *Nuclear Physics* 58 (1964), pp. 529–543. DOI: 10.1016/0029-5582(64)90565-6.

- [MO65] I. Mitchell and T. Ophel. “Energy levels of ^{16}O in the vicinity of 13 MeV (II)”. In: *Nuclear Physics* 66.3 (1965), pp. 553–561. DOI: 10.1016/0029-5582(65)90784-4.
- [Mül20] M. Müller. “Monte-Carlo-Simulation des in-beam- γ -Spektroskopie-Aufbaus im Felsenkeller”. Bachelor’s Thesis. Dresden: Technische Universität Dresden, 2020.
- [Nik+94] T. Niklaus et al. “Optimising tandem accelerator stripping efficiency by simulation of charge changing processes”. In: *Nuclear Instruments and Methods in Physics Research Section B: Beam Interactions with Materials and Atoms* 92.1 (1994), pp. 115–121. DOI: 10.1016/0168-583X(94)95989-7.
- [Olá+16] L. Oláh et al. “Cosmic Background Measurements at a Proposed Underground Laboratory by the REGARD Muontomograph”. In: *Journal of Physics: Conference Series* 665.1 (2016), p. 012032.
- [Olá16] L. Oláh. “Research and Development of Particle Detectors for Muon Tomography and the CERN ALICE Experiment”. PhD thesis. Eötvös Loránd University, 2016.
- [Oue+92] J. M. L. Ouellet et al. “ $^{12}\text{C}(\alpha,\gamma)^{16}\text{O}$ cross sections at stellar energies”. In: *Phys. Rev. Lett.* 69 (13 Sept. 1992), pp. 1896–1899. DOI: 10.1103/PhysRevLett.69.1896.
- [Oue+96] J. M. L. Ouellet et al. “ $^{12}\text{C}(\alpha,\gamma)^{16}\text{O}$ cross sections at stellar energies”. In: *Phys. Rev. C* 54 (4 Oct. 1996), pp. 1982–1998. DOI: 10.1103/PhysRevC.54.1982.
- [OVH20] OVH SAS. *Topographische Karte Monaco, Höhe, Relief*. [Online; accessed 25-November-2020]. 2020. URL: <https://de-at.topographic-map.com/maps/ii3s/Monaco/>.
- [Pat+71] J. Patterson et al. “Experimental investigation of $^{16}\text{O} + ^{12}\text{C}$ nuclear burning at stellar energies”. In: *Nuclear Physics A* 3 (1971), pp. 545–559. DOI: 10.1016/0375-9474(71)90469-6.
- [PCL04] P. Povinec, J.-F. Comanducci, and I. Levy-Palomo. “IAEA-MEL’s underground counting laboratory in Monaco—background characteristics of HPGe detectors with anti-cosmic shielding”. In: *Applied Radiation and Isotopes* 61.2 (2004). Low Level Radionuclide Measurement Techniques - ICRM, pp. 85–93. DOI: 10.1016/j.apradiso.2004.03.019.
- [Pla+12] R. Plag et al. “ $^{12}\text{C}(\alpha,\gamma)^{16}\text{O}$ studied with the Karlsruhe 4π BaF₂ detector”. In: *Phys. Rev. C* 86 (1 July 2012), p. 015805. DOI: 10.1103/PhysRevC.86.015805.
- [Pra20] P. Prati. “The LUNA-MV facility at Gran Sasso”. In: *Journal of Physics: Conference Series* 1342 (Jan. 2020), p. 012088. DOI: 10.1088/1742-6596/1342/1/012088.

- [RC19] E. Ross and W. J. Chaplin. “The Behaviour of Galactic Cosmic-Ray Intensity During Solar Activity Cycle 24”. In: *Solar Physics* 294.1 (Jan. 2019), p. 8. DOI: 10.1007/s11207-019-1397-7.
- [Red+87] A. Redder et al. “The $^{12}\text{C}(\alpha,\gamma)^{16}\text{O}$ cross section at stellar energies”. In: *Nuclear Physics A* 462.2 (1987), pp. 385–412. DOI: 10.1016/0375-9474(87)90555-0.
- [Rob+16] Robertson, Daniel et al. “Underground nuclear astrophysics studies with CASPAR”. In: *EPJ Web of Conferences* 109 (2016), p. 09002. DOI: 10.1051/epjconf/201610909002.
- [Rol+88] C. Rolfs et al. *Cauldrons in the Cosmos: Nuclear Astrophysics*. Theoretical Astrophysics. University of Chicago Press, 1988.
- [Rot+99] G. Roters et al. “The E1 and E2 capture amplitudes in $^{12}\text{C}(\alpha,\gamma)^{16}\text{O}$ ”. In: *The European Physical Journal A - Hadrons and Nuclei* 6.4 (Dec. 1999), pp. 451–461. DOI: 10.1007/s100500050369.
- [Sag+17] K. Sagara et al. “Direct Measurement of $^{12}\text{C} + ^4\text{He}$ Fusion Cross Section Down to $E_{\text{cm}} = 1$ MeV and Prospects”. In: *Proceedings of the 14th International Symposium on Nuclei in the Cosmos (NIC2016)*. 2017. DOI: 10.7566/JPSCP.14.010404.
- [Sag86] S. Sagisaka. “Atmospheric effects on cosmic-ray muon intensities at deep underground depths”. In: *Il Nuovo Cimento C* 9.4 (July 1986), pp. 809–828. DOI: 10.1007/BF02558081.
- [Sar+12] M. Sarkar et al. “Transmission and charge state distribution of carbon ions emerging from nitrogen gas target in a tandem accelerator: Impact of stripper gas pressure”. In: *Physical Review Special Topics - Accelerators and Beams* 15 (Oct. 2012), p. 100101. DOI: 10.1103/PhysRevSTAB.15.100101.
- [Sch+11] D. Schürmann et al. “Study of the 6.05 MeV cascade transition in $^{12}\text{C}(\alpha,\gamma)^{16}\text{O}$ ”. In: *Physics Letters B* 703.5 (2011), pp. 557–561. DOI: 10.1016/j.physletb.2011.08.061.
- [Sch10] C. Schmitt. “Equilibrium Charge State Distributions of Low-Z Ions Incident on Thin Self-Supporting Foils”. PhD thesis. Notre Dame, Indiana: University of Notre Dame, 2010.
- [Sla64] J. C. Slater. “Atomic Radii in Crystals”. In: *The Journal of Chemical Physics* 41.10 (1964), pp. 3199–3204. DOI: 10.1063/1.1725697.
- [Ste19] J. Steckling. “Determination of the ideal operating parameters for ^{12}C -ion beam at Felsenkeller underground laboratory”. Bachelor’s Thesis. Dresden: Technische Universität Dresden, 2019.

- [Sug+79] I. Sugai et al. “Carbon deposition on targets during beam bombardment”. In: *Nuclear Instruments and Methods* 1 (1979), pp. 135–136. DOI: 10.1016/0029-554X(79)90492-0.
- [Sut+18] M. Suter et al. “Charge-state distributions and charge-changing cross sections and their impact on the performance of AMS facilities”. In: *Nuclear Instruments and Methods in Physics Research Section B: Beam Interactions with Materials and Atoms* 437 (2018), pp. 116–122. DOI: 10.1016/j.nimb.2018.08.014.
- [SW14] T. Sukhbold and S. E. Woosley. “The Compactness of Presupernova Stellar Cores”. In: *The Astrophysical Journal* 783.1 (Feb. 2014), p. 10. DOI: 10.1088/0004-637x/783/1/10.
- [Szü+19] T. Szücs et al. “Background in γ -ray detectors and carbon beam tests in the Felsenkeller shallow-underground accelerator laboratory”. In: *The European Physical Journal A* 55.10 (2019), p. 174. DOI: 10.1140/epja/i2019-12865-4.
- [Tan+06] A. Tang et al. “Muon simulations for Super-Kamiokande, KamLAND, and CHOOZ”. In: *Phys. Rev. D* 74 (5 Sept. 2006), p. 053007. DOI: 10.1103/PhysRevD.74.053007.
- [Tan+18] M. Tanabashi et al. “Review of Particle Physics”. In: *Phys. Rev. D* 98 (3 Aug. 2018), p. 030001. DOI: 10.1103/PhysRevD.98.030001.
- [TB04] O. Tarasov and D. Bazin. “LISE++ : design your own spectrometer”. In: *Nuclear Physics A* 746 (2004). Proceedings of the Sixth International Conference on Radioactive Nuclear Beams (RNB6), pp. 411–414. DOI: 10.1016/j.nuclphysa.2004.09.063.
- [Vaj+15] Z. Vajta et al. “ γ -ray spectroscopy of ^{19}C via the single-neutron knock-out reaction”. In: *Phys. Rev. C* (6 June 2015), p. 064315. DOI: 10.1103/PhysRevC.91.064315.
- [Var+13] D. Varga et al. “Close cathode chamber: Low material budget {MWPC}”. In: *Nuclear Instruments and Methods in Physics Research Section A: Accelerators, Spectrometers, Detectors and Associated Equipment* 698 (2013), pp. 11–18. DOI: 10.1016/j.nima.2012.09.025.
- [VHK11] D. Varga, G. Hamar, and G. Kiss. “Asymmetric Multi-Wire Proportional Chamber with reduced requirements to mechanical precision”. In: *Nuclear Instruments and Methods in Physics Research Section A: Accelerators, Spectrometers, Detectors and Associated Equipment* 648.1 (2011), pp. 163–167. DOI: 10.1016/j.nima.2011.05.049.
- [Wal11] H. W. P. H. Walter, ed. *Geologie von Sachsen I*. Stuttgart, Germany: Schweizerbart Science Publishers, Sept. 2011.

- [WH06] K. Werner and F. Herwig. “The Element Abundances in Bare Planetary Nebula Central Stars and the Shell Burning in AGB Stars”. In: *Publications of The Astronomical Society of The Pacific* 118 (Feb. 2006), pp. 183–204. DOI: 10.1086/500443.
- [You+08] G. C. Young et al. “Comparison of a 250 kV single-stage accelerator mass spectrometer with a 5 MV tandem accelerator mass spectrometer - fitness for purpose in bioanalysis”. In: *Rapid Communications in Mass Spectrometry* 22.24 (Dec. 2008), pp. 4035–4042. DOI: 10.1002/rcm.3829.
- [ZZB10] J. F. Ziegler, M. Ziegler, and J. Biersack. “SRIM – The stopping and range of ions in matter (2010)”. In: *Nuclear Instruments and Methods in Physics Research Section B: Beam Interactions with Materials and Atoms* 268.11 (2010). 19th International Conference on Ion Beam Analysis, pp. 1818–1823. DOI: 10.1016/j.nimb.2010.02.091.

Erklärung

Hiermit versichere ich, dass ich die vorliegende Arbeit ohne unzulässige Hilfe Dritter und ohne Benutzung anderer als der angegebenen Hilfsmittel angefertigt habe; die aus fremden Quellen direkt oder indirekt übernommenen Gedanken sind als solche kenntlich gemacht.

Diese Arbeit wurde an der TU Dresden und am Helmholtz-Zentrum Dresden Rossendorf unter wissenschaftlicher Betreuung von PD Dr. Daniel Bemmerer angefertigt. Die Arbeit wurde bisher weder im Inland noch im Ausland in gleicher oder ähnlicher Form einer anderen Prüfungsbehörde vorgelegt.

Ich erkenne hiermit die Promotionsordnung der Technischen Universität Dresden Fakultät Mathematik und Naturwissenschaften Bereich Physik vom 23.02.2011 an.

Felix Ludwig

Dresden, 25. Februar 2021



Bautzner Landstr. 400
01328 Dresden, Germany
Tel. +49 351 260-3581
Fax +49 351 260-13581
d.bemmerer@hzdr.de
<http://www.hzdr.de>